



Fermilab

FERMILAB-THESIS-1999-17

Hard single diffraction in $p\bar{p}$ collisions at 1800 and 630 GeV center of mass energies

by

Kristal Monika Mauritz

A dissertation submitted to the graduate faculty
in partial fulfillment of the requirements for the degree of
DOCTOR OF PHILOSOPHY

Major: High Energy Physics

Major Professor: John M. Hauptman

Iowa State University

Ames, Iowa

1999

Copyright © Kristal Monika Mauritz, 1999. All rights reserved.

Graduate College
Iowa State University

This is to certify that the Doctoral dissertation of
Kristal Monika Mauritz
has met the dissertation requirements of Iowa State University

Committee Member

Committee Member

Committee Member

Committee Member

Major Professor

For the Major Program

For the Graduate College

TABLE OF CONTENTS

1	INTRODUCTION	1
2	THEORY	4
	Soft diffraction	6
	Ingelman-Schlein model	7
	Soft Color Interaction model	10
	Speculation	11
3	THE DØ DETECTOR	13
	Detector coordinates	15
	Calorimeter	15
	Intercryostat detectors	18
	L0 detector	18
	Rapidity gap tagging	21
	Threshold	21
	Noise Studies	23
4	MONTE CARLO	30
	Method	30
	Gap Efficiency	34
	ξ distribution	39
	Event characteristics	45
	Diffractive rates	47
	Monte Carlo Interpretation	58
5	DATA ANALYSIS	59
	Data selection	59
	Signal measurement	61

Fitting	61
Cross-checks and corrections	68
ξ distribution	77
Event characteristics	77
6 INTERPRETATION	82
Rate comparison	82
ξ	83
7 CONCLUSION	88
Bibliography	89

LIST OF TABLES

Table 2.1	Quarks	4
Table 3.1	Units of ieta to pseudorapidity	20
Table 4.1	Gap Efficiency for hard gluons with forward and central jets at both center-of-mass energies.	37
Table 4.2	Far gap efficiency for various structure functions with forward and central jets at both center-of-mass energies.	39
Table 4.3	The predicted rates of 1800 POMPYT divided by PYTHIA at generator level for a hard gluon structure function and different choices of input values. The errors shown are binomial.	55
Table 4.4	The predicted rates of POMPYT divided by PYTHIA at generator level for several structure functions at 1800 and 630 GeV. The errors on the fraction are statistical. All have a central jet rate higher than forward jets except for the soft gluon.	55
Table 4.5	The predicted rates of POMPYT divided by PYTHIA after full detector simulation for several different structure function choices.	57
Table 5.1	Effect of cuts on number of events.	60
Table 5.2	Measured gap fractions for the far gap region for central and forward jets at both center-of-mass energies.	65
Table 5.3	Measured gap fractions for the near gap region for central and forward jets at both center-of-mass energies.	65
Table 5.4	Measured gap fractions for the long gap region for central and forward jets at both center-of-mass energies.	65
Table 5.5	Fitted gap fractions for the far gap region for 1800 forward jets, varying the data cuts applied to the sample. The fraction is stable.	68

Table 5.6	Fitted gap fractions for the far gap region for 1800 central jets, varying the data cuts applied to the sample. The fraction is stable.	69
Table 5.7	Fitted gap fractions for the far gap region for 630 forward jets, varying the data cuts applied to the sample. The fraction is stable.	69
Table 5.8	Fitted gap fractions for the far gap region for 630 central jets, varying the data cuts applied to the sample. The fraction is stable.	69
Table 5.9	The efficiency of the vertex algorithm to find one vertex in a single interaction event for all events and for gap events.	72
Table 5.10	The fitted gap fractions for 1800 forward and central jets with different minimum thresholds for finding the calorimeter multiplicity.	73
Table 5.11	The fitted gap fractions for 630 forward and central jets with different minimum thresholds for finding the calorimeter multiplicity.	75
Table 5.12	The measured far gap fractions after the vertex correction.	75
Table 5.13	The measured ratios of the far gap fractions.	75
Table 6.1	The rate predictions for Monte Carlo after folding in the gap efficiency.	83
Table 6.2	The measured ratios of the far gap fractions for POMPYT structure functions.	83

LIST OF FIGURES

Figure 1.1	The soft processes of elastic scattering and single diffraction. Elastic scattering has only the proton and antiproton in the final state with no particles between them (a rapidity gap), and single diffraction is characterized by particle production opposite a rapidity gap with either the proton or the antiproton in the final state.	3
Figure 1.2	The hard processes of hard single diffraction and hard double pomeron exchange. The hard processes have jet production in the final state.	3
Figure 2.1	The strong fine structure constant, α_s , as a function of the momentum transfer Q . At high momenta transfer the coupling between particles approaches zero allowing QCD to be calculable with perturbation theory, and at low momenta the strong fine structure constant becomes large and is non-perturbative [4]. . .	5
Figure 2.2	Inelastic cross-section as a function of four-momentum t [5]	7
Figure 2.3	Total cross-section versus center-of-mass energy [6]	8
Figure 2.4	Single Diffraction	9
Figure 2.5	Factorization in Ingelman and Schlein model	10
Figure 2.6	Soft Color Interaction model creates rapidity gaps through non-perturbative color cancellation. It has no explicit pomeron dynamics [14].	11
Figure 3.1	The D0 Detector has three main systems; from the inside out there is the central detector which includes tracking and vertexing, the calorimeter, and the muon system.	14
Figure 3.2	The $D\bar{0}$ Calorimeter is divided into three parts: the central calorimeter (CC) and the two identical end cap calorimeters (EC). It has full coverage for $ \eta < 4.1$	16

Figure 3.3	A sample calorimeter cell showing uranium as the absorbing medium and liquid argon as the ionizing medium. As a particle traverses the absorber, the particle showers and ionizes the argon which produces a charge.	17
Figure 3.4	The segmentation of the calorimeter cell in detector eta and ieta. The segmentation is $\delta\eta \times \delta\phi = 0.1 \times 0.1$ in EM and HAD out to $ieta = 32$ or $\eta_d = 3.2$. Due to the physical size, larger values of $ieta$ are ganged together and correspond to even larger η_d	18
Figure 3.5	A side view of the calorimeter, showing the segmentation and slices in pseudo-rapidity space.	19
Figure 3.6	The L0 detector consists of scintillator tiles (shaded region) surrounding the beampipe.	20
Figure 3.7	Fraction of events with one or more tower greater than threshold due to noise versus threshold. The threshold to be above most of the noise for EM is 150 MeV, for FHD is 500 MeV, and for IH15 is 50 MeV.	24
Figure 3.8	Fraction of events with one or more tower greater than threshold versus threshold if there is an interaction. This can provide a measure of efficiency for tagging particles in the EM and FHD case.	25
Figure 3.9	The multiplicity of L0 and calorimeter towers above threshold over a data-set containing only noise. In all three rapidity gap definitions, very few rapidity gaps are ruined due to noise.	26
Figure 3.10	Multiplicity Distribution for inclusive and forward trigger samples with a 200 MeV tower threshold	27
Figure 3.11	Multiplicity Distribution for inclusive and forward trigger samples with a 60 MeV tower threshold	28
Figure 3.12	Noise from Zero bias overlaid with the 60MeV threshold multiplicity distribution for forward sample.	29
Figure 4.1	The η distribution at $\sqrt{s} = 1800$ GeV for soft gluons (solid line), hard gluons (dashed line), and quarks (dotted line) structures.	31
Figure 4.2	The η distribution at $\sqrt{s} = 630$ GeV for soft gluons (solid line), hard gluons (dashed line), and quarks (dotted line) structures.	32

Figure 4.3	The multiplicity of particles with an energy greater than 700 MeV for the far gap with both POMPYT and PYTHIA. The POMPYT multiplicity distribution is peaked at zero, while the PYTHIA multiplicity is peaked farther out and tapers off to zero at zero multiplicity.	33
Figure 4.4	The two dimensional (L0 vs. N_{CAL}) multiplicity distributions for POMPYT (upper) with the hard gluon structure function and for PYTHIA (lower) after full detector simulation.	34
Figure 4.5	The multiplicity for 1800 GeV hard gluons in the long gap and far gap for forward and central jets. The gap efficiency is higher (less spread out of the 0 – 0 bin) when the gap is farther away from the interaction region.	36
Figure 4.6	The multiplicity for 630 GeV hard gluons in the long gap and far gap for forward and central jets. As at 1800, the gap efficiency increases when the gap is farther away from the interaction region.	37
Figure 4.7	The MC central jet multiplicity at 1800 GeV in bins of ξ . The gap efficiency decreases as the ξ increases.	38
Figure 4.8	The ξ distribution for the hard gluon at 1800 GeV for all events (solid line) with 12 GeV jets. The dashed line is the ξ distribution if we require central jets and the dotted line for forward jets. The ξ region probed for the central jets is higher than for the forward jets.	40
Figure 4.9	The effect of requiring a gap in the ξ distribution for forward and central jets with the hard gluon structure function at 1800 GeV. The long gap (dashed) restricts more of the higher mass events than the far gap (dotted).	41
Figure 4.10	The ξ distribution for the hard gluon structure at 630 GeV for all events. The dashed line is the ξ distribution if we require central jets and the dotted line for forward jets. The ξ region probed for the central jets is higher than for the forward jets, and overall higher than at 1800.	42
Figure 4.11	The effect of requiring a gap in the ξ distribution for forward and central jets with the hard gluon structure function at 630 GeV. The long gap (dashed) restricts more of the higher mass events than the far gap (dotted).	43

Figure 4.12	The relation between the true ξ and the ξ calculated using Collin's formula at particle level for the hard gluon at 1800 and 630 GeV and for the quark and soft gluon structure function. The slope of one does not depend on center-of-mass or structure function.	44
Figure 4.13	At the calorimeter level, the relation between true ξ and the ξ calculated. Shown is the hard gluon and quark structure function at both center of mass energies. The slope is the same within errors in all cases, but it is higher than one because we are only collecting about half of the energy using only the EM calorimeter.	45
Figure 4.14	The number of jets, jet width, delta phi between jets, and jet E_T for the two leading jets in POMPYT hard gluon (solid) and PYTHIA (dashed) at 1800 GeV. The POMPYT events are quieter and thinner, consistent with less radiation in the event.	46
Figure 4.15	The number of jets, jet width, delta phi between jets, and jet E_T for the two leading jets in POMPYT hard gluon (solid) and PYTHIA (dashed) at 630 GeV.	47
Figure 4.16	The jet E_T distribution at 630 GeV for two leading jets restricting the ξ in POMPYT to less than 0.1. POMPYT (solid curve) falls below PYTHIA (dashed curve) throughout much of the distribution.	48
Figure 4.17	The number of jets, jet width, delta phi between jets, and jet E_T for the two leading jets in POMPYT flat gluon (solid) and PYTHIA (dashed) at 1800 GeV.	49
Figure 4.18	The number of jets, jet width, delta phi between jets, and jet E_T for the two leading jets in POMPYT flat gluon (solid) and PYTHIA (dashed) at 630 GeV.	50
Figure 4.19	The number of jets, jet width, delta phi between jets, and jet E_T for the two leading jets in the POMPYT quark structure function (solid) and PYTHIA (dashed) at 1800 GeV.	51
Figure 4.20	The number of jets, jet width, delta phi between jets, and jet E_T for the two leading jets in the POMPYT quark structure function (solid) and PYTHIA (dashed) at 630 GeV.	52
Figure 4.21	Event characteristics for the soft gluon structure function (solid) at 1800 GeV compared to PYTHIA (dotted).	53
Figure 4.22	Event characteristics for the soft gluon structure function (solid) at 630 GeV compared to PYTHIA (dotted).	54

Figure 4.23	The jet η and η_{boost} distribution for POMPYT hard gluon $\xi < 0.10$ and $\xi < 0.05$. The higher momentum pomeron is only slightly boosted where the lower momentum pomeron distribution shows a definite boost. Overlaid on the η_{boost} distributions is a PYTHIA sample that is symmetric about zero. The last plots show the fraction versus η_{boost} for each distribution. The low ξ fraction increases with η_{boost} due the kinematics of the event.	56
Figure 4.24	The distribution of jet η in POMPYT and PYTHIA if $\eta_{boost} < 1.0$, and the effect on each with cutting on two central jets. PYTHIA loses a significant portion of events with the cut compared to POMPYT.	57
Figure 5.1	The multiplicity distributions for 1800 GeV forward jets, the entire multiplicity, the lower multiplicity bins, and the projections onto the L0 and calorimeter axes.	62
Figure 5.2	The fit results for 1800 GeV forward jets.	64
Figure 5.3	The 2D far gap multiplicity at 1800 GeV for forward and central jets. Shown is for all multiplicities (left) as well as a close-up of the lower multiplicity bins (right).	66
Figure 5.4	The 2D far gap multiplicity at 630 GeV for forward and central jets. Shown is for all multiplicities (left) as well as a close-up of the lower multiplicity bins (right).	67
Figure 5.5	Luminosity distributions for 1800 and 630 GeV.	70
Figure 5.6	The fraction of events with one vertex versus luminosity in 630 GeV forward jets.	72
Figure 5.7	The far gap multiplicity distributions for 1800 GeV forward jets with and without noise. The $0 - 0$ multiplicity bin is slightly higher without noise, but the signal extracted from the fit is consistent.	73
Figure 5.8	As the calorimeter threshold increases, the distributions shifts to lower multiplicity.	74
Figure 5.9	Fits to N_{CAL} using a negative binomial and a line.	76
Figure 5.10	The 1800 GeV ξ distributions for forward, central and all jets. The factor of 2.2 is included to account for only using the EM.	78
Figure 5.11	The 630 GeV ξ distributions for forward, central, and all jets.	79
Figure 5.12	Comparing gap events (solid) to non-diffractive events (dashed) at 1800.	80
Figure 5.13	Comparing gap events (solid) to non-diffractive events (dashed) at 630.	81
Figure 6.1	The ξ distribution for 1800 GeV data (solid) and for POMPYT hard gluons (dotted).	84

Figure 6.2	The ξ distribution for POMPYT hard gluon forward jets at 1800 with a far rapidity gap. Shown are also the analogous distribution for PYTHIA imposing a far gap, and the combined distribution with the same purity as in the (0, 0) data.	85
Figure 6.3	The diffractive ξ distribution (solid) for forward, central, and all jets at 1800 GeV. Also calculated is the unnormalized ξ distribution for non-diffractive data (dotted), assuming color cancellation to produce a far gap.	86
Figure 6.4	The diffractive ξ distribution (solid) for forward, central, and all jets at 630 GeV. Also calculated is the unnormalized ξ distribution for non-diffractive data (dotted), assuming color cancellation to produce a far gap.	87

ACKNOWLEDGEMENTS

I would like to thank the support of the DØ Collaboration at Fermilab, specifically the QCD group, convenors, the physics coordinators, and everyone that assisted both with the detector and the software to make my analysis possible. I also want to heartfully thank Andrew Brandt and Bob Hirosky specifically for their guidance, help, and patience through this difficult topic. They were there whenever I asked for a suggestion or a comment and helped to make my experience enjoyable. I also want to profusely thank my advisor, John Hauptman, for his support and allowing me to find a topic that I would enjoy.

Lastly, I want to thank my boyfriend, Pete, as well as Laura Lee and my other friends for being with me over these last years and supporting me with their love and friendship.

1 INTRODUCTION

The search for a basic understanding of the universe has been going on for most of recorded history. The first documented speculations about the nature of the cosmos are from the ancient Greek philosophers around 4 B.C.. Democritus and Leucippus are perhaps the most well known because of their postulate that the universe is composed of hard, indivisible bodies, called atomos, that move through empty space. Democritus proposed that atoms with various shapes and masses are responsible for all the macroscopic differences that we see around us, and that the cosmos was formed by a vortex of atoms.

Today, our understanding of the world in which we live is quite different than in Democritus' day. With experiment and the scientific method we can test our hypotheses and quantify them. Today we believe that the fabric of the cosmos is the vacuum with quarks and gluons, leptons, photons, and bosons. Particle physics is the study of these most basic beginnings on which everything else is built.

We have a good understanding today of much of the building blocks in the "standard model". Of the four forces: electricity and magnetism, weak, strong, and gravity, we can trace nearly back to the big bang how electricity and magnetism and the weak force diverged. The electroweak theory describes these interactions very well. There is also a good understanding of the strong force at high energies with QCD or Quantum Chromodynamics, and work is continuing on combining all four forces into what we believe should be one force at the time of the big bang.

At the Tevatron, currently the world's highest energy particle accelerator, we can study the interactions at this tiny scale to study the strong and weak forces. Protons and antiprotons are hadrons composed of quarks, antiquarks, and gluons, so by colliding them at high energies, we literally have quark and gluon collisions. From these collisions we study many subjects, including the top quark, b-quark states, the W mass, quark compositeness, and the inclusive jet cross-section, and compare to theory.

QCD provides a systematic description of the strong force and has a predictive power at high energies, but at lower energies the same equations become uncalculable. About 40% of the cross-section

is produced diffractively (which involves low energy interactions where the p or \bar{p} can stay intact), and it is poorly understood.

We separate diffraction into two classes: soft diffraction and hard diffraction. In soft diffraction, which has been studied for many years, there are the subclasses of elastic scattering

$$p + \bar{p} \rightarrow p + \bar{p}$$

and single diffraction

$$p + \bar{p} \rightarrow p + X \text{ or } p + \bar{p} \rightarrow \bar{p} + X,$$

as shown in Figure 1.1. The elastic scattering final state has both the proton and antiproton which continue down the beamline and no particles between them (called a rapidity gap), and in single diffraction, either the proton or antiproton becomes excited and breaks apart, scattering particles throughout half of the detector opposite a rapidity gap. Observation of nearly constant total and elastic cross-sections led to the introduction of the 'pomeron' by Pommeranchuk. These soft collisions can be modeled rather well with Regge theory [1], which predates QCD.

Hard diffraction is similar to soft diffraction, except that jets are produced in the final state (see Figure 1.2) and was introduced by Ingelman and Schlein [2] in 1985 as a field of study to probe the nature of the pomeron. In the classic experimental high energy physics tradition, something that is known (the proton) is collided against something that is not known (the pomeron) at high energy to study the nature of the unknown (the pomeron). Hard Single Diffraction (HSD) is a subset of single diffraction where the signature is the production of two energetic jets

$$p + \bar{p} \rightarrow j + j + X.$$

Hard double pomeron exchange is characterized by two central jets and the outgoing proton and antiproton in the final state with a rapidity gap on both sides of the jets,

$$p + \bar{p} \rightarrow p + \bar{p} + j + j + X.$$

With these energetic collisions we can study in depth the nature of the diffractive interactions as well as probe the method for producing it. Since the introduction of hard diffraction, the field of study has increased dramatically. Today, in addition to diffractive jets, there is diffractive W -boson, diffractive Z , diffractive J/ψ , and diffractive heavy quarks. The combination of these results gives new insight into the nature of the exchanged object. In this dissertation, I focus on the study of hard single diffractive jet production from $p\bar{p}$ collisions at two center of mass energies: 1800 and 630 GeV.

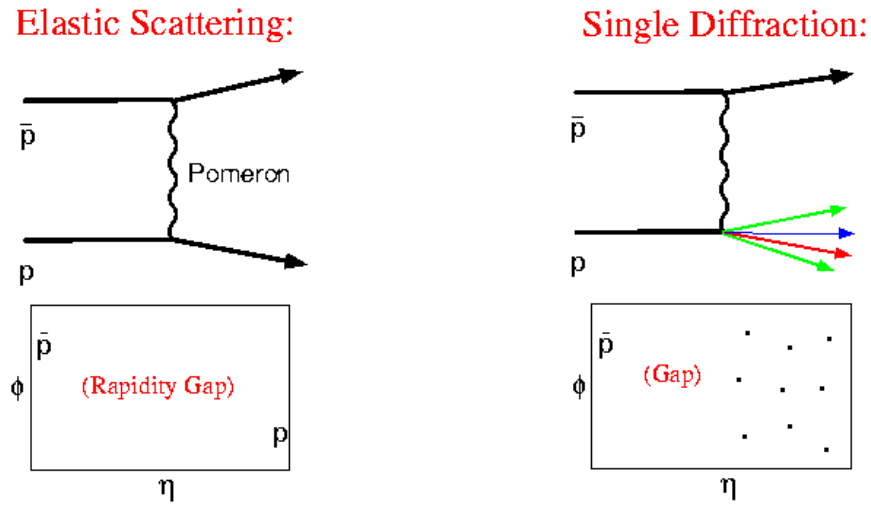


Figure 1.1 The soft processes of elastic scattering and single diffraction. Elastic scattering has only the proton and antiproton in the final state with no particles between them (a rapidity gap), and single diffraction is characterized by particle production opposite a rapidity gap with either the proton or the antiproton in the final state.

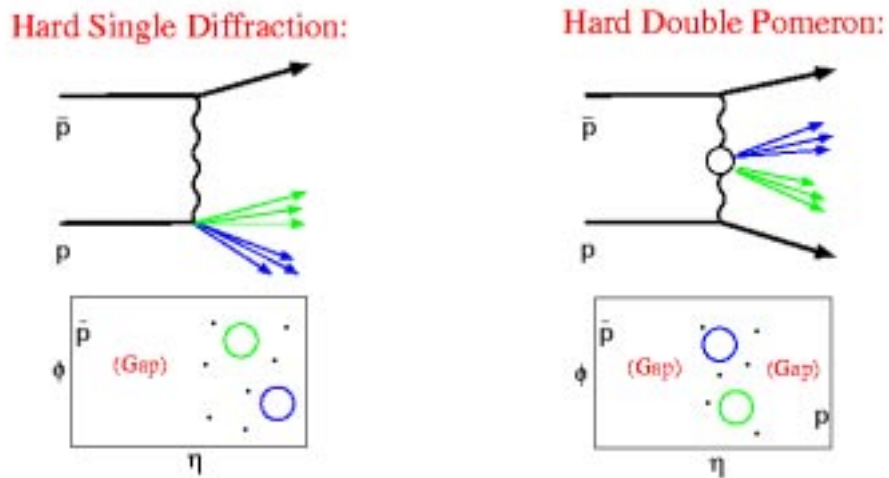


Figure 1.2 The hard processes of hard single diffraction and hard double pomeron exchange. The hard processes have jet production in the final state.

2 THEORY

Quantum Chromodynamics (QCD) has been a remarkably successful theory where it is calculable. With the quark-model, it describes the large number of once thought to be strongly interacting elementary particles, mesons (like π^+) and baryons (like protons and neutrons) in terms of a simpler picture of quarks and gluons –carriers of “color” charge. In a very simple picture, there are three “color” charges: red, green, and blue. Mesons have a quark and an antiquark and baryons have three quarks with gluons “pasting” the quarks together. All observable objects are colorless, so mesons ($q\bar{q}$) have color-anticolor (i.e. $r\bar{r}$) and baryons have all three colors (i.e. rgb or \overline{rgb}). There are six basic quarks, shown in table 2.1, along with the antiquarks in the six flavors: red, green, blue, $\overline{\text{red}}$, $\overline{\text{green}}$, and $\overline{\text{blue}}$ and eight gluons to mediate the interactions. Of course life is never that easy because these mesons and baryons exist above the vacuum, which instead of being empty, has quarks and gluons flitting in and out of existence obeying Heisenberg’s uncertainty principle $\Delta E\Delta t \geq \hbar/2$. In other words, $q\bar{q}$ pairs of energy E can come into existence for a time of order $\hbar/2E$. These are the “sea” quarks that are attracted to the “valence” quarks in the hadrons (mesons and baryons). For a systematic examination of particle physics, see Reference [3].

QCD is an $SU(3)$ gauge field theory describing all of these interactions at high energies. What makes QCD calculable is the property of asymptotic freedom. That is, at high momentum transfer, the strength of the coupling between the particles decreases and approaches zero as the momenta goes to infinity (see Figure 2.1). This means that at high momenta, perturbation theory can be used to calculate the appropriate matrix element that describes the interaction. However, at low momentum transfer the strength of the coupling or the strength of the strong force increases between the particles.

Table 2.1 Quarks

u	s	t
d	c	b

The colored particles are tightly bound together. If we try to remove a quark from a $q\bar{q}$ pair, for instance, the energy grows with the distance that the quark is pulled until it becomes great enough that it is easier to create another $q\bar{q}$ pair to break the “string” that connected the original quark to its partner. This property is called confinement. In this low momentum transfer region QCD cannot calculate the interaction, so it is called the non-perturbative region or soft QCD.

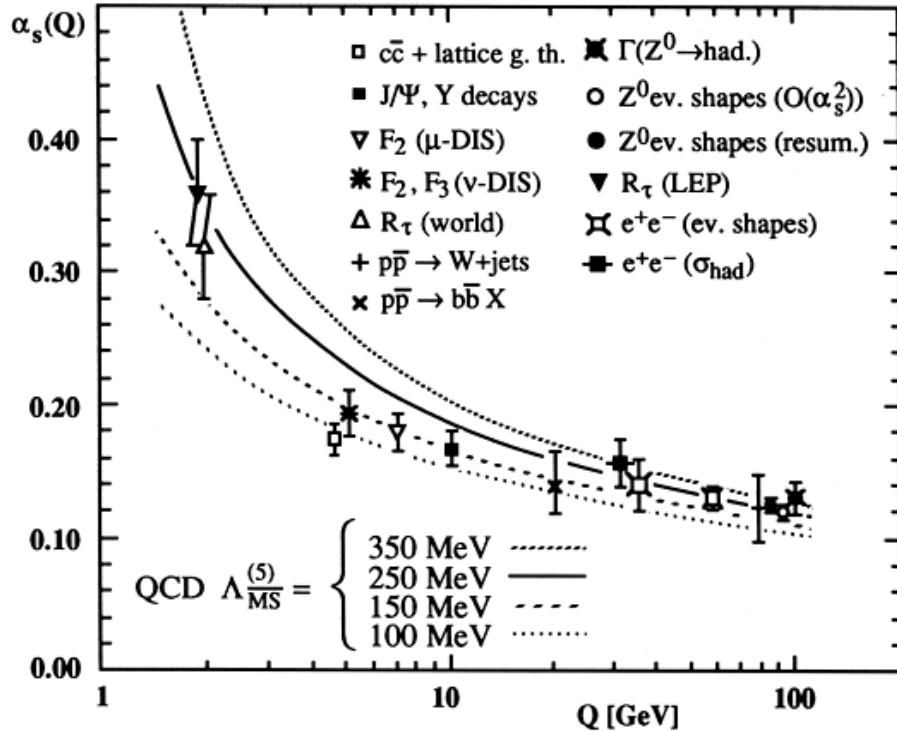


Figure 2.1 The strong fine structure constant, α_s as a function of the momentum transfer Q . At high momenta transfer the coupling between particles approaches zero allowing QCD to be calculable with perturbation theory, and at low momenta the strong fine structure constant becomes large and is non-perturbative [4].

Although what happens in the non-perturbative region of QCD is not directly calculable, it is still an important regime. At a high energy interaction point where a quark or gluon from a proton interacts with a quark or gluon from an antiproton the participants can be treated as free, but as they recede there is a transition to the soft regime. The standard way to treat hadronization is with color “strings”, so that as the strings are stretched, $q\bar{q}$ pairs or mesons are formed. The final state of a high energy $2 \rightarrow 2$ interaction is two jets (or two clumps of particles where the quark or gluon hadronized) as well as “beamjets” from the breakup and hadronization of the proton and antiproton. So every interaction,

even those at high energies, includes soft physics that is not directly calculable from direct QCD. It is worth exploring the soft physics, whether to understand underlying event backgrounds that are in every physics process or to model Monte Carlos correctly, which is a primary tool in experimental high energy physics.

Soft diffraction

In hadron-hadron collisions at the Tevatron, about 40% of the cross-section is soft diffractive physics –so called because as shown in Figure 2.2, the cross-section versus four-momentum transfer t , has the behavior typical of optical scattering through a circular hole. (J_0 Bessel function that goes as e^{-bt} where $b \approx 12$ for elastic scattering and $b \approx 7$ for single diffraction. Figure 2.3 shows the total cross-section versus center-of-mass energy. The phenomenology of Regge theory, which pre-dates QCD, successfully describes many features of the data. Simply, the total cross-section is fit to an expression $\sigma^{total} = Xs^{0.08} + Ys^{-0.45}$ where the second term is reggeon exchange (hadrons) which decreases with energy and the first term is pomeron exchange which increases with energy. At high energies, the cross-section becomes dominated by pomeron exchange, so it is clearly the most important Regge pole particle. As the mediating particle for inelastic scattering, the pomeron must then have quantum numbers of the vacuum, with no baryon number or charge. An in-depth treatment of Regge theory is given in Reference [1]. To fit into a QCD picture of the strong force, the pomeron must be a composite particle (or pseudo-particle) of quarks and gluons.

In this picture of diffraction, note that the exchanged particle must be a color-singlet; it must be colorless. Figure 2.4 shows a diagram of a single diffractive event. The final state is characterized by particle production from the proton that broke up as well as the diffracted proton and a rapidity gap (no particles produced) on the side of the outgoing proton. If the exchanged object had color, then the outgoing proton is no longer colorless and there is a color-string between it and the exchanged object. The outgoing proton will hadronize and as the string breaks, particles will be produced throughout the whole region. So the exchanged object must be colorless for a diffractive event.

Note that there are two experimental signatures for diffractive events. We can tag the diffracted proton or antiproton, or we can tag the rapidity gap produced in these events. For this thesis, we use the latter method because we do not yet have the detectors (called Roman Pots) to tag the diffracted proton. In the next run at the Tevatron, these will be installed at DØ which will increase the ability of doing diffractive physics.

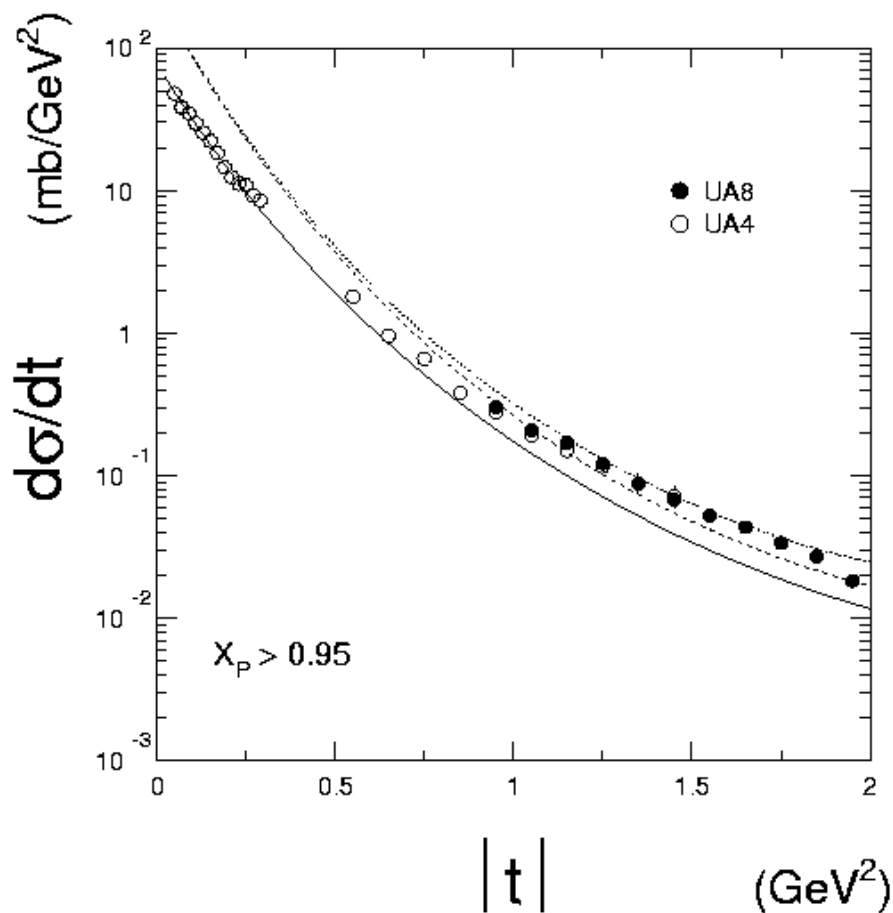


Figure 2.2 Inelastic cross-section as a function of four-momentum t [5]

Ingelman-Schlein model

Ingelman and Schlein introduced the theory of hard diffraction as a means to probe into the nature of the pomeron [2], the exchanged object in diffractive scattering. They blended both Regge phenomenology and QCD to write the cross-section for diffractive hard scattering as

$$\frac{d\sigma(\bar{p}p \rightarrow p + X)}{dx_P dt dx_1 dx_2} = f_{P/p}(x_P, t) \frac{d\sigma(\bar{p}P \rightarrow X)}{dx_1 dx_2}. \quad (2.1)$$

The first factor is called the “flux” factor and gives the probability of the ‘emission’ of a pomeron. This can be estimated using Regge theory and data as

$$f_{P/p}(x_P, t) = \frac{d\sigma/dx_P dt}{\sigma_{Pp \rightarrow X}}. \quad (2.2)$$

The second factor is the cross-section for the hard pomeron-particle scattering, which convolutes the parton density in the pomeron, the standard QCD matrix element, and the parton density of the proton.

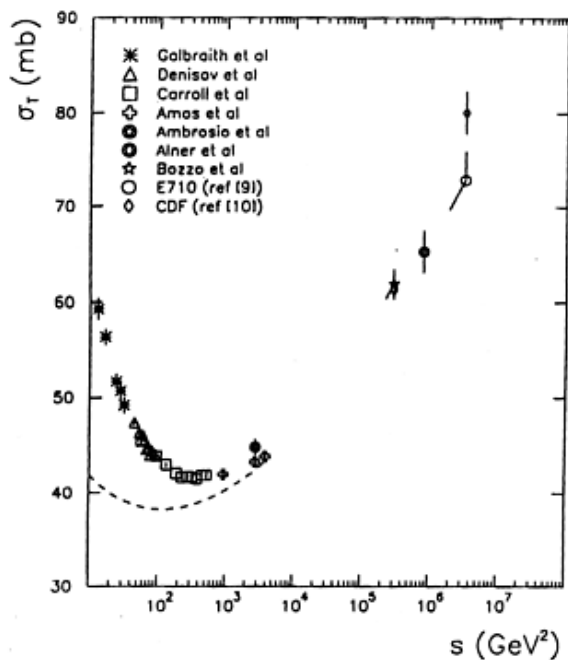


Figure 2.3 Total cross-section versus center-of-mass energy [6]

So in simpler terms, the interaction is factorized into two parts as shown in Figure 2.5. In a particular frame of reference we can say the the proton ‘emits’ the pomeron (which is described by the flux), and then there is a hard scattering between a parton in the proton and a parton in the pomeron, dictated by perturbative QCD.

With this picture, there are a number of kinematic variables that become important. The total $p\bar{p}$ center of mass energy is given by \sqrt{s} . The standard four-momentum transfer t is defined as

$$t = -(p_f - p_i)^2 \quad (2.3)$$

where p_i is the incoming proton and p_f is the outgoing proton after it has diffractively scattered. The momentum fraction of the proton that is taken by the pomeron is given by

$$\xi = 1 - x_p = 1 - p_f/p_i. \quad (2.4)$$

Diffraction dominates for $\xi < 0.05$ so that the maximum diffractive mass available is

$$M_x = \sqrt{\xi s} \approx 400 \text{ GeV}/c^2 \text{ for } \xi = 0.05. \quad (2.5)$$

Just like the interacting parton from the proton will have a momentum fraction x , the interacting parton from the pomeron will have a momentum fraction we will call β . This fraction will be described by the structure function of the pomeron.

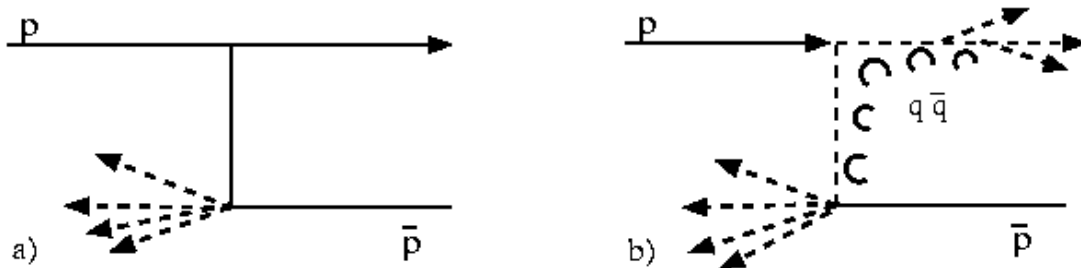


Figure 2.4 In this picture diffraction must be mediated through a color-singlet.
 a) A diagram of single diffraction where the \bar{p} breaks. b) If the exchanged object had color instead, the outgoing proton would also have color and there would be a color string between the outgoing proton and the exchanged object. Quark/antiquark pairs would be produced along the string and the proton would hadronize.

Ingelman and Schlein proposed three possible structure functions to compare to data. They ignored any dependence on the four-momentum t and assumed that the Q^2 evolution would be small, so that the variable that it would depend on is β . For a gluon structure, two extreme possibilities were considered: a hard gluon composed of two gluons sharing the momenta of the pomeron ($\langle \beta \rangle = 1/2$),

$$\beta G(\beta) = 6\beta(1 - \beta); \quad (2.6)$$

a soft effective gluon structure like the average gluon structure of the proton ($\langle \beta \rangle = 1/7$),

$$\beta G(\beta) = 6(1 - \beta)^5; \quad (2.7)$$

and a quark structure function.

$$\beta G(\beta) = \frac{6}{4}\beta(1 - \beta). \quad (2.8)$$

The momentum sum rule ($\int_0^1 x f(x) = 1$) is applied for the normalization, although it does not obviously apply to a virtual pomeron. A quark-dominated pomeron model developed by Donnachie and Landshoff is similar to the quark structure function above with a smaller normalization since they do not apply the momentum sum rule [8].

By studying different final states, the quark and gluon content of the structure function can be measured. For example, jet production couples more strongly to the gluon content of the pomeron,

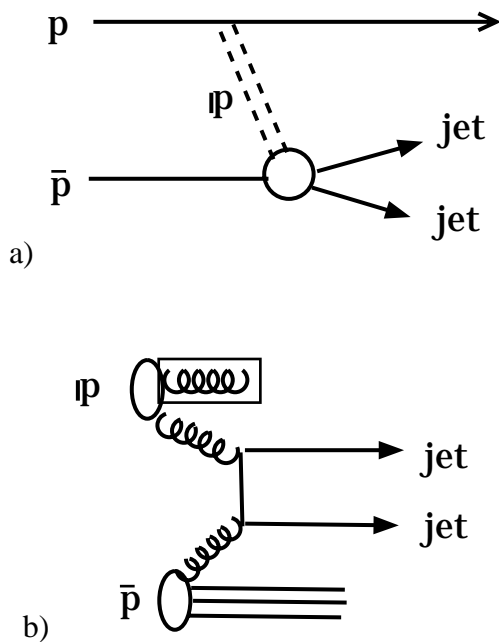


Figure 2.5 Factorization assumes that pomeron exchange can be treated as two separate interactions. a) The pomeron is “emitted” from the proton (antiproton). b) A parton from the pomeron undergoes a hard scatter with a parton in the antiproton (proton). In this case a heavy quark pair is produced diffractively.

and diffractive W production measures mostly the quark content of the pomeron because the gluon content ($\gamma g \rightarrow q\bar{q}$) is suppressed by an order α_s .

The Ingelman and Schlein model is by far the most widely used, and until recently, the only one capable of describing the data at both DESY (an ep collider) as well as the Tevatron. There are several Monte Carlos based on the Ingelman and Schlein model that refine the pomeron structure function and can include Q^2 evolution and ξ dependence. In the last couple of years the soft color interaction model has been developed which is quite different and needs further study.

Soft Color Interaction model

The soft color interaction model was developed [9, 10, 11, 12] to explain rapidity gaps and diffraction with no explicit pomeron dynamics. It is based on the hypothesis that adding soft color interactions

can change the hadronization of a typical event such that rapidity gaps can occur in the final state. These soft color interactions (SCI) are non-perturbative in nature and exist between partons to form closed loops, as pictured in Figure 2.6. SCI changes the color of the partons involved, so it changes the color topology of the event.

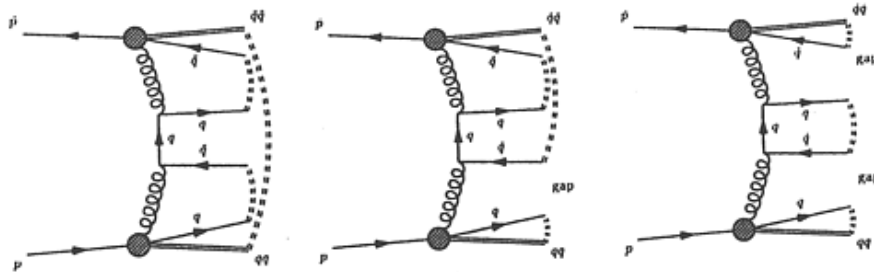


Figure 2.6 Soft Color Interaction model creates rapidity gaps through non-perturbative color cancellation. It has no explicit pomeron dynamics [14].

The SCI also gives an exponential t -dependence as in the Ingelman and Schlein model. The t -dependence of the model is related to the primordial k_{\perp} or transverse momentum of the partons in the proton. The p_T from the interacting parton is balanced by the recoil p_T of the proton. It also demonstrates many of the same event characteristics that is shown in the Ingelman-Schlein model. The events are quieter because it preferentially selects events which in addition to a grazing collision, do not have a spectator interaction (double parton-parton scattering). Without this extra interaction, the events have less ‘underlying event’ and are overall quieter.

Speculation

The Ingelman-Schlein and SCI model are the two basic types of models, although there are others and the field is continually evolving. In the Ingelman-Schlein model, the pomeron is treated as a pseudo-particle and the event is treated as completely factorizable. In fact, it has been shown [13] that this is a correct treatment at HERA but is incorrect at the Tevatron. In $p\bar{p}$ collisions with the extra colored object, it becomes easier for there to be a soft gluon emission between the proton and antiproton. However, it might still be a good approximation at the Tevatron. The scale where factorization breaks is not known. In SCI and other similar and emerging models there is no pomeron dynamics—only soft

non-perturbative interactions that allow for color cancellation so that the proton or antiproton stays whole and a rapidity gap is produced.

One other speculation is that the pomeron could be a 9th gluon. With a 9th gluon, that would make the standard model $SU(3)_c$ which in itself might not describe the data. However, if the 9th gluon were a color-singlet, it still could not be the pomeron. If the 9th gluon exists, it would be a pure color-singlet, meaning that it has *no* color charge and cannot couple to color at all. In QCD it would act like a photon, except that it wouldn't couple to anything. This would mean that if it did exist, we would have no way of detecting it. The reason why the pomeron, a color-singlet, can couple to quarks and gluons is because it is a composite. It is the quarks and gluons in the pomeron that do the interacting [17].

In the models described above, there are several different methods to produce diffraction, where the proton or antiproton stays whole and a rapidity gap is produced. For the purposes of this thesis, we will define the pomeron discussed in data as the “thing” or mechanism that produces diffractive events and rapidity gaps. Then we will compare it to the Ingelman-Schlein model which is currently available.

3 THE DØ DETECTOR

The study of QCD is synonymous with the study of jet physics. The accelerator acts like a huge microscope to probe the quarks and gluons. The Tevatron, currently the worlds highest energy accelerator, coupled with DØ a high p_t multipurpose detector, provides a perfect environment for these studies.

The 5500-ton, 40-foot-high DØ detector is a multipurpose detector designed to explore many types of high p_t phenomena at the Fermilab Tevatron. These include precision tests and measurements of the electroweak W and Z bosons, observation of the top quark, production of b-quark hadrons, tests of perturbative QCD, and searches for phenomena beyond the standard model. To study these subjects, DØ was designed to provide excellent identification of electrons and muons and good measurements of missing transverse energy and parton jets.

The DØ detector is composed of three main systems: the central detector, the calorimeter, and the muon spectrometer (see Figure 3.1). The central detector system is the innermost part of the detector and provides vertex finding and tracking. Wrapping closest to the beampipe is the vertex drift chamber, followed by the transition radiation detector, and the central drift chamber. Two forward drift chambers sit perpendicular to the beampipe at the ends. The liquid- argon/uranium calorimeter is the primary detector of many analyses as it is responsible for energy measurement and particle identification. It consists of three sections, the central calorimeter which surrounds the central drift chamber in the region $|\eta| < 1.0$, and two endcap calorimeters for detection of particles and jets in the forward region up to $|\eta| < 4.1$. The muon spectrometer identifies muons and measures their momentum, and it surrounds the large calorimeter in a box. In addition to these main systems there are detectors to bridge the gap between the central calorimeter and the endcap calorimeters. These include the massless gaps and intercryostat detectors in the rapidity region $0.8 \leq |\eta| \leq 1.4$, and the L0 detector which is a scintillating detector surrounding the beampipe. Full descriptions of each part of the DØ detector can be found in Ref [18]. The following sections will concentrate on the parts of the detector used in this analysis.

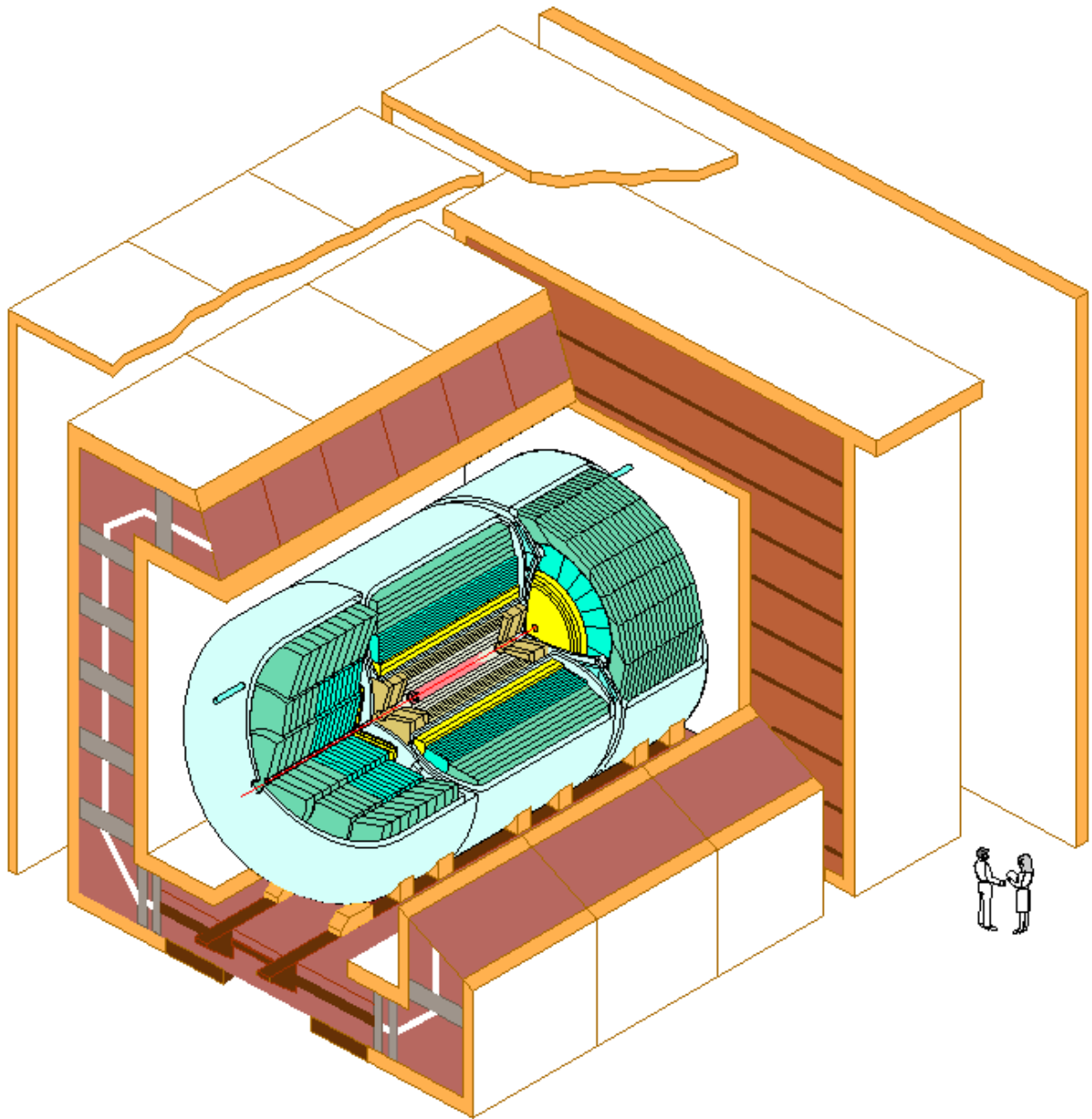


Figure 3.1 The D0 Detector has three main systems; from the inside out there is the central detector which includes tracking and vertexing, the calorimeter, and the muon system.

Detector coordinates

There are different coordinate systems that could be used with the DØ detector. The cylindrical symmetry of the detector suggests polar coordinates (r, ϕ, z) , but when the interaction is at rest, the event is spherical (r, θ, ϕ) . When the interaction is not at rest, so that one parton had more energy than the other parton in the interaction, the event is boosted in the lab frame. In this case, coordinates that are a Lorentz invariant would make simpler transformations under boosts. The coordinates used with the DØ detector that fit all of these criteria are a combination of the above (z, η, ϕ) . The z-axis is defined along the beam pipe with +z as the direction that the proton is traveling. It is primarily used in an event to define where the vertex of the event is, or where the interaction happened along the length of the detector. The other axes define the location of what is of interest in the event like a jet or a particle. The standard azimuthal angle is ϕ , which is always perpendicular to z. The pseudorapidity, η , is used instead of the polar angle, θ , because when the energy of a particle is much greater than its mass, it's approximately equal to rapidity, y , a Lorentz invariant. The pseudorapidity is related to θ by $\eta = -\ln(\tan(\theta/2))$. So $\eta = 0$ when $\theta = \pi/2$, and η goes to infinity at the beampipe as $\theta \rightarrow 0$. We also define a difference between detector pseudorapidity, η_d and physics pseudorapidity, η_p , where the latter shifts relative to the vertex of the event.

In $p\bar{p}$ physics much of the longitudinal momentum of the collision is lost down the beam pipe, so only transverse energy and momentum are conserved. The transverse energy can be defined as $E_t^2 = E^2 - p_z^2 = p_t^2 - m^2$ or $E = E_T \cosh(y)$, so that as the energy of a particle is much greater than its mass, where pseudorapidity is equivalent to rapidity, the E_t is also equivalent to p_t . The transverse momentum is defined in terms of the 3-momentum as $p_t = p \sin(\theta)$. Also in the limit $m \rightarrow 0$, the invariant mass of two massless particles can be calculated as $M_{12}^2 = 2E_{T1}E_{T2}(\cosh(\delta\eta) - \cos(\delta\phi))$.

Calorimeter

The DØ calorimeter was designed to have excellent discrimination and energy measurement of high P_T objects (electrons, photons, and jets). Since there is no magnetic field in the central detector, the calorimeter must produce the full kinematics and energy measurements of the event in addition to the jet profiles and particle detection. It has full pseudorapidity coverage out to a detector $|\eta| < 4.1$ and partial coverage (with reducing depth) out to $|\eta| = 5.2$. The calorimeter is divided into three segments (Figure 3.2). The central calorimeter (CC) covers $|\eta| < 1.0$, and the two identical end cap calorimeters (EC) cover $1.5 < |\eta| < 5.2$.

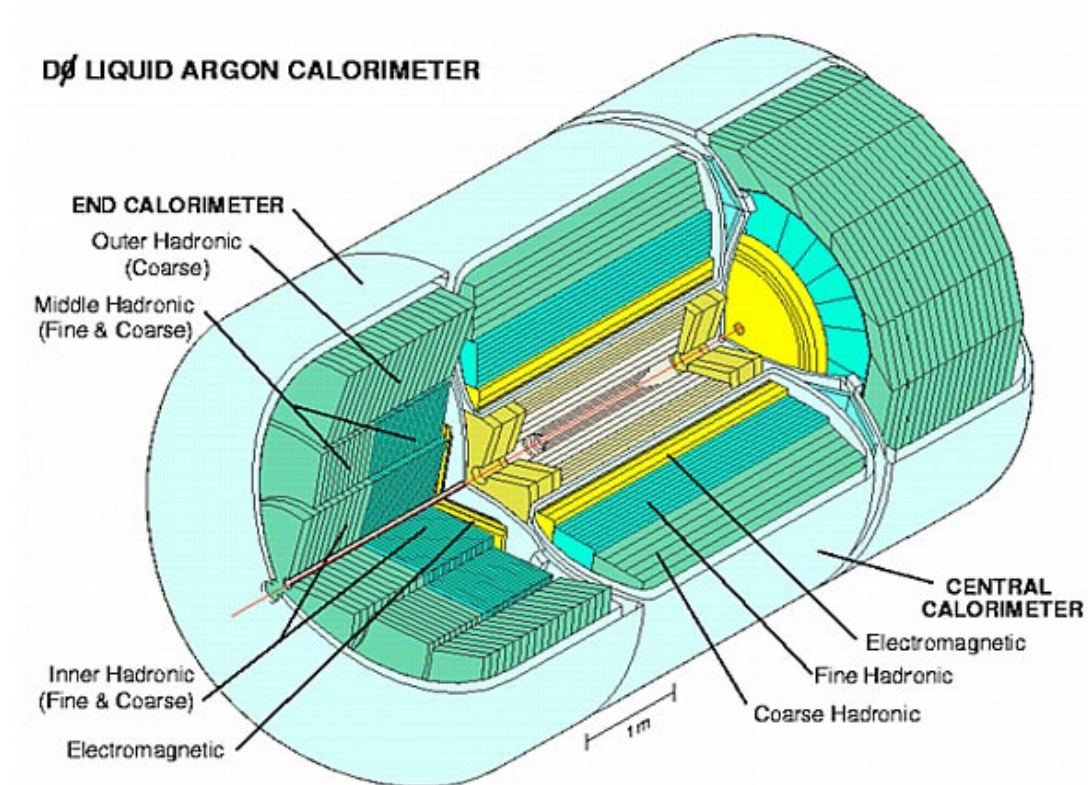


Figure 3.2 The DØ Calorimeter is divided into three parts: the central calorimeter (CC) and the two identical end cap calorimeters (EC). It has full coverage for $|\eta| < 4.1$.

The DØ calorimeter is a sampling calorimeter where the particles deposit a fraction of their energy in the liquid argon and that fraction is converted into a total energy measurement (See Figure 3.3). It uses primarily uranium, but also stainless steel or copper as the absorbing material and liquid argon as the ionizing sampling medium. As a high energy particle traverses the dense absorber, the particle interacts through electromagnetic and nuclear processes to produce a shower of particles. When the particles pass through the sampling layer, they ionize the argon, producing a charge that the electronics can detect and read out. Grouping many layers of absorber, sampling medium, and read-out boards improves the energy resolution.

Both the CC and EC have three distinct layers: the electromagnetic, EM, the Fine Hadronic (FH), and the Coarse Hadronic (CH) calorimeters. The EM section was designed to measure the energy of electromagnetic particles and absorb most of the energy from electromagnetic showers. It consists of thin uranium plates and is segmented into four longitudinal sections. In the CC it is read out at radiation lengths of 2.0, 2.0, 6.8, and 9.8 and in the EC at 0.3, 2.6, 7.9, and 9.3. The transverse

segmentation is $\delta\eta \times \delta\phi = 0.1 \times 0.1$, except for the third longitudinal layer in the CC which is segmented with $\delta\eta \times \delta\phi = 0.05 \times 0.05$. This provides increased position resolution since average electromagnetic showers deposit most of their energy in this layer. In the CC the EM section has full coverage out to $|\eta| = 1.2$ and in the EC the EM section has full coverage from $1.5 < |\eta| < 4.1$.

The fine hadronic section was designed to measure the energy of hadronic particles. It has thicker uranium plates and three longitudinal segments in the CC and four longitudinal segments in the EC. These layers give a total of about five interaction lengths. The coarse hadronic consists of at least one layer of very thick stainless steel or copper. It provides about four interaction lengths. The CH was designed for energy containment of the showers. The combination of the two hadronic calorimeters provides nearly full coverage in η_d .

Figure 3.4 shows the segmentation of the calorimeter in towers of η_d and $i\eta$, the data variable. The left side shows full coverage in all segments in the central calorimeter as well as the small gap in coverage from the CC to the EC. The segmentation is $\delta\eta \times \delta\phi = 0.1 \times 0.1$ in all detectors out to $i\eta = 32$ or $\eta_d = 3.2$. At large η the physical size of the slices in the detector becomes very small (see Figure 3.5) so it is necessary to group together towers of $\eta - \phi$. This happens from $i\eta = 33$ to 37 and conversions from $i\eta$ to η_d are shown in Table 3.1.

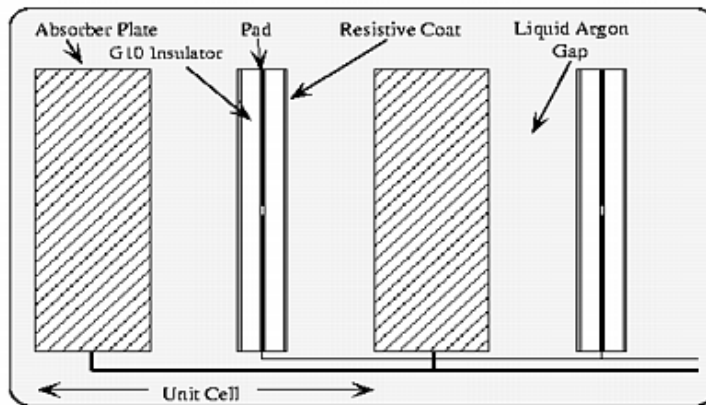


Figure 3.3 A sample calorimeter cell showing uranium as the absorbing medium and liquid argon as the ionizing medium. As a particle traverses the absorber, the particle showers and ionizes the argon which produces a charge.

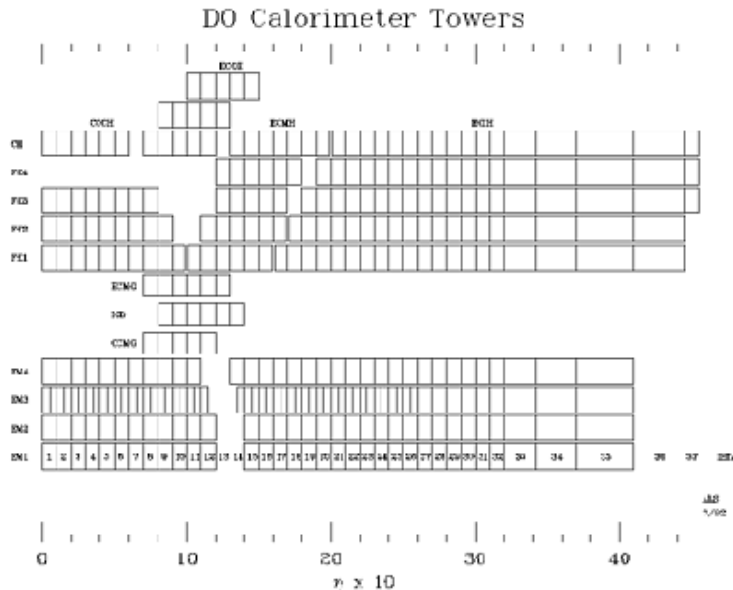


Figure 3.4 The segmentation of the calorimeter cell in detector eta and ieta. The segmentation is $\delta\eta \times \delta\phi = 0.1 \times 0.1$ in EM and HAD out to $ieta = 32$ or $\eta_d = 3.2$. Due to the physical size, larger values of $ieta$ are ganged together and correspond to even larger η_d

Intercryostat detectors

In the region between the CC and EC calorimeters, roughly from $0.8 \leq |\eta| \leq 1.4$, the EM and FHD calorimeters are only partially instrumented. Two different kinds of detectors were installed in this area to lessen the dead space and to correct for the energy deposited in the uninstrumented region. Scintillation counter arrays called Intercryostat Detectors (ICD) were mounted on the front surface of the end calorimeters. Each ICD has 384 scintillator tiles with $\eta \times \phi = 0.1 \times 0.1$ to match the calorimeter coverage. The other detector is the Massless Gaps, which are signal boards with no absorber. They are surrounded by liquid argon and measure charge in the same way as the calorimeter. They are mounted inside the cryostats on the outer surfaces of the hadronic calorimeters.

L0 detector

The primary purpose of the L0 detector is triggering on inelastic collisions. It consists of two hodoscopes of scintillation tiles that are mounted on each calorimeter endcap and surround the beam

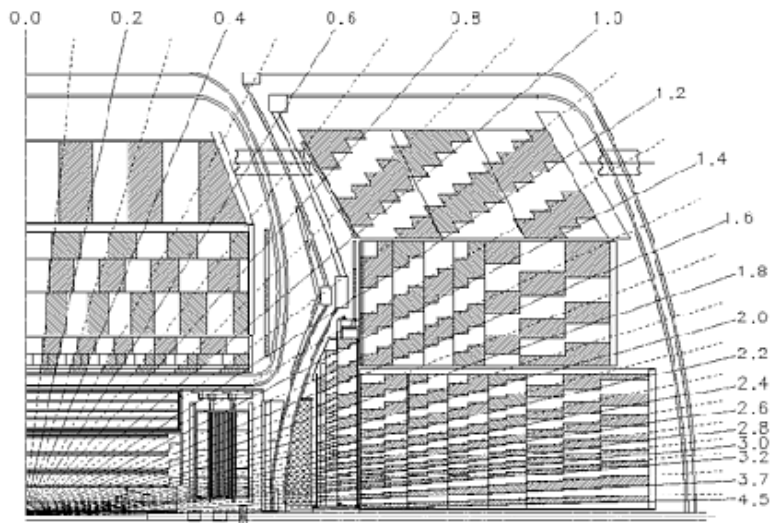


Figure 3.5 A side view of the calorimeter, showing the segmentation and slices in pseudorapidity space.

pipe at forward pseudorapidities. A coincidence in both detectors is a good trigger for an inelastic collision. In addition, it can also be used as an additional method to determine the position of the z -vertex from the timing difference between the north and south detectors. The detectors, pictured in Figure 3.6, each have two different types of scintillator tiles.

There are 20 “short” scintillator tiles which are closest to the beam pipe and measure $7 \times 7 \text{cm}^2$ each. The “long” hodoscopes are at a slightly lower pseudorapidity and have 8 scintillator tiles that measure $7 \times 65 \text{cm}^2$ each. Each array partially covers a region in pseudorapidity of $1.9 < |\eta| < 4.3$, with nearly total coverage from $2.2 < |\eta| < 3.9$. In this analysis, where we are interested in forward rapidity gaps or lack of particle production, we use the L0 detector “short,” tiles. We can also use the L0 detector to trigger on events where the “short” hodoscopes do not fire. Figure 3.6 shows a single diffractive candidate event. It has two jets and hits on one side of the detector and a rapidity gap on the left side of the detector. By triggering on events with no hits in the L0 detector along with concurrent jet production in the calorimeter, we can acquire a large sample of hard single diffractive events to study the event characteristics.

Table 3.1 Units of ieta to pseudorapidity

Ieta	pseudorapidity
33	3.20-3.42
34	3.42-3.70
35	3.70-4.10
36	4.10-4.45
37	4.45 up to 5.2

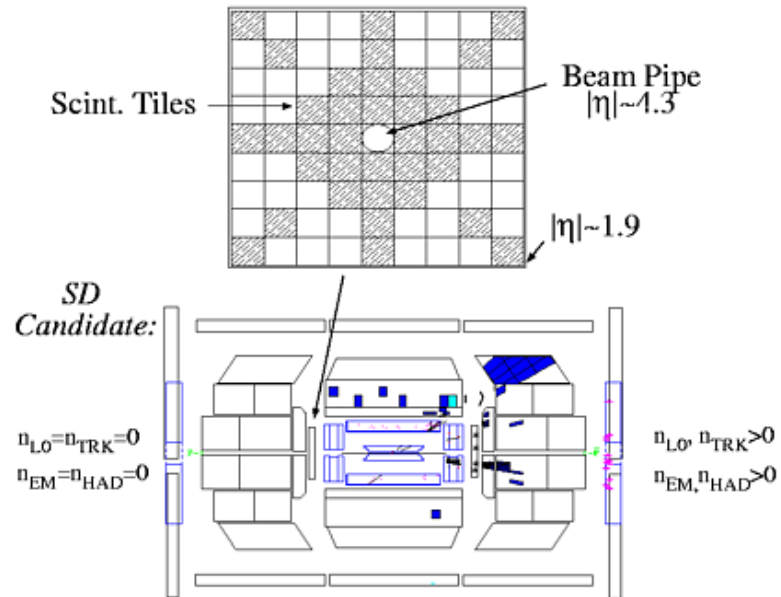


Figure 3.6 The L0 detector consists of scintillator tiles (shaded region) surrounding the beampipe.

Rapidity gap tagging

The method of analysis is to examine particle multiplicity distributions in the forward detectors (L0 and calorimeter sections) to search for a class of events with very low multiplicities on one side. This forward rapidity gap along with two jets is the signature for hard single diffraction.

In an analogous way to previous rapidity gap analyses [24, 25, 26], we actually measure forward calorimeter tower multiplicities in the forward detector η ranges above an imposed energy threshold. This differs from the previous central gap analyses which used only the electromagnetic calorimeter and applied a 200 MeV E_T cut to central towers in making multiplicity distributions. Since this is effectively a very hard cut on particle energy in forward regions, we instead set the threshold with *energy* for each calorimeter tower. For each event the CAEQ bank is used to construct a CATE bank containing nonsuppressed tower energy information used throughout this analysis. In the forward detector where we look for a rapidity gap, we use the forward EM calorimeter which ranges from (-4.1,-2) and/or (2,4.1), the forward hadronic calorimeter from ($\pm 3.2, \pm 5.2$), as well as the L0 short scintillator tiles to measure multiplicities.

We use three rapidity gap definitions to search for diffractive signals in the hard single diffractive and hard double pomeron exchange analyses. In all studies, the same thresholds are used: the EM threshold is 150 MeV, the FHD is 500 MeV, and the IH15 is 50 MeV in energy, but different η ranges are used to probe the nature of the pomeron in different states.

- $2.0 \leq \eta \leq 4.1$ or $-4.1 \leq \eta \leq -2.0$ (**Near Gap**)
- $2.0 \leq \eta \leq 5.2$ or $-5.2 \leq \eta \leq -2.0$ (**Long Gap**)
- $3.0 \leq \eta \leq 5.2$ or $-5.2 \leq \eta \leq -3.0$ (**Far Gap**)

For the near gap we use only the EM, and for the long gap and far gap all three detectors are used. EM covers $2.0 \leq |\eta| \leq 4.1$ and the FHD and IH15 cover $2.0 \leq |\eta| \leq 5.2$. The calorimeter multiplicities are combined in each region to define n_{CAL} , the total number of calorimeter towers hit above threshold.

Of the three rapidity gap definitions, the far gap in most studies is the preferred rapidity gap region. It is farthest away from the hard scattering region and closest to the beampipe.

Threshold

When we plot the multiplicity in a region by counting the number of calorimeter towers greater than threshold, choosing the “threshold” becomes an important factor. If the threshold is too high,

then we are not efficient at finding particles. As a result the overall multiplicity in the non-diffractive region will be low and will merge into any diffractive signal at zero multiplicity. (At the extreme, if the threshold is far too high then we are not efficient at finding anything and we get a spike at zero multiplicity!) A low overall multiplicity makes it difficult to use to differentiate between diffraction and the non-diffractive background and creates a larger than necessary fitting error in the measurement of the single diffractive signal. Alternatively, if the threshold is too low then detector noise is counted in the multiplicity. Instead of a signal-spike at zero, there is a peak over a few units. This again makes extracting the signal difficult. Ideally, we would like a threshold just above the noise where we will have good sensitivity to particles and ruin a minimum number of rapidity gaps due to noise.

The data set that we use for this study is a zero-bias run, number 76317. It is a special low luminosity run where data were taken during random beam crossings, so we can select “events“ where no interaction took place to give a good idea of the detector noise during running. The cuts to define a no-interaction event are no hits in the forward or central tracking ($nfdc + ncdc = 0$) and no hits in the level 0 detector ($nhits_scn + nhits_scs + nhits_lcn + nhits_lcs + time_n + time_s = 0$). There are 28710 events with these cuts. We also define a loose interaction-cut where both north and south level-0 counters fired in time ($l0_fastf = true$) to compare our no-interaction sample with, and there are 8694 events in this sample.

We separate the calorimeter into three different detectors with different thresholds: the electromagnetic calorimeter (EM), the forward hadronic calorimeter (FHD), and the last layer of the forward hadronic calorimeter (IH15). The coverage of the EM is from ieta of 21 to 35, corresponding to a pseudorapidity of 2.0 to 4.1, and that of the FHD is from ieta 33 to 37, corresponding to a pseudorapidity of 3.2 up to 5.2 in the very last layer. The IH15, this last layer of the FHD, is treated as a separate detector because it is made out of stainless steel instead of uranium. This makes it extremely quiet compared to the FHD so we can achieve greater sensitivity by reducing the threshold with negligible double counting.

Qualitatively, the noise decreases from ieta 21 to 32 ($2.0 < \eta < 3.2$) because the physical size of the calorimeter cells decreases while the towers span a constant physics η range of 0.1 unit. From ieta 33 to 37 ($3.2 < \eta < 5.2$) the noise begins to increase because more units of pseudorapidity are ganged together into a slice of ieta, as shown in Table 3.1.

The no-interaction sample, after hot cells are removed, contains only noise. (Hot cells are towers during the run that continually misfire with some energy.) Figure 3.7 we plot for each detector the fraction of events out of the total sample that have one or more towers greater than a particular

threshold. (We do this separately for the north side of the detector and the south side of the detector and combine them for these figures since they are very similar.) This is the fraction of events that would no longer have zero multiplicity due to noise effects. At a very low threshold all of the detectors have noise in every event, but as the threshold increases, the fraction of events with noise falls quickly to a fairly stable value. We would like to have the lowest threshold possible where we are not on the rapidly falling curve and where the number of rapidity gaps events spoiled due to noise is about a percent. These conditions are satisfied at a threshold of 150 MeV for the EM, 500 MeV for the FHD, and 50 MeV for IH15, with 2.0%, 2.0%, and 0.2% noise at each at those thresholds, respectively. We do not correct the data for this low noise rate because in extracting the signal we integrate over the first couple of multiplicity bins above a fit. If we were only to take those events in the zero bin as single diffractive events, then we would have to make the correction for noise.

As a cross-check for these thresholds we would like to verify that we are still efficient at tagging particles when there is an interaction. Figure 3.8 shows the same plots as before but with the interaction-cut selected instead. This means that when there is a non-diffractive interaction it gives the fraction of the time that we have at least one tower greater than threshold. For the EM, we are about 99.8% efficient and for the FHD we are approximately 98.7% efficient. For the IH15, unfortunately, this cross-check is not very effective because few particles will reach to the last layer of the FHD in an event. That means that the number on the graph, about 57% is a product of acceptance (or how frequently particles reach the IH15) as well as the efficiency.

Noise Studies

We can use the zero-bias data to measure how often the different rapidity gap regions are spoiled due to noise. Shown in Figure 3.9 is a 2-dimensional plot of the number of towers greater than threshold in all calorimeters (NCAL) and the number of scintillator tiles hit. The majority of the events are in the $(0, 0)$ bin, showing that very few gaps are ruined from noise, and those only in the calorimeter, not the L0 detector. Running over noise events for the near gap, long gap, and far gap, about 1.3%, 3.8%, and 3.7% of events smear out of the $(0, 0)$ bin, and most of these only into the $0 - 1$ bin. In data we fit over a large number of bins to extract the signal. Since noise is spread throughout diffractive as well as non-diffractive samples, no correction should be needed from noise ruining rapidity gaps. We cross-check this in the data measurement later.

A powerful crosscheck of the efficacy of the gap tagging method may be accomplished by going to very low threshold for counting towers for the multiplicity distributions. Figure 3.10 shows the forward

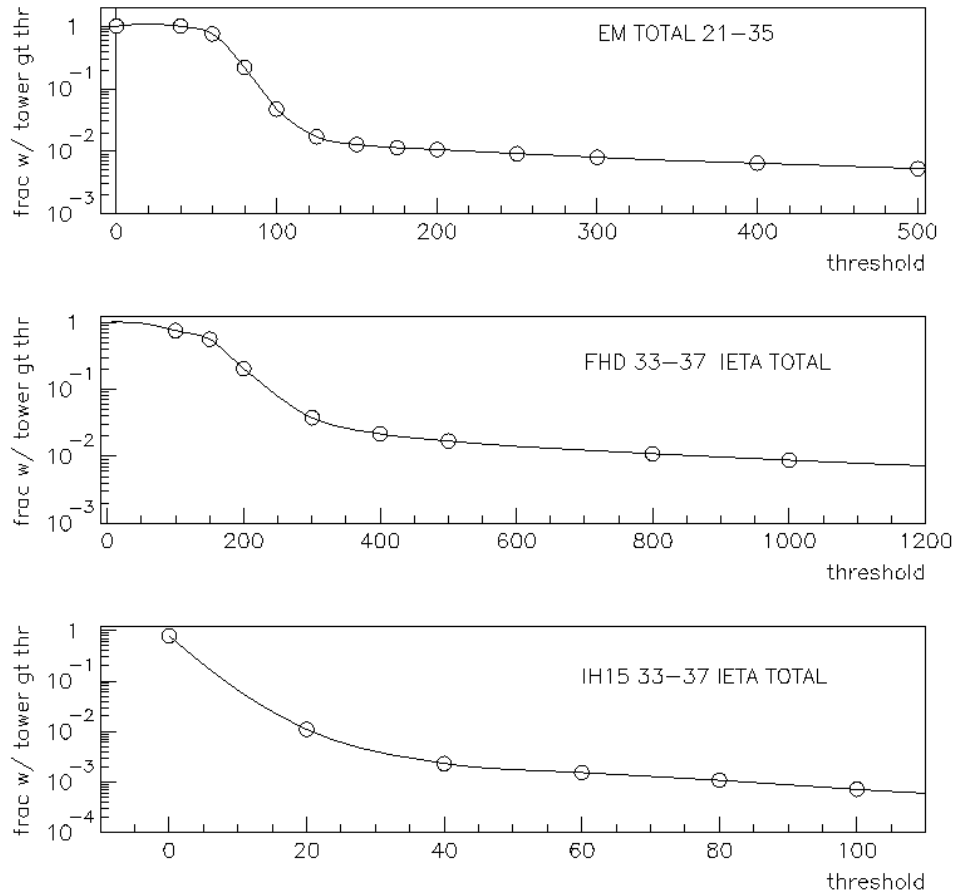


Figure 3.7 Fraction of events with one or more tower greater than threshold due to noise versus threshold. The threshold to be above most of the noise for EM is 150 MeV, for FHD is 500 MeV, and for IH15 is 50 MeV.

multiplicity distribution using only the EM calorimeter with a threshold of 200 MeV. In Figure 3.11 we show the same distribution with the threshold lowered to 60 MeV. The mean multiplicity at 60 MeV is higher as expected because it is sensitive to more particles as well as noise. Two peaks are evident in both samples, where the low peak again represents the rapidity gap events, now spread out by calorimeter noise. Figure 3.12 shows a noise distribution for the same calorimeter region overlaid with the forward trigger sample multiplicities. The noise was obtained from a zero bias run at low luminosity with cuts to remove events with a $p\bar{p}$ interaction from the sample (no L0 hits, no central tracks, no fdc tracks). The rapidity gap peak in the distribution is observed to be in good agreement with the noise distribution. A check with the INCLUSIVE trigger sample shows the measured signal to be consistent

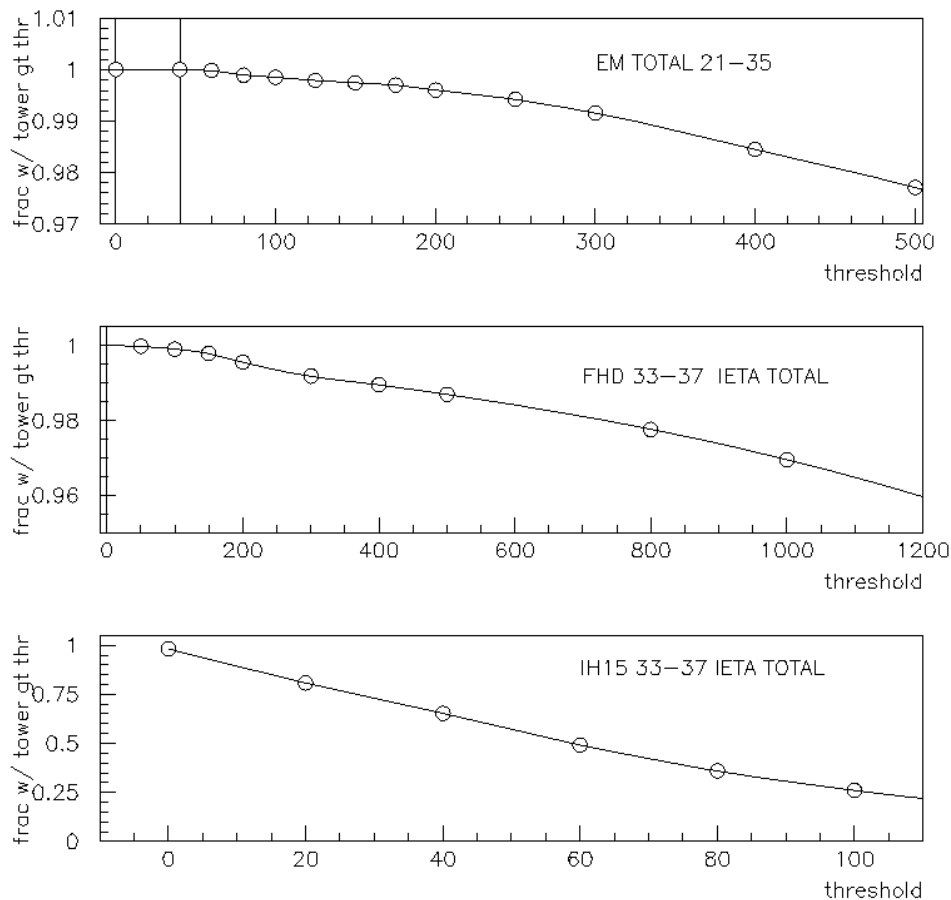


Figure 3.8 Fraction of events with one or more tower greater than threshold versus threshold if there is an interaction. This can provide a measure of efficiency for tagging particles in the EM and FHD case.

between the 200 MeV threshold and 60 MeV threshold multiplicity distributions (about .25% for the 200 MeV threshold and about .20% for the 60 MeV threshold).

This means that in events with two jets in them and a rapidity gap, the rapidity gap has nothing in it. It is consistent with only having noise in that section of the calorimeter. Measuring above a fit even when the distribution is smeared from noise produces a consistent gap fraction.

PYTHIA studies shown in the Monte Carlo section clearly predict a smoothly falling particle multiplicity distribution approaching zero multiplicity for events with jets passing our E_T requirements for non-diffractive physics processes. A similar study using POMPYT (a modified version of PYTHIA which calculates hard scattering of a proton with various Pomeron models) predicts forward particle multiplicity distributions which are strongly peaked at zero.

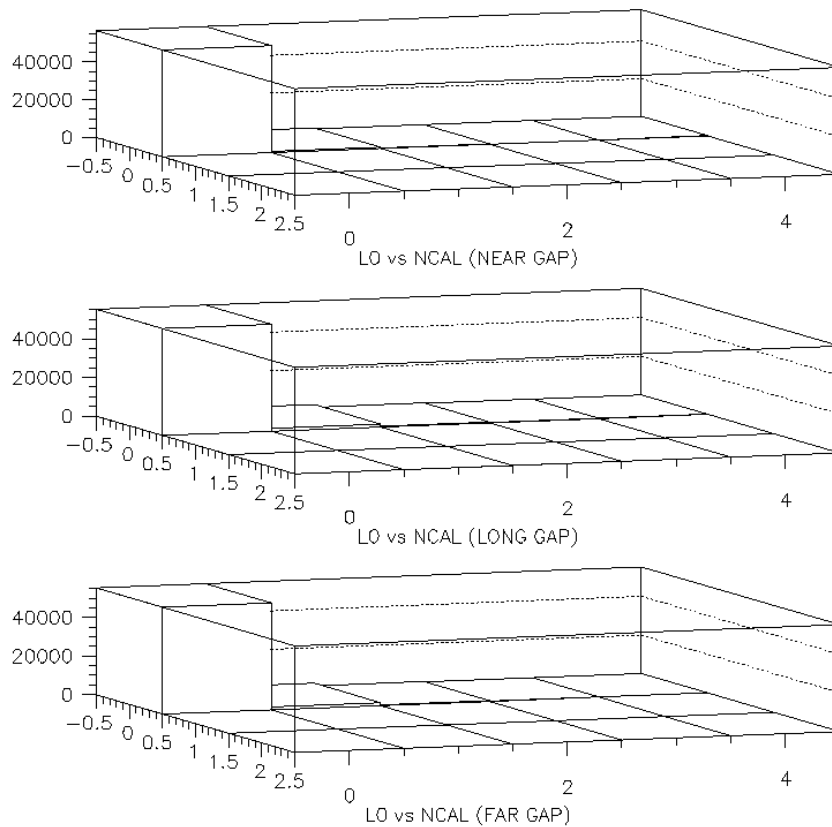


Figure 3.9 The multiplicity of L0 and calorimeter towers above threshold over a data-set containing only noise. In all three rapidity gap definitions, very few rapidity gaps are ruined due to noise.

The data show features of both Monte Carlo distributions and is assumed to be composed of two independent samples: a sample of non-diffractive jet events produced via color exchange processes and a hard single diffractive sample produced via a colorless exchange.

We fit simultaneous functions to the diffractive and non-diffractive data to extract the fraction of diffractive jet events. We measure the fraction of diffractive events as the number in the signal fit divided by the total number of events.

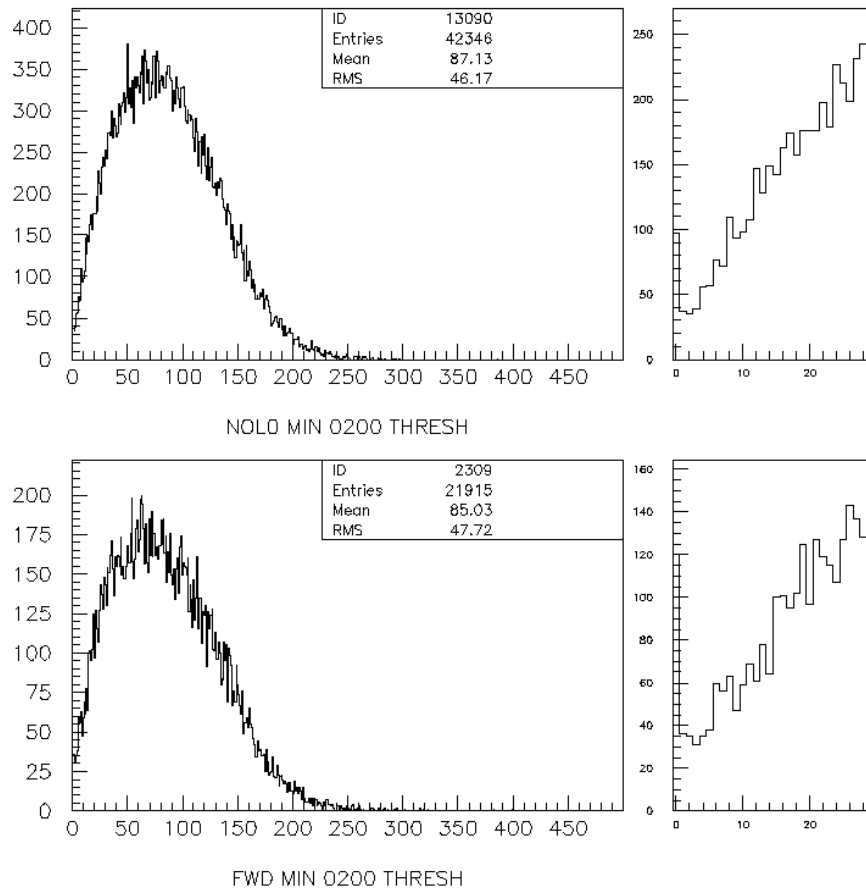
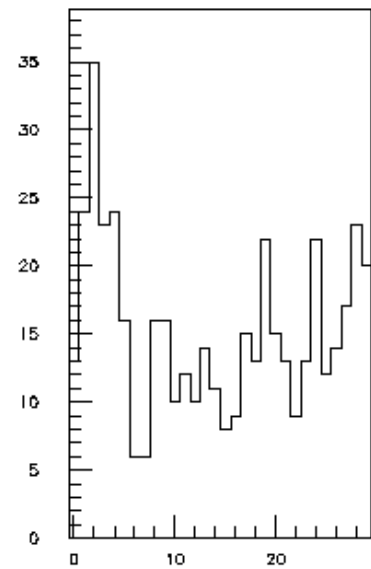
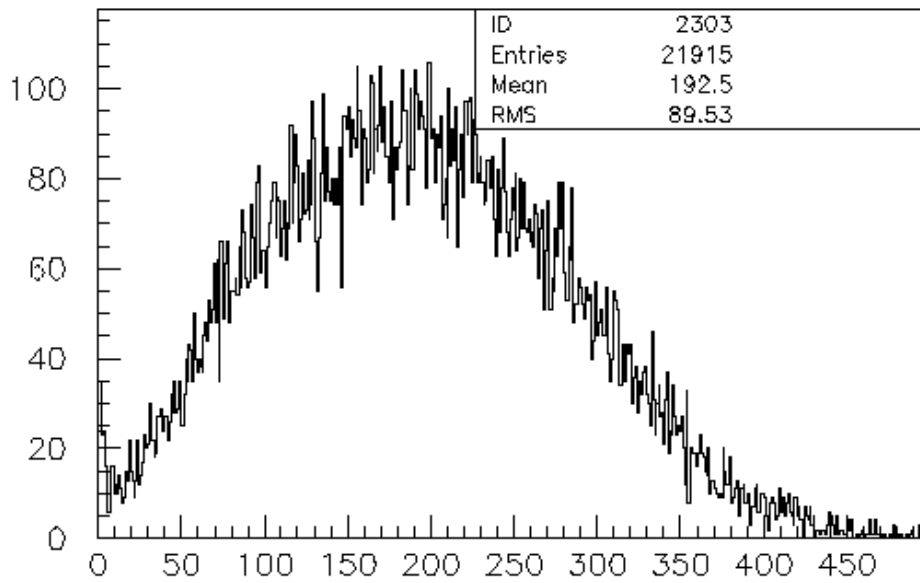
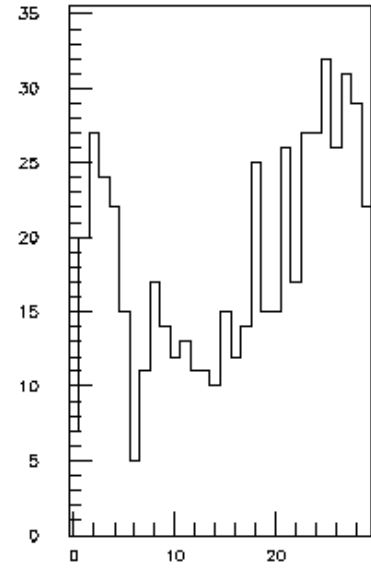
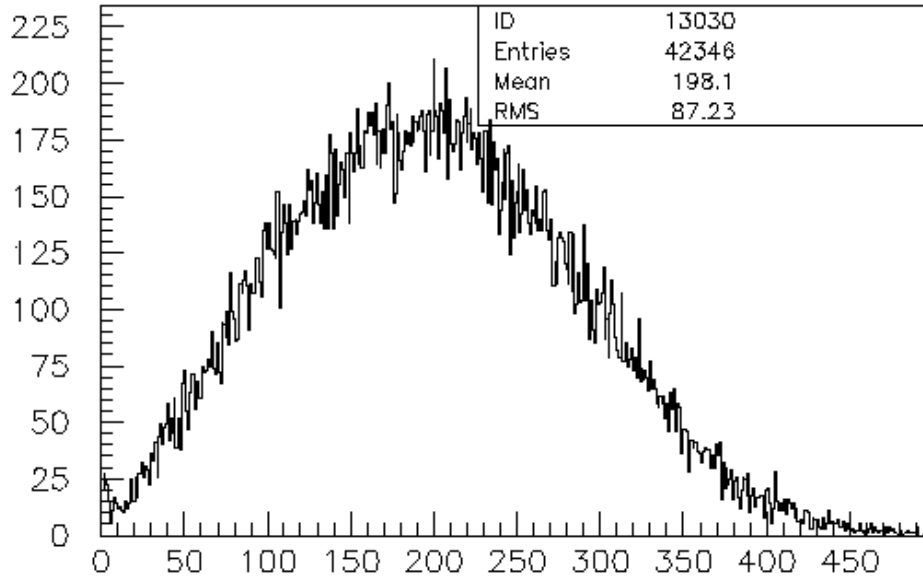


Figure 3.10 Multiplicity Distribution for inclusive and forward trigger samples with a 200 MeV tower threshold



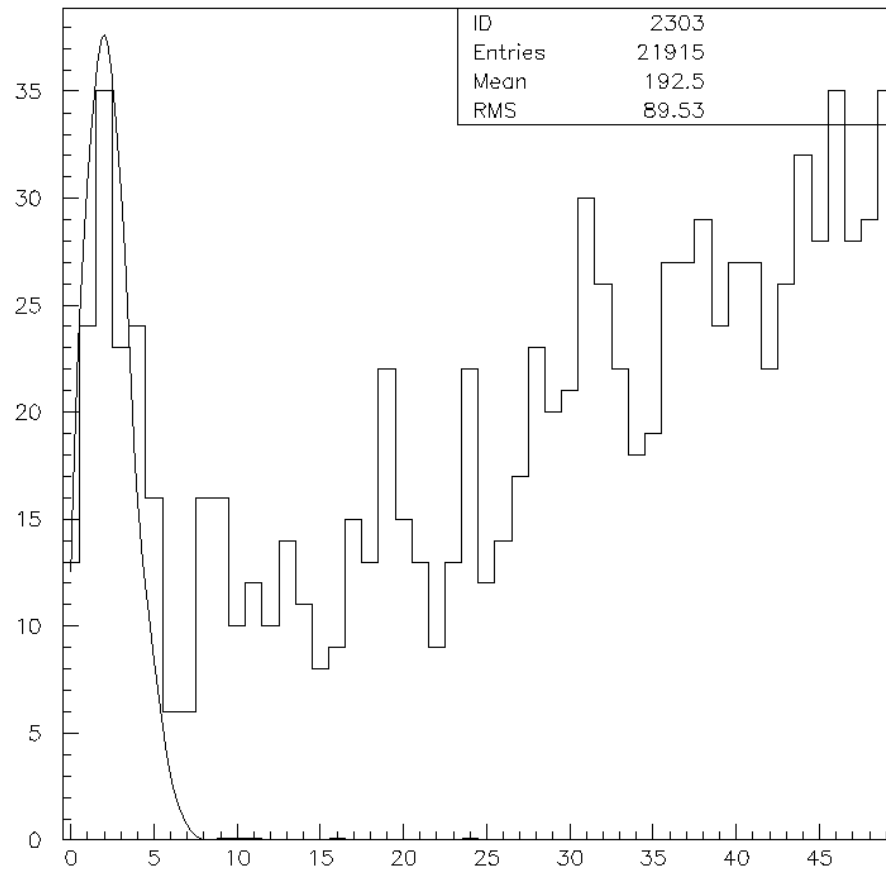


Figure 3.12 Noise from Zero bias overlaid with the 60MeV threshold multiplicity distribution for forward sample.

4 MONTE CARLO

POMPYPY [30] is a Monte Carlo created by Bruni and Ingelman to model hard single diffractive scattering at the particle level. It is based on PYTHIA [31] and it produces pomeron-proton collisions at different center-of-mass energies and different pomeron fluxes. It also includes structure functions for the pomeron models proposed by Ingelman and Schlein of two “hard” gluons or two quarks sharing the pomeron’s momentum, $xG(x) \simeq x(1-x)$, a flat gluon function (proportional to one) and a conglomerate of “soft” gluons like the average gluon distribution in the proton with $xG(x) = 6x(1-x)^5$. POMPYPY26 is the latest version of POMPYPY which can allow for more sophisticated pomeron structures including Q^2 evolution and the possibility to input structures derived at Hera. In this paper, we will use POMPYPY to study the efficiency of the rapidity gap method to tag diffractive events, the distribution of the momentum given to the pomeron by the proton (ξ), the predicted rates for diffraction (POMPYPY/PYTHIA), as well as the model dependence of these and other quantities. We can also examine some general properties of the Ingelman-Schlein model and motivate our method of analysis.

Method

There are two classes of hard single diffractive events that we examine: those with forward jets and those with central jets. The forward jet data trigger requires at least two jets above $E_T = 12 \text{ GeV}$ in the region $\eta > 1.6$ or $\eta < -1.6$. Because the pomeron typically carries less than 5% of the incident proton momentum, the jet system is expected to be slightly boosted in the lab frame and a rapidity gap is expected on the side opposite the jets. POMPYPY models a proton-pomeron collision with the pomeron as the beam particle coming from the north, so the system will always be boosted in the same direction. To correspond with the data, the cuts on Monte Carlo forward jets are at least two jets above $E_T = 12 \text{ GeV}$ in the region $\eta < -1.6$. Figure 4.1 shows the η distribution at 1800 GeV for different POMPYPY structure functions. The structure functions for the soft gluons are $xG(x) \sim x(1-x)^5$, while those for the hard gluons and quarks are $xG(x) \sim x(1-x)$, so the soft gluons on average have a much lower x or much less momentum than the hard gluons, resulting in an even larger boost. (The

η distribution does not distinguish between the hard gluons and quarks because they have similar structure functions in POMPYT.) Figure 4.2 shows the η distribution for the two leading jets again for the center-of-mass energy 630 GeV. This looks very similar to the 1800 GeV center-of-mass energy as might be expected because the pomeron is provided with the same percentage of the proton's energy, but the peaks are narrower because a given E_T requires a larger parton x at 630 GeV which is suppressed in the proton parton density function (pdf).

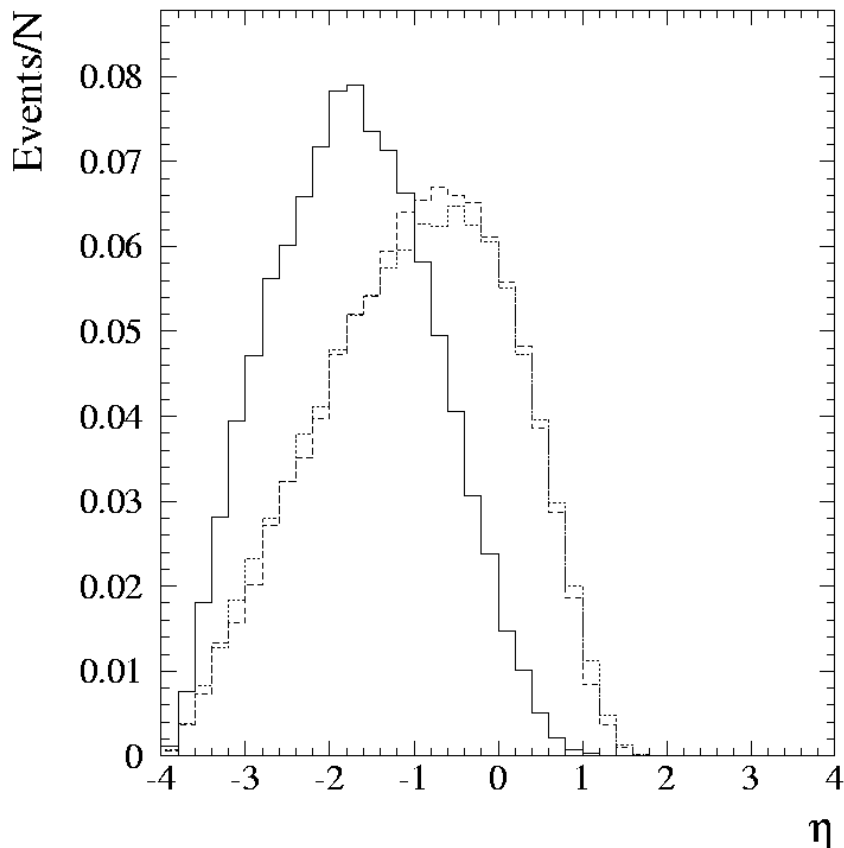


Figure 4.1 The η distribution at $\sqrt{s} = 1800$ GeV for soft gluons (solid line), hard gluons (dashed line), and quarks (dotted line) structures.

For the forward jet samples the multiplicity is plotted on the side opposite the jets. The central jet data set comes from an inclusive trigger with no η cuts. We require off-line two jets above 15 GeV (12 GeV at 630) in the central region $|\eta| < 1.1$. Since there is no preferred side for a rapidity gap like in the forward jet sample, we plot the multiplicity on the minimum side to search for rapidity gaps.

The particle multiplicity for POMPYT and PYTHIA forward jets (far gap) are shown in Figure 4.3

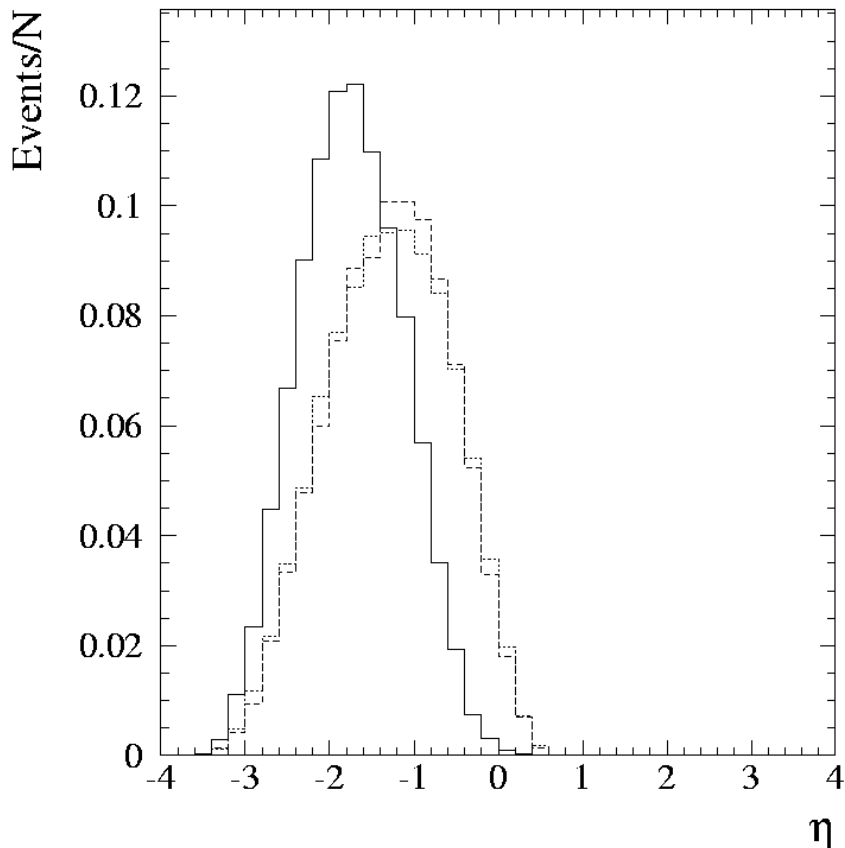


Figure 4.2 The η distribution at $\sqrt{s} = 630$ GeV for soft gluons (solid line), hard gluons (dashed line), and quarks (dotted line) structures.

for particles with an energy greater than 700 MeV. (This threshold simulates the calorimeter threshold.) The diffractive signal from POMPYT is strongly peaked at zero with a small tail extending to higher multiplicities. PYTHIA shows a larger mean-multiplicity peak that tapers off to zero on both sides of the distribution. The diffractive distribution is clearly distinguishable from the non-diffractive distribution, so multiplicity is a good variable to tag rapidity gaps and diffraction.

Initial POMPYT results were focused at the particle level, so instead of counting EM towers or FHD towers, we were actually counting particles. However POMPYT has been incorporated into the DØ zebra structure so now events can be run through detector simulation, and we have a basis for comparison to real data. Figure 4.4 shows the analogous multiplicity distributions for the POMPYT and PYTHIA after full detector simulation. It is a two-dimensional plot with the number of calorimeter towers above threshold (the same used in data) and the number of L0 tiles hit. The POMPYT multiplicity is even

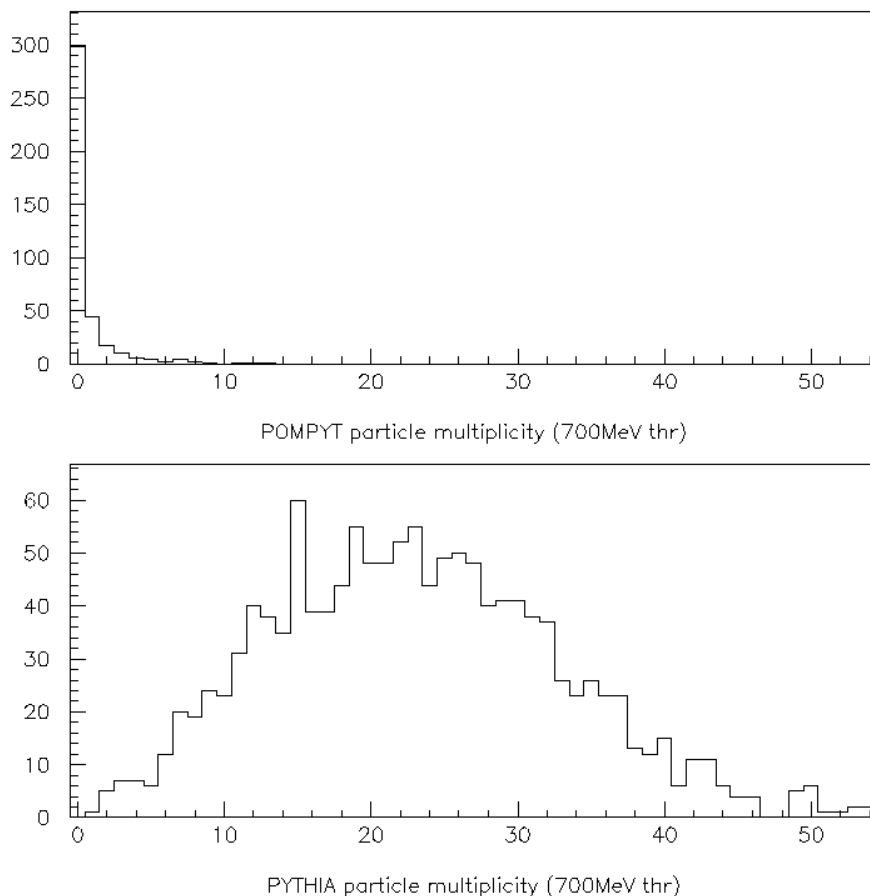


Figure 4.3 The multiplicity of particles with an energy greater than 700 MeV for the far gap with both POMPYT and PYTHIA. The POMPYT multiplicity distribution is peaked at zero, while the PYTHIA multiplicity is peaked farther out and tapers off to zero at zero multiplicity.

more strongly peaked at $(0,0)$ because we are not detecting every particle, and PYTHIA again tapers off to zero near the $(0,0)$ multiplicity bin. The multiplicity distributions for the other gap regions and for central jets are similar in character.

The relationship of particle multiplicity to calorimeter tower multiplicity is complex. One high energy particle will generally hit several different towers with a wide shower, increasing the multiplicity. Then some of the soft energy particles might be below threshold and not included in the measurement. In addition, in the far gap and long gap regions there is a small overlap between with the EM and FHD detectors, which results in higher multiplicity. On average the multiplicities after full detector simulation are higher, and they more closely reflect the data. All Monte Carlo plots hereafter will have

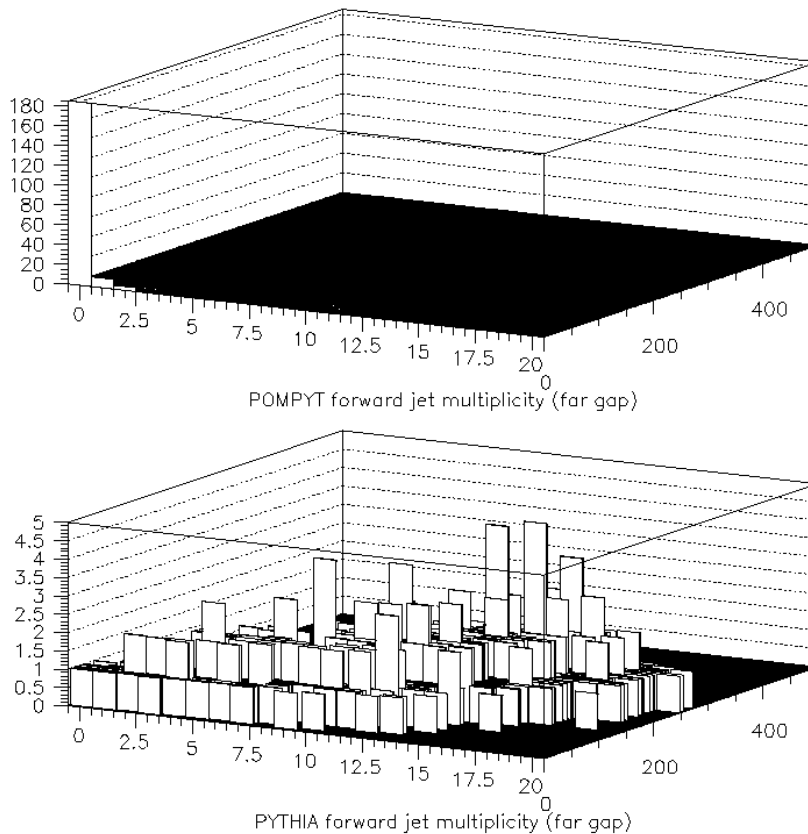


Figure 4.4 The two dimensional (L0 vs. N_{CAL}) multiplicity distributions for POMPYT (upper) with the hard gluon structure function and for PYTHIA (lower) after full detector simulation.

been run through full detector simulation unless otherwise noted.

Gap Efficiency

We want to measure the fraction of diffractive dijets to all dijets, and compare to data. However, with the rapidity gap method we will not tag every diffractive event because some of the time a particle from the interaction will spray into the rapidity gap region. This is the tail of the multiplicity plots shown earlier. To calculate the visible fraction of diffractive dijets to all dijets in order to be able to compare to data, we will need to correct for the efficiency of the method for tagging a pomeron, or how often the diffractive interaction will meet the criteria we defined for a rapidity gap. (This number will obviously vary depending on which rapidity gap definition we are measuring.) We call the efficiency of

tagging the gap the “gap efficiency”, so $f_{\text{visible}} = f_{\text{true}} \times \varepsilon_{\text{gap}}$.

There are two ways that we could extract the gap fraction from the data. We could consider only events in the zero-zero multiplicity bin and have a moderate gap efficiency correction or we could consider events in more bins of multiplicity and have a higher gap efficiency for extracting signal with a lower correction. The gap efficiency has a large model dependence, so if we take the latter approach we will have a less model-dependent measurement. We do this by fitting over the non-diffractive multiplicity as well as the diffractive signal simultaneously. Our fraction then is the number of events in the signal fit divided by the total number of events. (See data section for a description of the fits to the multiplicity distributions.)

To estimate the gap efficiency we add the POMPYT multiplicities for a particular sample to a background fit from the analogous data. (This does assume that there are comparatively few gap events left in the background fit.) A new fit is performed and the number of measured POMPYT events is extracted and compared to the original number added. The nominal gap efficiency is the number of events that we measure after the fit divided by the number of signal events. The fitting systematic error (only for the gap efficiency) is found by varying each bin in the background by a gaussian distributed random number times \sqrt{N} . The new varied background is added to the POMPYT MC signal and a new fit is done. After several iterations, the error is the RMS of the gap efficiency found. There is an additional systematic error based on the energy scale difference between Monte Carlo and data. In other words, the 150 MeV EM threshold required in Monte Carlo might actually correspond to 160 MeV in data. This error is based on the jet energy scale difference known between Monte Carlo and data (it is discussed later on in more depth in the ξ distribution), and it is approximately 13%.

We should note that there is no difference in the Monte Carlo between the near gap and long gap because the diffracted proton is assumed to remain intact –so the rapidity gap extends down to the beam pipe. In data the difference between the near gap and the long gap will be a measure of how much double diffraction occurs. Double diffraction is when the outgoing diffracted proton becomes excited and breaks into a low-mass state. Table 4.1 shows the gap efficiency for the hard gluons at $\sqrt{s} = 1800$ and 630 GeV with the long and far rapidity gap multiplicity ranges for a forward and central jet η distribution. Figure 4.5 shows the corresponding 1800 GeV multiplicity distributions. As the rapidity gap is moved closer to the hard scatter, the percent of events in the $(0, 0)$ bin decreases, so the gap efficiency increases. A higher mass system can spread out and ruin a long gap easier than it can ruin a far gap. The gap efficiency also decreases when the jets are moved closer to the gap region from the forward jet to central jet systems. This is as expected since the hard mass system is closer

to the gap region. At $\sqrt{s} = 630 \text{ GeV}$ there is less total center-of-mass energy and the gap efficiency is correspondingly higher. The multiplicity distributions at 630 GeV are shown in Figure 4.6. This is consistent with the picture that at 630 GeV to get the same jet E_T as at 1800 GeV, will require a larger momentum parton of the pomeron. So there is less energy available in the underlying event to spread into the rapidity gap region.

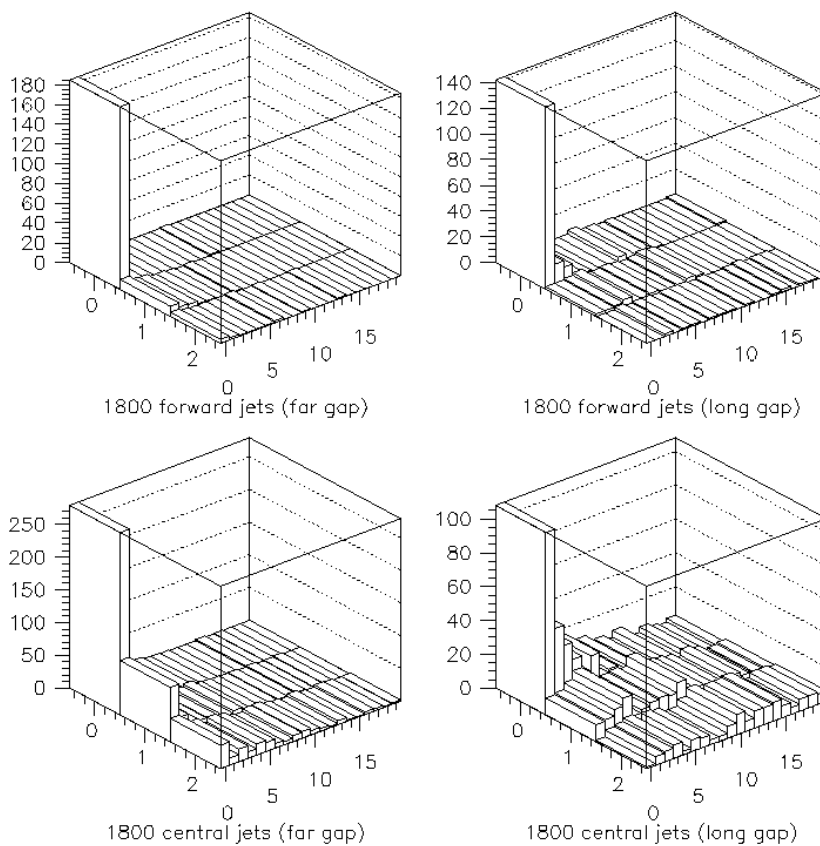


Figure 4.5 The multiplicity for 1800 GeV hard gluons in the long gap and far gap for forward and central jets. The gap efficiency is higher (less spread out of the $0 - 0$ bin) when the gap is farther away from the interaction region.

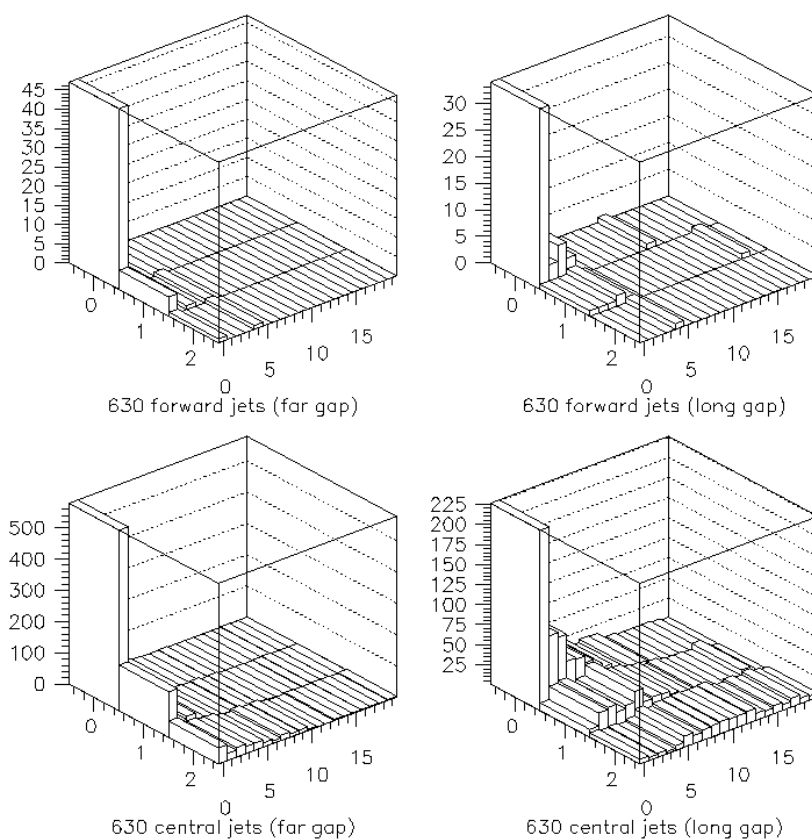


Figure 4.6 The multiplicity for 630 GeV hard gluons in the long gap and far gap for forward and central jets. As at 1800, the gap efficiency increases when the gap is farther away from the interaction region.

Table 4.1 Gap Efficiency for hard gluons with forward and central jets at both center-of-mass energies.

GAP REGION	1800 FORWARD	1800 CENTRAL	630 FORWARD	630 CENTRAL
FAR GAP	$74\% \pm 5\% \pm 10\%$	$40\% \pm 4\% \pm 5\%$	$85\% \pm 10\% \pm 11\%$	$49\% \pm 2\% \pm 6\%$
NEAR GAP	$61\% \pm 3\% \pm 8\%$	$13\% \pm 2\% \pm 2\%$	$65\% \pm 9\% \pm 8\%$	$15\% \pm 2\% \pm 2\%$
LONG GAP	$60\% \pm 4\% \pm 8\%$	$16\% \pm 2\% \pm 2\%$	$63\% \pm 4\% \pm 8\%$	$15\% \pm 2\% \pm 2\%$

The central jet events in general also have a pomeron that takes a higher momentum fraction from the proton, or a higher ξ . Requiring central jets forces the pomeron momentum to balance the momentum of the parton from the other proton. The higher mass system that results has a larger spread and can potentially ruin more rapidity gaps, so the gap efficiency also has a dependence on the ξ taken by the pomeron. Figure 4.7 shows the multiplicity distributions at 1800 GeV in four bins of ξ for central jets. The gap efficiency decreases as ξ is increased. The forward jets have a similar dependence, although it is less pronounced than the central jets. Forward jets typically have a smaller ξ than the central jets, because a pomeron with less momentum results in a higher boost. Correspondingly, forward jets have fewer events at higher ξ where the gap efficiency worsens. The central jets have a strong dependence on the pomeron ξ , which is similar at 630 GeV (not shown). Finding the ξ that is probed in data is important to measuring the proper central gap efficiency.

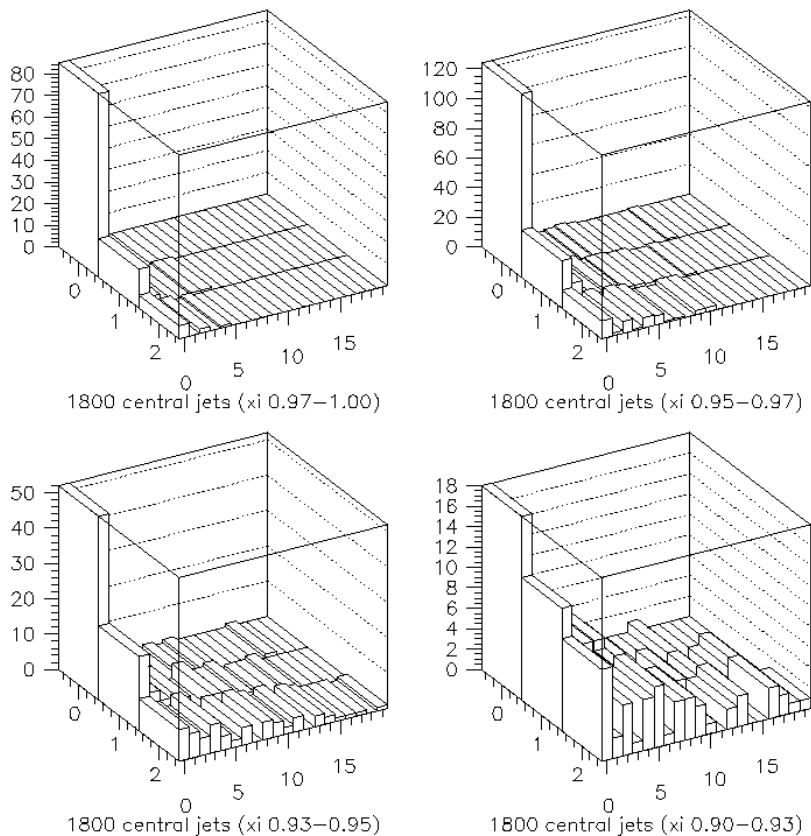


Figure 4.7 The MC central jet multiplicity at 1800 GeV in bins of ξ . The gap efficiency decreases as the ξ increases.

Table 4.2 shows the gap efficiency for the quark, flat gluon, and soft gluon structure functions. They show similar behavior as for the hard gluon, but become increasing lower overall. The pomeron structure functions measured at HERA and CDF seem to prefer a structure function that is mainly hard gluon.

We should note that the gap efficiency with the two-dimensional method is less than the gap efficiency that we had previously done with a one-dimensional n_{cal} only distribution. Previously we had taken the gap efficiency as the first six bins in n_{cal} divided by the total number of events. In the two-dimensional method where the signal is fit to a falling exponential, only the first couple of bins are taken as signal. The two-dimensional method provides more information for the fits and significantly reduces the error in background subtraction so there is a strong preference for that method, even though the gap efficiency is lower.

Table 4.2 Far gap efficiency for various structure functions with forward and central jets at both center-of-mass energies.

STRUCTURE FCN	1800 FORWARD	1800 CENTRAL	630 FORWARD	630 CENTRAL
HARD GLUON	$74\% \pm 5\% \pm 10\%$	$40\% \pm 4\% \pm 5\%$	$85\% \pm 10\% \pm 11\%$	$49\% \pm 2\% \pm 6\%$
FLAT GLUON	$66\% \pm 2\% \pm 9\%$	$56\% \pm 5\% \pm 7\%$	$70\% \pm 14\% \pm 9\%$	$60\% \pm 2\% \pm 8\%$
QUARKS	$58\% \pm 3\% \pm 8\%$	$18\% \pm 6\% \pm 2\%$	$53\% \pm 9\% \pm 7\%$	$25\% \pm 11\% \pm 3\%$
SOFT GLUON	$23\% \pm 4\% \pm 3\%$	$4\% \pm 3\% \pm 1\%$	$11\%pm8\% \pm 1\%$	$4\% \pm 4\% \pm 1\%$

ξ distribution

Differences in the gap efficiency are expected between the long gap and far gap. When the pomeron has more momentum, higher mass states can occur which spread out more in rapidity. These would spoil the long rapidity gap which is nearest to the jets, and as we move the edge of the rapidity gap farther away from the jets, more of these higher mass states would be allowed. Thus, when we study the far rapidity gap region as opposed to the long rapidity gap region, we are probing a slightly different state of the pomeron. This is also true when we look at forward jets and central jets. Central jets, which have no boost, tend to have a higher ξ distribution, so we are probing a higher momentum pomeron. Figure 4.8 shows the momentum distribution, ξ , of the pomeron for the hard gluon pomeron structure function with $E_T = 12 \text{ GeV}$ jets. (The ξ distribution without this jet E_T cut is peaked at zero, but the jet requirements bias against low mass, or low ξ , states.) The momentum given to the pomeron is $1 - x_p$, where x_p is the momentum fraction of the outgoing diffracted proton. The dashed line is the ξ

distribution if we require central jets and the dotted line if we require forward jets. The forward jet ξ distribution is peaked closer to zero, so that for most of the events the pomeron around 0.01% of the proton momentum. The ξ that is probed with the central jets is higher. Figure 4.9 shows the effect of requiring a long (dashed) or far (dotted) gap with forward and central jets. The effect of requiring the rapidity gap is that much of the higher mass states are excluded, and the far gap allows in higher mass pomeron states than the long gap. For the forward jets there is little difference between the long and far gap, so the gap efficiency does not change greatly. The central jet sample shows a larger difference and a greater effect. Figures 4.10 and 4.11 are the corresponding ξ distributions at $\sqrt{s} = 630$ GeV. A similar behavior is observed except the distribution extends to higher values of ξ .

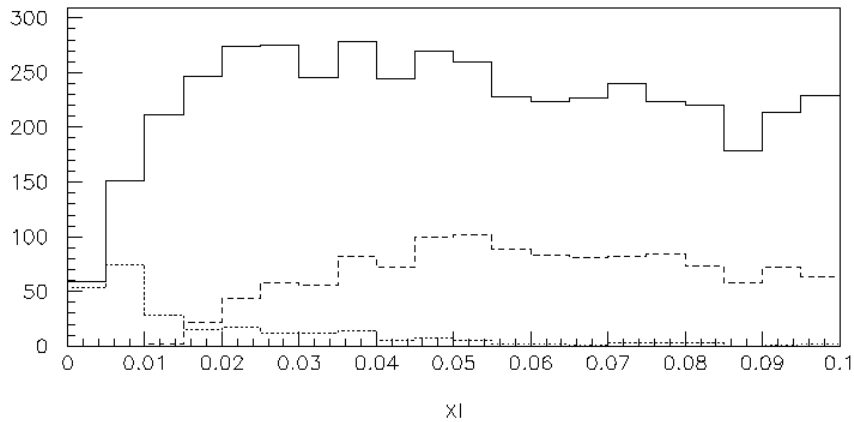


Figure 4.8 The ξ distribution for the hard gluon at 1800 GeV for all events (solid line) with 12 GeV jets. The dashed line is the ξ distribution if we require central jets and the dotted line for forward jets. The ξ region probed for the central jets is higher than for the forward jets.

Although a higher value of ξ is expected at 630 GeV than at 1800 GeV to produce the same jet E_T range, the range of ξ is much larger than would normally be expected in the Ingelman-Schlein model. The proton is expected to dissociate when it gives more than $\simeq 20\%$ of its momentum to the pomeron. The pomeron dominated region is normally $\xi < 0.05$ to $\xi < 0.10$, with large backgrounds from Reggeon exchange for $\xi > 0.1$. The pomeron ξ distribution at 630 GeV extends out to $\xi = 0.2$! To get a better estimate of the rates and the gap efficiency, it would be best to measure what ξ range is actually being probed in the data.

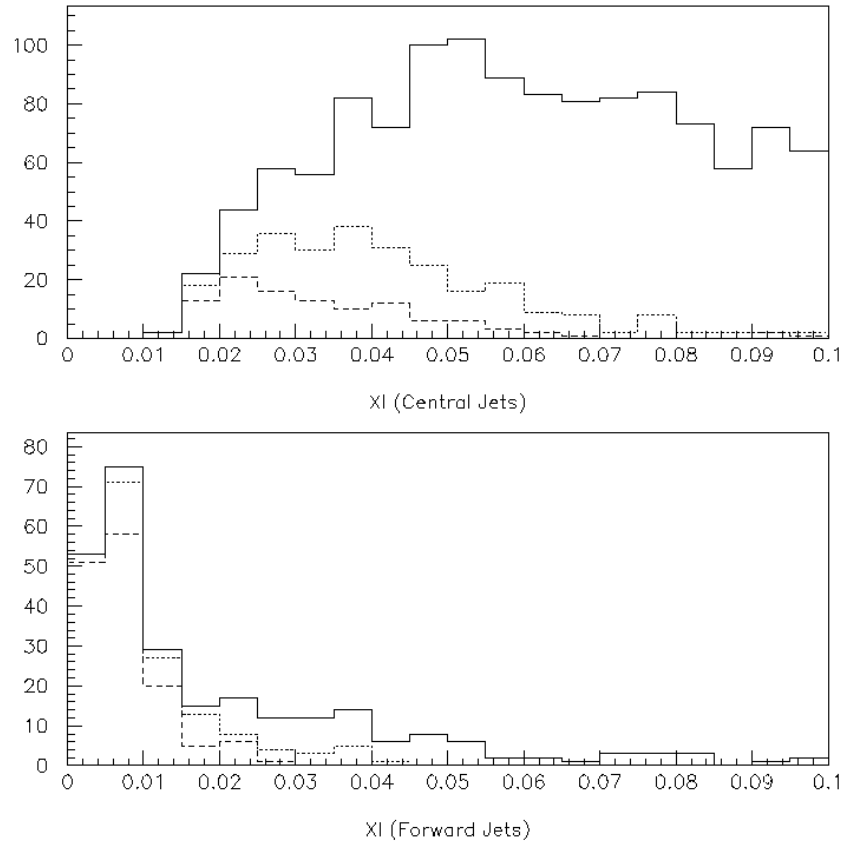


Figure 4.9 The effect of requiring a gap in the ξ distribution for forward and central jets with the hard gluon structure function at 1800 GeV. The long gap (dashed) restricts more of the higher mass events than the far gap (dotted).

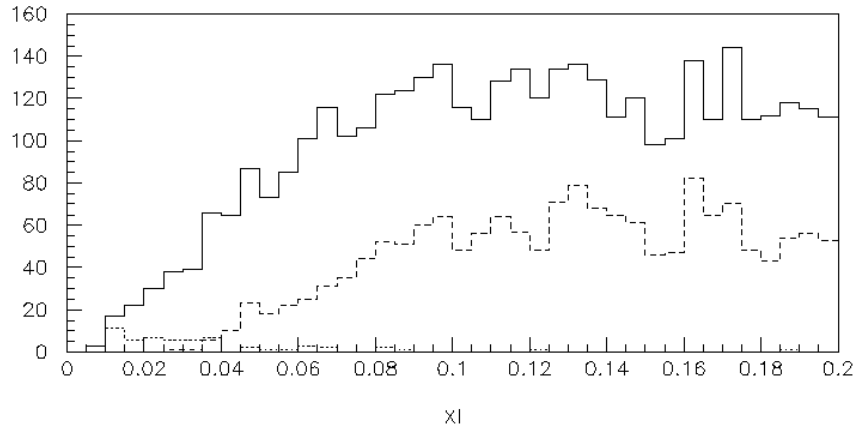


Figure 4.10 The ξ distribution for the hard gluon structure at 630 GeV for all events. The dashed line is the ξ distribution if we require central jets and the dotted line for forward jets. The ξ region probed for the central jets is higher than for the forward jets, and overall higher than at 1800.

In his paper, “Light-cone Variables, Rapidity and All That” [32], John Collins describes a method to measure the ξ distribution:

$$\xi \approx \Sigma \frac{E_{T_i} e^{y_i}}{2E}, \quad (4.1)$$

summing over the particles with the highest y and largest E_T . The outgoing diffracted proton (or the rapidity gap) is defined to be at positive η . This formula measures of the size of the rapidity gap. The particles that are of most significance are those that are closest to the rapidity gap. Those particles that are far away from the rapidity gap contribute very little to ξ . We first tested the formula’s validity at particle level.

Figure 4.12 shows a plot of the calculated ξ compared to the true ξ given by POMPYT for that event. The error shown is the RMS value from the corresponding two-dimensional scatter plot. At the particle level all information is present, so we sum over the E_T and η for every particle with an $|\eta| < 5.2$, the viewable region in the detector. Shown is a hard gluon structure at 1800 GeV, and a line fitted to the distribution has a slope of 1.0 ± 0.1 , consistent with $\xi_{\text{calc}} = \xi_{\text{true}}$. Applying the same procedure for the quark structure and even an extreme soft gluon structure at 1800 GeV and the hard gluon structure at 630 GeV give similar results. This formula does not depend on the structure function of the pomeron or the center-of-mass energy.

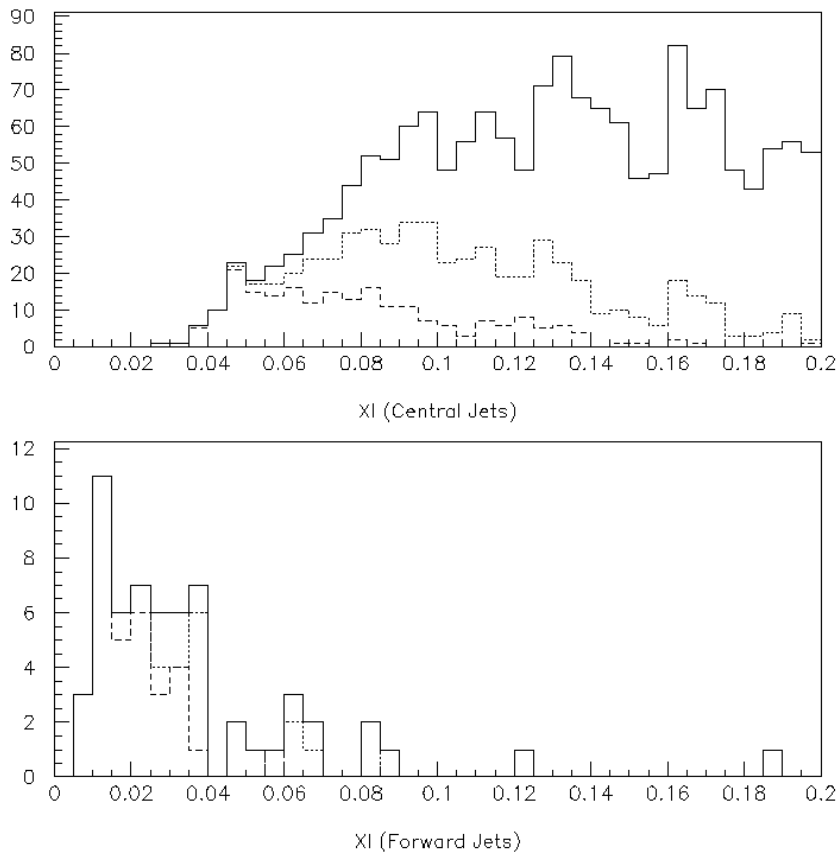


Figure 4.11 The effect of requiring a gap in the ξ distribution for forward and central jets with the hard gluon structure function at 630 GeV. The long gap (dashed) restricts more of the higher mass events than the far gap (dotted).

In data, or after full detector simulation, there is a more limited amount of information present. That we have towers instead of particles should not make any difference because we will be summing over all of the towers and it does not matter in the formula if we divide the energy of a particle into six towers or two. The limiting factor is the amount of information available in the data ntuples. The ntuple has the most information in the EM central calorimeter, which is also the most important. The energy for every central tower above 200 MeV is kept. The EM forward calorimeter has the energy in terms of whether the energy reached one of fourteen thresholds, from 0 MeV to 1.0 GeV. The minimum value of the threshold energy is assumed. The Hadronic calorimeter has only has five thresholds with limited information and since it is also far noisier, we decided to only use the EM calorimeter information.

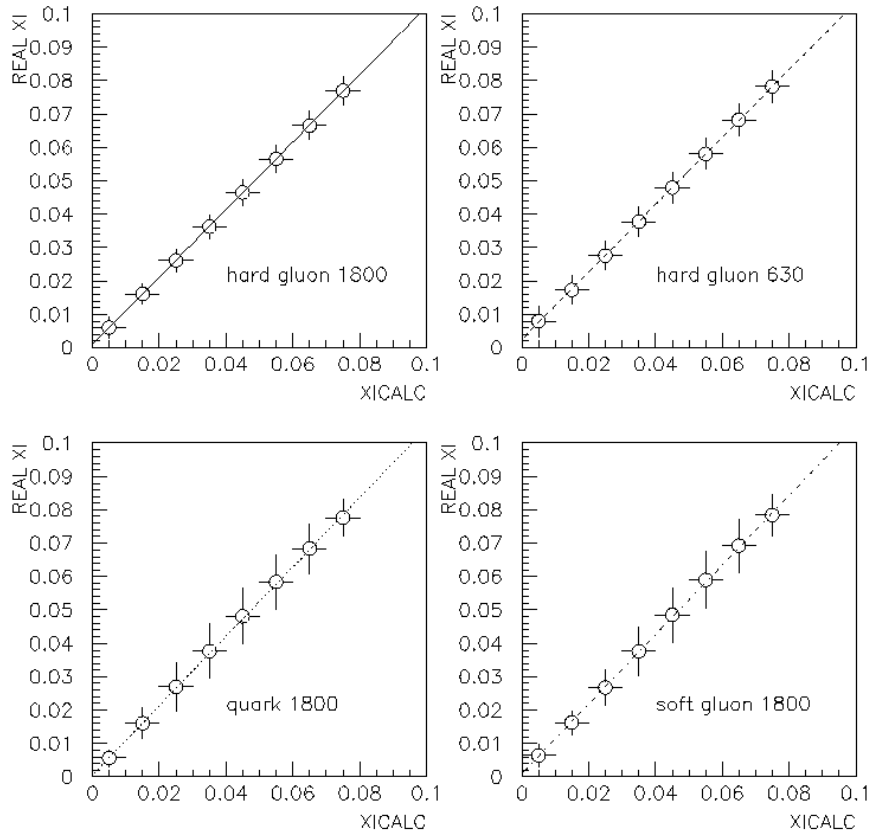


Figure 4.12 The relation between the true ξ and the ξ calculated using Collin's formula at particle level for the hard gluon at 1800 and 630 GeV and for the quark and soft gluon structure function. The slope of one does not depend on center-of-mass or structure function.

Figure 4.13 shows a plot of ξ_{calc} versus ξ_{true} after full detector simulation, where the error is the RMS value from a two-dimensional scatter plot. Because only the EM calorimeter is used in the calculation, about half of the energy is missing—resulting in a slope of about 2.2 ± 0.1 for every structure function and center-of-mass energy. As a double check, if we raise the EM threshold to 400 MeV, reducing further the energy that we include, the slope continues to increase. In order to apply this correction to the calculated ξ found in the data, the distribution needs to be corrected for the lost energy. Adding the additional error for the energy scale difference between Monte Carlo and data gives the final error and correction to be 2.2 ± 0.3 (see [33] for discussion of this error and unsmearing).

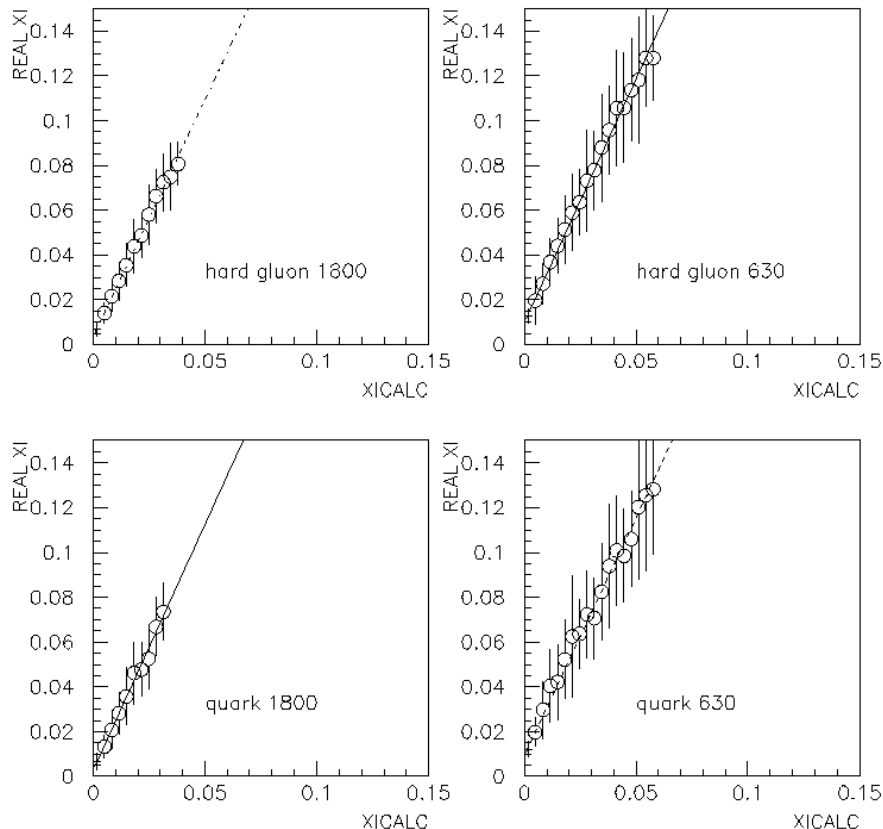


Figure 4.13 At the calorimeter level, the relation between true ξ and the ξ calculated. Shown is the hard gluon and quark structure function at both center of mass energies. The slope is the same within errors in all cases, but it is higher than one because we are only collecting about half of the energy using only the EM calorimeter.

Event characteristics

We have already noted one difference between POMPYT and PYTHIA events –the η distribution due to the boosted POMPYT events, but there are other similarities and differences in Monte Carlo that should be addressed. Plotted in Figure 4.14 is the jets multiplicity, the jet width, the $\Delta\phi$ between jets, and the jet E_T for POMPYT hard gluons (with a far gap) and PYTHIA (at 1800 GeV). The POMPYT events (solid) tend to have fewer jets than PYTHIA (dashed), and they are also thinner and more back to back (steeper $\delta\phi$). This is consistent with less overall radiation in the POMPYT events as expected from diffractive events. Figure 4.15 shows the same distributions at 630 GeV. It has similar characteristics although not as dramatic as the 1800 GeV sample.

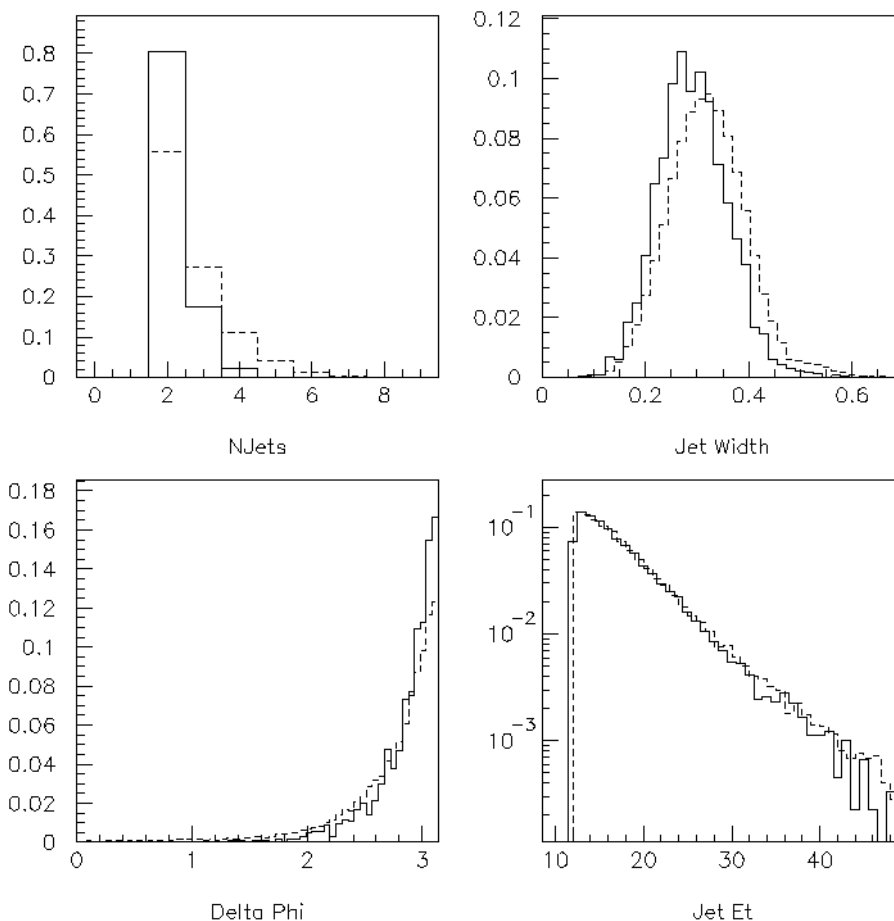


Figure 4.14 The number of jets, jet width, delta phi between jets, and jet E_T for the two leading jets in POMPYT hard gluon (solid) and PYTHIA (dashed) at 1800 GeV. The POMPYT events are quieter and thinner, consistent with less radiation in the event.

As shown in the Figures, the jet E_T for the two leading jets is consistent between the diffractive events and the non-diffractive events along the entire region. These distributions in POMPYT are for a $\xi < 0.1$ at 1800 GeV and $\xi < 0.2$ at 630 GeV. If we restrict the momentum given to the pomeron, as in Figure 4.16 to $\xi < 0.1$ at 630 GeV, then the POMPYT jet E_T falls away from the PYTHIA distribution at the higher jet E_T . So to match PYTHIA at 630 GeV, the POMPYT ξ distribution needs to extend to at least 0.2.

The event characteristics for flat gluons with a far gap is shown in Figure 4.17 and Figure 4.18 for 1800 and 630 GeV. The event characteristics for the flat gluon are similar to the hard gluon. Figure 4.19 and Figure 4.20 show the event characteristics of the POMPYT quark structure function at 1800 and

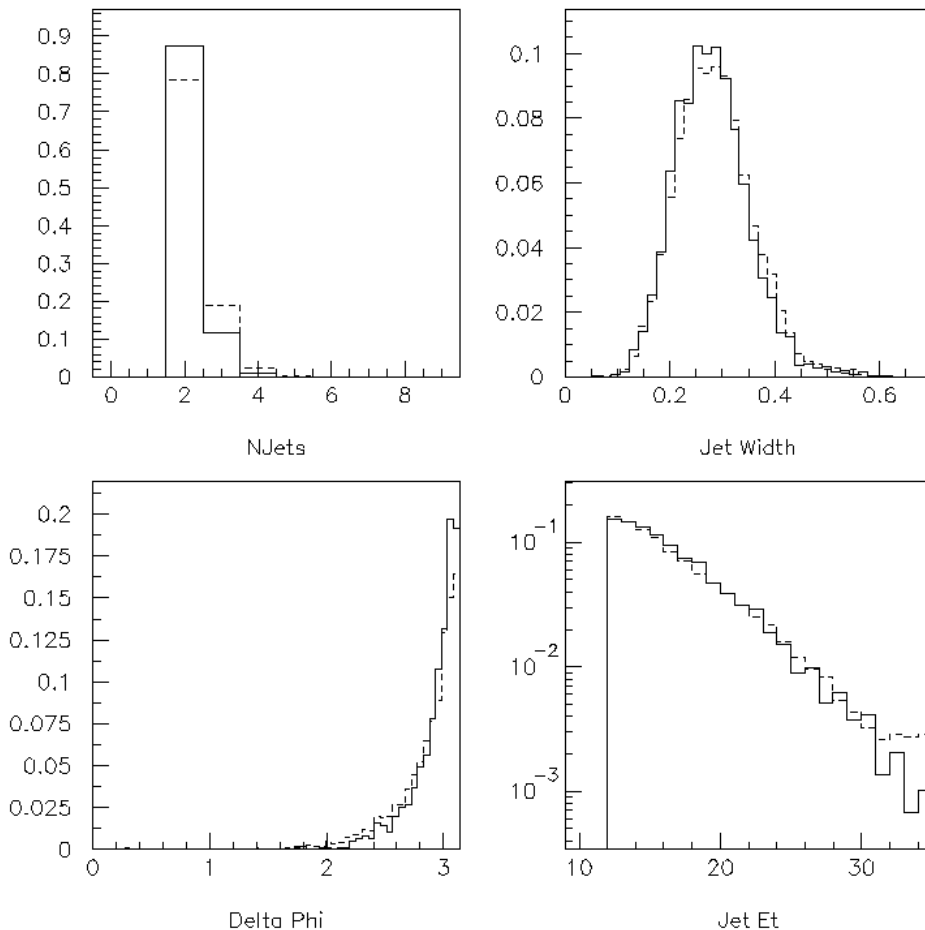


Figure 4.15 The number of jets, jet width, delta phi between jets, and jet E_T for the two leading jets in POMPYT hard gluon (solid) and PYTHIA (dashed) at 630 GeV.

630 GeV for events with a far gap. We compare the event characteristics for the soft gluon structure function with PYTHIA at 1800 (see Figure 4.21) and 630 (see Figure 4.22). Unlike the harder structures, the E_T distribution does not match PYTHIA at either center-of-mass energy with a $\xi < 0.1$ at 1800 GeV and a $\xi < 0.2$ at 630 GeV.

Diffraction rates

Our diffractive rate measurement is the fraction of that diffractive jet events in an inclusive jet sample, or the fraction of diffractive dijets to all dijets. In Monte Carlo this is the same as the cross-section measured in POMPYT26 divided by the cross-section measured by PYTHIA. At the particle

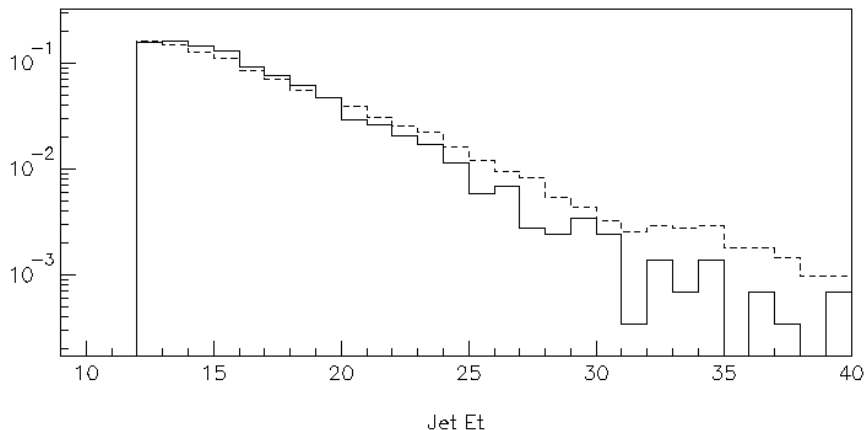


Figure 4.16 The jet E_T distribution at 630 GeV for two leading jets restricting the ξ in POMPYT to less than 0.1. POMPYT (solid curve) falls below PYTHIA (dashed curve) throughout much of the distribution.

level, where generation is fast, we can examine how it changes with different choices of initial variables. Then we can also look at the rate predictions with detector simulation which will provide a more accurate prediction. At particle-level we use the d0pjet algorithm to find the jets, which simulates jet-finding with data. There is no real difference in rates, number of jets, or other variables between d0pjet and LUCCELL, the internal PYTHIA jet-finding cone algorithm.

Before looking at the rates, we must first look at the overall multiplicity of the events. If there is a large underlying event, then making jets is easier and if there is no underlying event, making jets is harder. There are two components to the underlying event. There is the interactions of the spectator partons in the proton with the spectator partons in the pomeron. These, following the DØ standard language, we will call spectator interactions. (PYTHIA calls them multiple interactions.) There also can be multiple hard interactions between another proton and antiproton in the same beam-crossing. All of our data-sets are at low luminosity and selected for single interaction, because another interaction on top of the diffractive interaction can ruin the rapidity gap. So multiple $p\bar{p}$ interactions will not affect the rates, but the spectator interactions can.

The default version of POMPYT contained a bug producing far too many spectator interactions and many more jets, because the wrong underlying event distributions were used. We have corrected the bug, although with a diffractive event there is no reason to assume that there are any spectator interactions with pomeron exchange. Although there is little difference in the rates with turning them

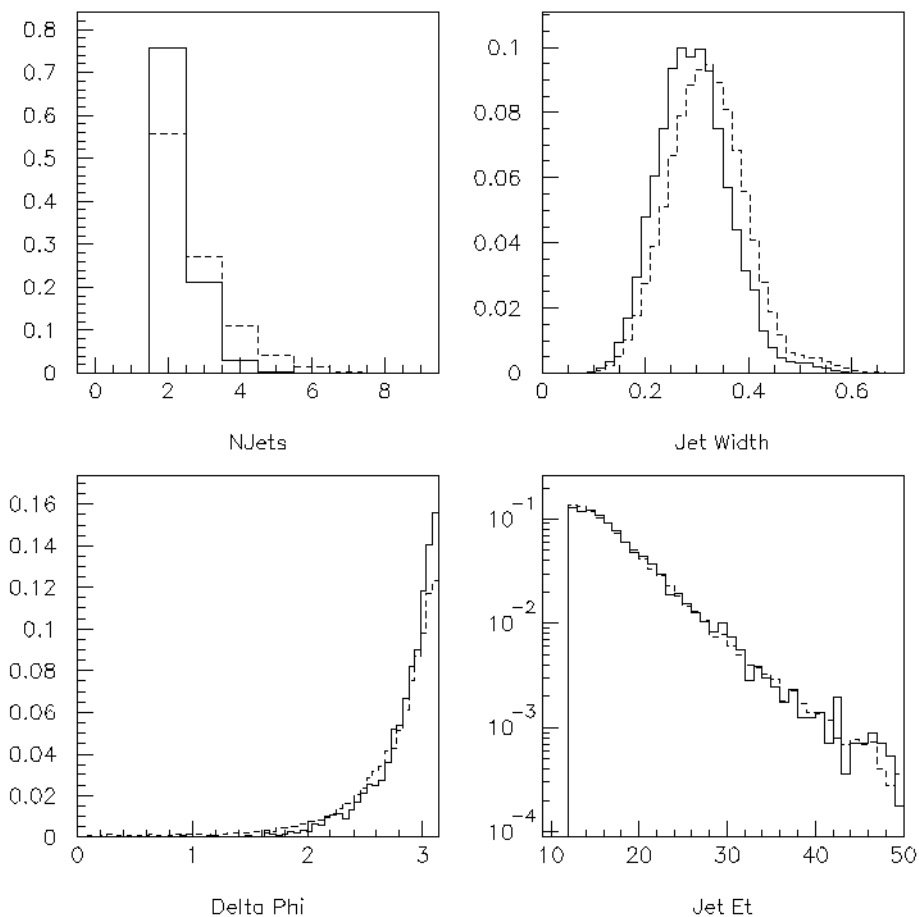


Figure 4.17 The number of jets, jet width, delta phi between jets, and jet E_T for the two leading jets in POMPYT flat gluon (solid) and PYTHIA (dashed) at 1800 GeV.

on or off, we have them turned off in POMPYT because the overall event multiplicities were slightly high when comparing to data in regions without a gap. We required central jets and a gap on only one side. Then we compared multiplicities on the opposite side. The multiplicities were not very different: a mean of 82 towers with underlying event and 76 towers without (far gap) comparing to a mean of 71 in data at 1800 GeV. Conversely, the PYTHIA underlying event multiplicities were a little low using the same method but requiring no gap. The mean multiplicity in data is 164 towers and the mean multiplicity in PYTHIA is 145 towers. To bring the average multiplicity closer to the data, we added a little more underlying event (the mean number of towers is with a small amount of added underlying event is 155). The parameters tuned in PYTHIA are $\text{PARP}(82)=2.25$ at 1800 GeV and $\text{PARP}(82)=2.20$ at 630 GeV. The $\text{PARP}(82)$ parameter is the low-end cut-off for calculating the cross-section and it is

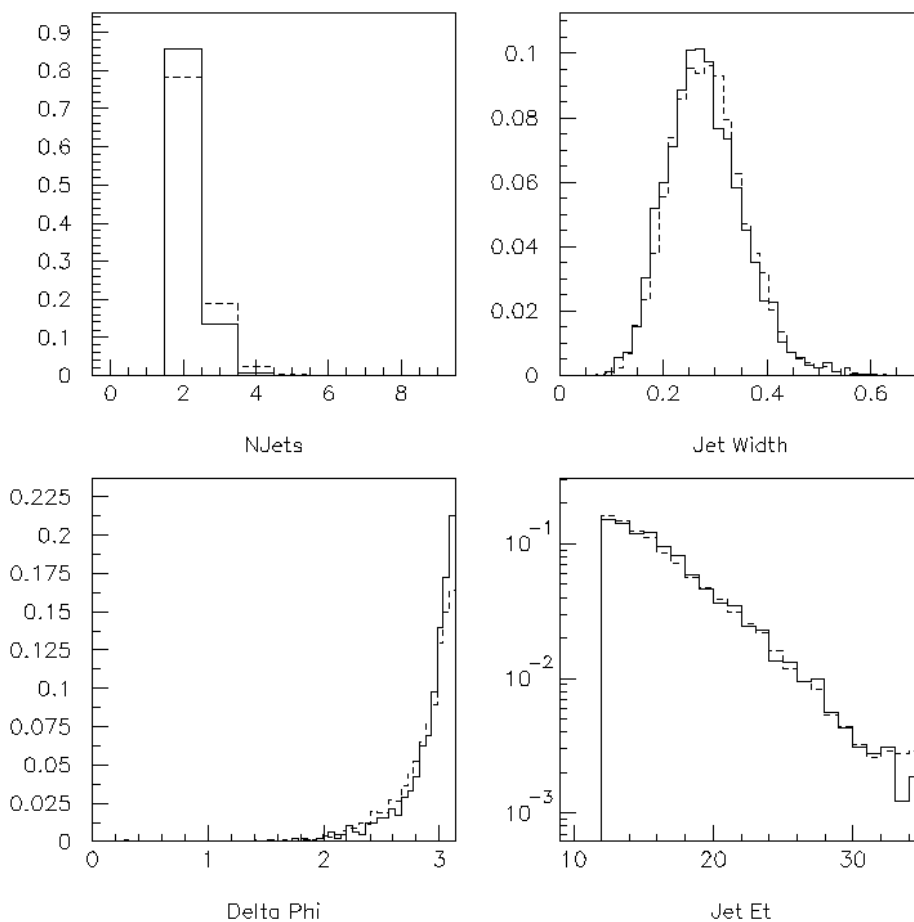


Figure 4.18 The number of jets, jet width, delta phi between jets, and jet E_T for the two leading jets in POMPYT flat gluon (solid) and PYTHIA (dashed) at 630 GeV.

customary to tune. The lower it is, the more underlying event that is added. Tuning PYTHIA and choosing no spectator interactions in POMPYT actually had very little effect on the rates with the POMPYT bug fixed.

Table 4.3 shows the rates at particle level for several different choices of input variables. (These rates do not include gap efficiency.) They are multiplied by a factor of two to compensate for only the antiproton being allowed to diffract in the POMPYT Monte Carlo. The central jet rates, as expected, are highly dependent on the input ξ upper bound. They also increase slightly when POMPYT underlying event is added. The next input parameters (epsilon, alpha, and dft2) are variations on the calculation of the flux –or how often a proton ‘emits’ a pomeron. The pomeron flux model by Donnachie and Landshoff [8] is given by

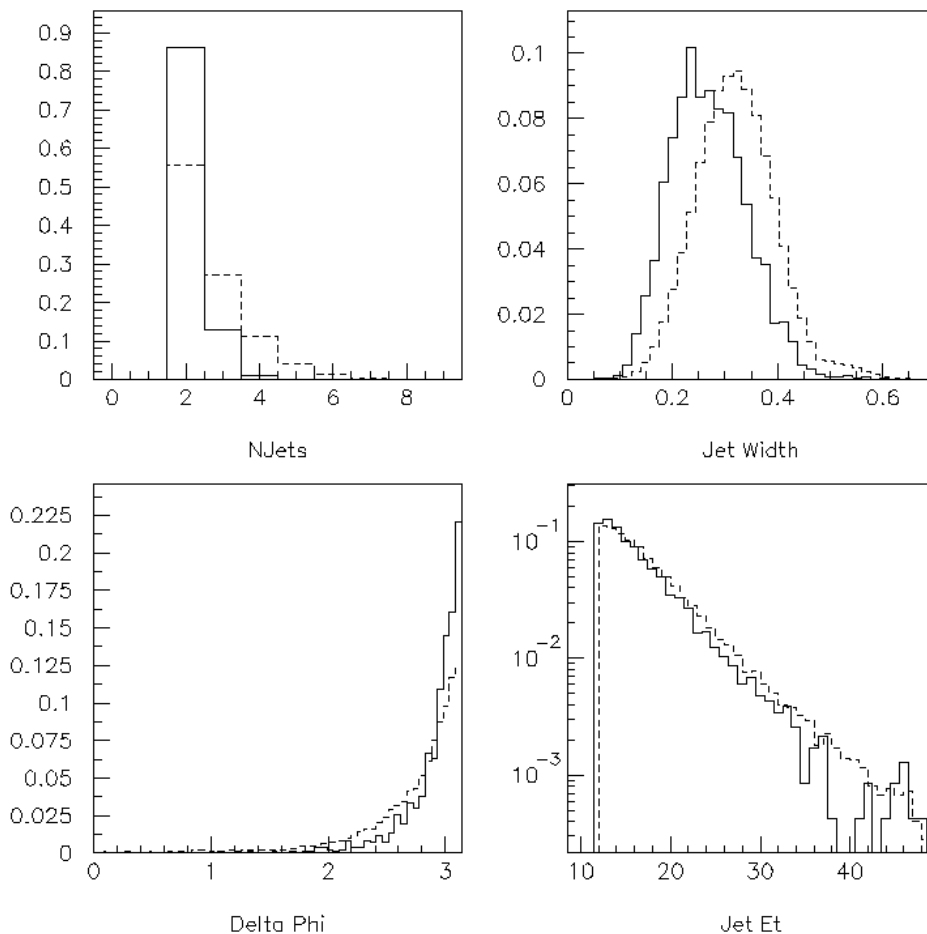


Figure 4.19 The number of jets, jet width, delta phi between jets, and jet E_T for the two leading jets in the POMPYT quark structure function (solid) and PYTHIA (dashed) at 1800 GeV.

$$f_{P/p}(x_P, t) = \frac{9\beta^2}{4\pi^2} [F_1(t)]^2 \left(\frac{1}{x_P}\right)^{2\alpha(t)-1} \quad (4.2)$$

where $\beta = 3.24 \text{ GeV}^{-2}$ is the effective pomeron-quark coupling. The standard pomeron Regge trajectory is given by

$$\alpha(t) = 1 + \epsilon + \alpha' t \quad (4.3)$$

where $\epsilon \simeq 0.085$ and the slope $\alpha' = 0.025$ are obtained by fits to world data. Variations shown in the table are based on fits to data made by the CDF collaboration [34]. They also use instead of the proton form factor $F_1(t)$ a falling exponential $e^{-4.6t}$ which is the variation FT2. Other than the ξ of

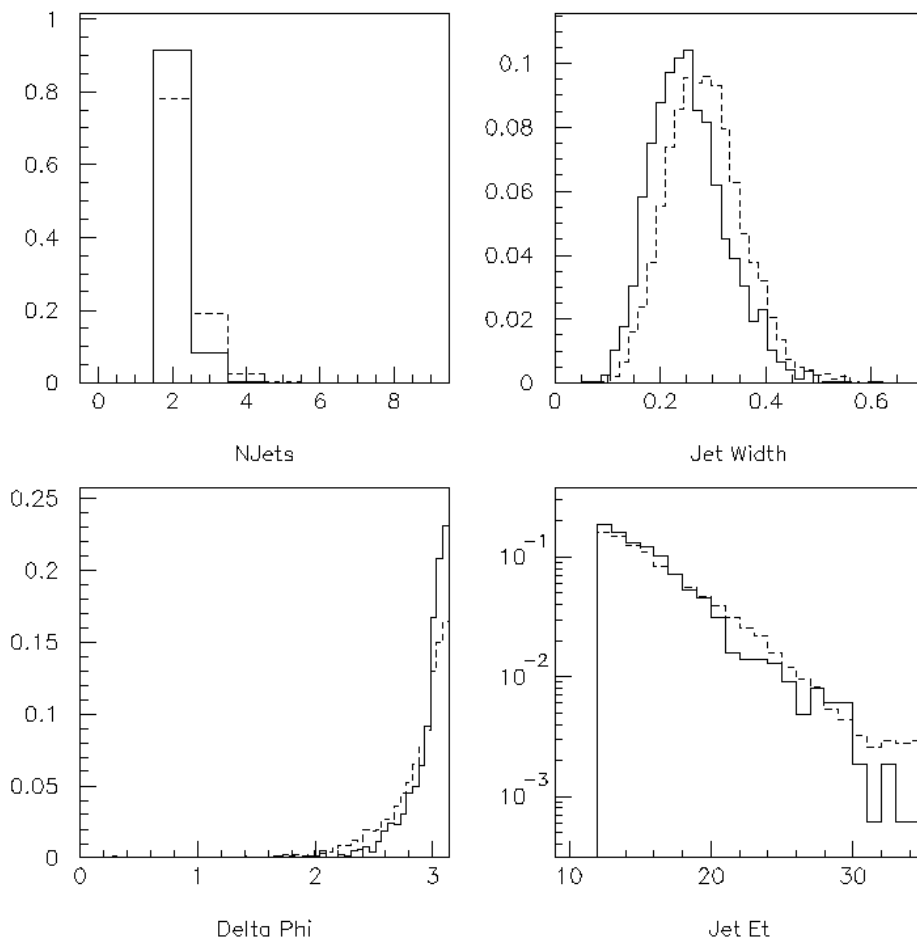


Figure 4.20 The number of jets, jet width, delta phi between jets, and jet E_T for the two leading jets in the POMPYT quark structure function (solid) and PYTHIA (dashed) at 630 GeV.

the pomeron, the variation in input parameters do not change the predictions by a significant amount. The central jet rate for hard gluons is expected to be around three times higher than the forward jet rate for a $\xi_{max} = 0.1$ and about one and a half times higher for a $\xi_{max} = 0.05$ Table 4.4 shows the rate predictions for the hard gluon, quark, flat gluon, and soft gluon at 1800 GeV ($\xi < 0.1$) and 630 GeV ($\xi < 0.2$).

That the central jet rate is higher than the forward jet rate seems counter-intuitive. Figure 4.23 shows the jet η and η_{boost} distribution at $\xi < 0.10$ and $\xi < 0.05$ ($\eta_{boost} = |(jet\eta_1 + jet\eta_2)/2|$) for the hard gluon structure function. The POMPYT $\xi < 0.10$ distribution is only slightly boosted away from zero and the lower ξ distribution is boosted farther as expected. A low momentum pomeron colliding

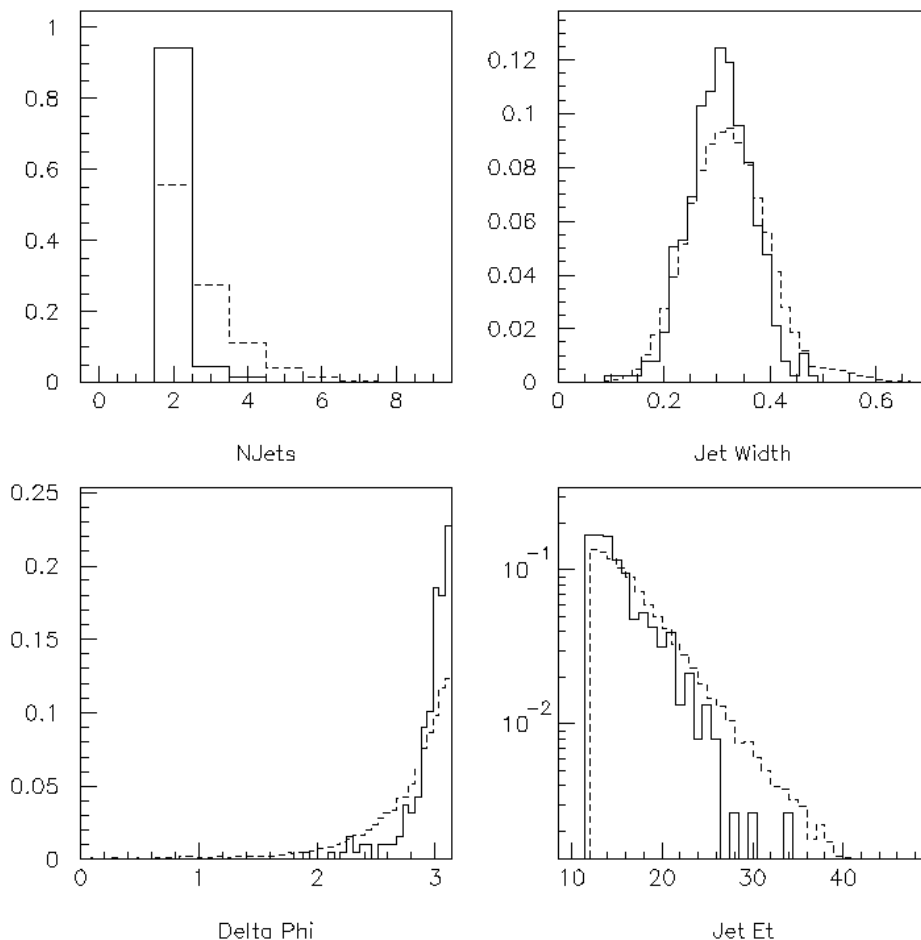


Figure 4.21 Event characteristics for the soft gluon structure function (solid) at 1800 GeV compared to PYTHIA (dotted).

against the proton will have a larger boost. Superimposed on the POMPYT η_{boost} distributions is the corresponding PYTHIA distribution. If we divide the POMPYT η_{boost} by the PYTHIA η_{boost} distribution and scale it by the cross-sections, we can plot the fraction versus η_{boost} at generator-level.

For a low momentum pomeron, the gap fraction rises with η_{boost} due to kinematics. The central boosted jets for a low momentum pomeron has a large PYTHIA background which decreases at larger boosts. At the same time, the POMPYT signal increases from the central boost to a more forward boost. If we make a cut requiring only both jets central or both jets forward, we are selecting only certain events out of those samples. In PYTHIA Figure 4.24 when we look at an η_{boost} less than one we have a large number of events where neither jet is central. Requiring central jets in PYTHIA cuts out a large number of events. However, since POMPYT is boosted and has no jets with an η greater than 2.0,

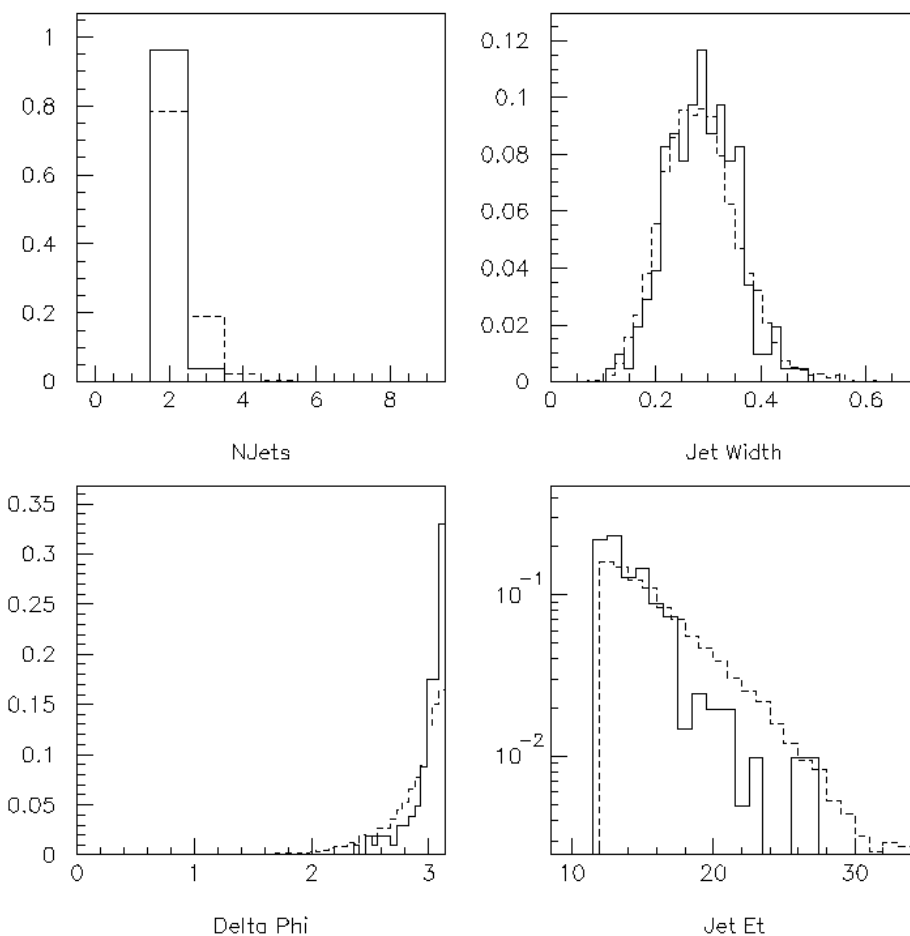


Figure 4.22 Event characteristics for the soft gluon structure function (solid) at 630 GeV compared to PYTHIA (dotted).

requiring central jets cuts a far smaller amount out of the sample than with PYTHIA. For forward jets POMPYT and PYTHIA are both at the edge of the jet distribution, and they lose a similar fraction of their events when we require both jets forward. So overall, even though the fraction vs. boost increases, the fraction can decrease (and does) when going from central to forward jets.

Table 4.5 shows the predicted rates after detector simulation. With full detector simulation the effect of jet η and E_T smearing as well as other detector can be taken into account to produce a better comparison to data. Except for the soft gluon, the central jet rate is higher than the forward jet rate, and the rate at 630 GeV are slightly higher than those at 1800 GeV.

Table 4.3 The predicted rates of 1800 POMPYT divided by PYTHIA at generator level for a hard gluon structure function and different choices of input values. The errors shown are binomial.

INPUT VARIATION	FORWARD JET RATE	CENTRAL JET RATE
1800 HARD GLUON ($\xi < 0.10$)	$3.4\% \pm 0.1\%$	$8.6\% \pm 0.2\%$
1800 HG UND ($\xi < 0.10$)	$3.6\% \pm 0.2\%$	$9.5\% \pm 0.2\%$
1800 HG EPSILON ($\xi < 0.10$)	$4.6\% \pm 0.2\%$	$10.2\% \pm 0.2\%$
1800 HG ALPHAP ($\xi < 0.10$)	$3.4\% \pm 0.1\%$	$8.4\% \pm 0.2\%$
1800 HG FT2 ($\xi < 0.10$)	$3.1\% \pm 0.1\%$	$7.8\% \pm 0.2\%$
1800 HG E,A,F ($\xi < 0.10$)	$4.2\% \pm 0.2\%$	$9.3\% \pm 0.2\%$
1800 HG ($\xi < 0.05$)	$3.1\% \pm 0.1\%$	$3.6\% \pm 0.1\%$

Table 4.4 The predicted rates of POMPYT divided by PYTHIA at generator level for several structure functions at 1800 and 630 GeV. The errors on the fraction are statistical. All have a central jet rate higher than forward jets except for the soft gluon.

STRUCTURE FUNCTION	FORWARD JET RATE	CENTRAL JET RATE
1800 HARD GLUON ($\xi < 0.10$)	$3.4\% \pm 0.1\%$	$8.6\% \pm 0.2\%$
1800 HG UND ($\xi < 0.10$)	$3.6\% \pm 0.2\%$	$9.5\% \pm 0.2\%$
630 HARD GLUON ($\xi < 0.20$)	$5.7\% \pm 1.1\%$	$12.4\% \pm 0.5\%$
630 HG UND ($\xi < 0.20$)	$6.0\% \pm 1.1\%$	$13.7\% \pm 0.5\%$
1800 QUARK ($\xi < 0.10$)	$1.7\% \pm 0.1\%$	$4.1\% \pm 0.1\%$
1800 QUARK UND ($\xi < 0.10$)	$1.7\% \pm 0.1\%$	$4.4\% \pm 0.1\%$
630 QUARK ($\xi < 0.20$)	$3.4\% \pm 0.8\%$	$6.3\% \pm 0.3\%$
1800 FLAT GLUON ($\xi < 0.10$)	$4.0\% \pm 0.2\%$	$7.5\% \pm 0.2\%$
1800 FG UND ($\xi < 0.10$)	$4.2\% \pm 0.2\%$	$8.1\% \pm 0.2\%$
630 FLAT GLUON ($\xi < 0.20$)	$6.1\% \pm 1.1\%$	$11.4\% \pm 0.5\%$
1800 SOFT GLUON ($\xi < 0.10$)	$8.8\% \pm 0.2\%$	$3.1\% \pm 0.1\%$
1800 SG UND ($\xi < 0.10$)	$14.3\% \pm 0.3\%$	$6.2\% \pm 0.2\%$
630 SOFT GLUON ($\xi < 0.20$)	$13.0\% \pm 1.5\%$	$2.9\% \pm 0.2\%$

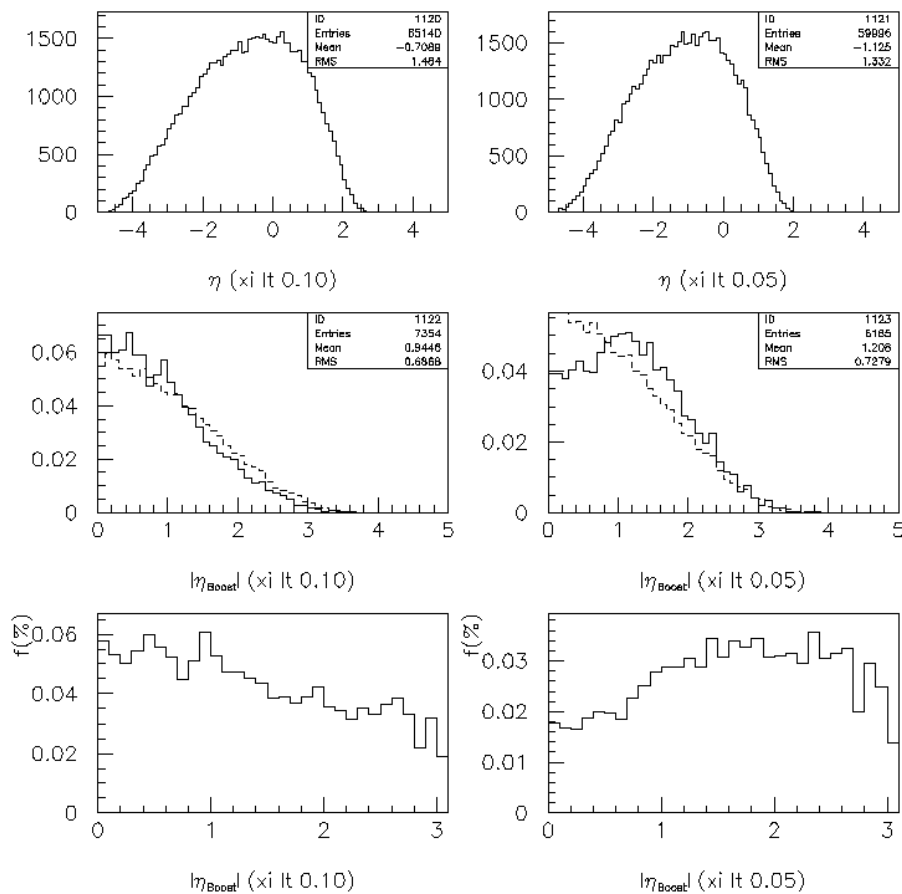


Figure 4.23 The jet η and η_{boost} distribution for POMPYT hard gluon $\xi < 0.10$ and $\xi < 0.05$. The higher momentum pomeron is only slightly boosted where the lower momentum pomeron distribution shows a definite boost. Overlaid on the η_{boost} distributions is a PYTHIA sample that is symmetric about zero. The last plots show the fraction versus η_{boost} for each distribution. The low ξ fraction increases with η_{boost} due the kinematics of the event.

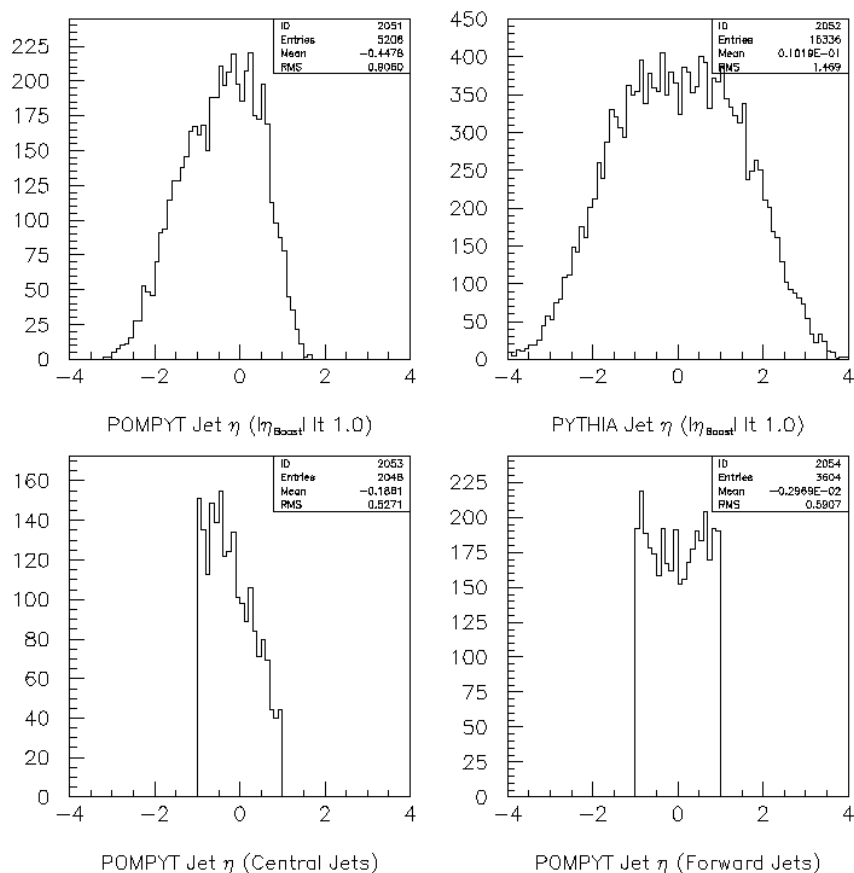


Figure 4.24 The distribution of jet η in POMPYT and PYTHIA if $\eta_{boost} < 1.0$, and the effect on each with cutting on two central jets. PYTHIA loses a significant portion of events with the cut compared to POMPYT.

Table 4.5 The predicted rates of POMPYT divided by PYTHIA after full detector simulation for several different structure function choices.

STRUCTURE FUNCTION	FORWARD JET RATE	CENTRAL JET RATE
1800 HARD GLUON ($\xi < 0.10$)	$2.8\% \pm 0.1\%$	$7.1\% \pm 0.1\%$
630 HARD GLUON ($\xi < 0.20$)	$5.4\% \pm 0.1\%$	$10.5\% \pm 0.1\%$
1800 FLAT GLUON ($\xi < 0.10$)	$3.6\% \pm 0.1\%$	$6.2\% \pm 0.1\%$
630 FLAT GLUON ($\xi < 0.20$)	$4.3\% \pm 0.1\%$	$10.1\% \pm 0.1\%$
1800 QUARK ($\xi < 0.10$)	$1.5\% \pm 0.1\%$	$2.6\% \pm 0.1\%$
630 QUARK ($\xi < 0.20$)	$4.2\% \pm 0.1\%$	$5.7\% \pm 0.1\%$
1800 SOFT GLUON ($\xi < 0.10$)	$6.8\% \pm 0.1\%$	$1.8\% \pm 0.1\%$
630 SOFT GLUON ($\xi < 0.20$)	$8.6\% \pm 0.1\%$	$1.8\% \pm 0.1\%$

Monte Carlo Interpretation

Monte Carlos based on the Ingelman-Schlein model were the only useful diffractive Monte Carlos available until recently. Too late to be included in this thesis is a first Monte Carlo based on the soft color interaction model. This model assumes no pomeron dependence and explains diffraction with a non-perturbative color-cancellation mechanism. The preliminary running at particle level is encouraging, although much still needs to be done, and the Monte Carlo is still changing. Meanwhile, POMPYT, which is based on the Ingelman-Schlein model is a powerful tool for comparison to data, and the data can either agree with the model's predictions, or reject the model.

5 DATA ANALYSIS

We use two different data samples to provide information on the number of jet events with forward rapidity gaps: ‘lowlum’ data at 1800 GeV and ‘lnr’ data at 630 GeV, which are both at a low luminosity. With these we can measure how the fraction of diffractive dijets to all dijets changes in the different rapidity ranges and if it compares to Monte Carlo expectations. We can also compare the 1800 GeV and 630 GeV data fractions.

There are two different triggers for each data set to study the forward and central jet samples. With the forward jet analysis, the data were obtained with a forward jet trigger (2 12 GeV jets with an $|\eta| > 1.6$). For the central jet analysis, the data were obtained with an inclusive jet trigger (2 15 GeV jets) and we imposed an off-line η cut ($|\eta| < 1.0$). The E_T threshold was higher for the inclusive jet trigger due to the online trigger thresholds used for these data.

Data selection

Events were selected with the following criteria:

- 2 forward jets with $E_T > 12$ GeV (V5.2 corrected) and $|\eta| > 1.6$
(jets are defined with a cone radius of 0.7)
- 2 central jets with $E_T > 15$ GeV (V5.2 corrected) and $|\eta| < 1.1$
(jets are defined with a cone radius of 0.7)
- Both leading jets passed standard quality cuts
 - $0.5 < \text{jet EM fraction} < 0.95$
 - $0.4 < \text{jet CH fraction}$
 - $10 > (\text{Hottest Cell})/(\text{Next-to-hottest Cell})$
- Only events with 1 vertex were allowed

- Total Missing ET < 25 GeV

These events were corrected with the jet energy scale (V5.2), but no underlying event was subtracted from the jets in the sample. This is because the underlying event for diffractive events is much less than that of non-diffractive events. This has very little effect in our measurement.

Table 5.1 shows the number of events passing each selection. The latter two cuts were found to be effective for rejecting cosmic ray events, which are a source of background in triggers requiring calorimeter activity while vetoing on the beam interaction tag (Level0).

One additional cut was applied to the inclusive sample:

- Multiple interaction (MI) flag < 2

This requirement is a loose veto on multiple interactions. An MIflag value of zero means that there was not sufficient Level0 information to calculate the flag (hits on both sides are required). The veto triggers thus have a value of 0. A value of 1 designates that the event likely contained a single interaction.

The effect of multiple interactions must be carefully considered in searching for a single diffraction signal using rapidity gaps. The presence of a second $p\bar{p}$ inelastic collision in an SD event will typically spoil any rapidity gap. And on average such secondary interactions will shift the particle multiplicities in events to higher values. Therefore we will pay particular attention to very low luminosity data where this effect is significantly reduced.

In all of the samples, the hot cells are removed. The threshold for hot cells in this analysis is different than in most others, because “warm” cells with an energy of 200 MeV can affect the measured gap fraction. Since there are few runs, especially in the special low luminosity 1800 sample, we find these hot cells by simply plotting η vs. ϕ for every tower with an energy greater than threshold. Any hot cell in this distribution clearly shows as a spike because it is always turned on, and it is removed.

Table 5.1 Effect of cuts on number of events.

EVENT CUT	1800 FWD	1800 CENT	630 FWD	630 CENT
TRIGGER	95728	152975	107544	955166
2JETS, JET ET	88439	96458	63449	247787
JET QUALITY	82769	90074	56524	222951
VERTEX ,MIFLAG	61074	65279	33685	155770
CENTRAL VERTEX	56988	60064	30214	134051
MISSING ET	56981	60055	30214	134039
JET PLACEMENT(CEN)	56981	14008	30214	43575

Signal measurement

For the forward jets analysis, the number of forward calorimeter towers above threshold (n_{CAL}) and the number of L0 scintillator tiles hit is measured opposite the two leading jets. For the central jets analysis (which does not have a preferred side for a rapidity gap), the minimum number of calorimeter towers above threshold and the number of L0 scintillator tiles hit on the same side is measured. This is shown for the far gap in Figure 5.3 at 1800 GeV center of mass energy for the multiplicities over the entire sample as well as for a close-up of the lower multiplicity bins. Both distributions show a peak at zero in agreement with expectations for a diffractive signal component and a large broad mean multiplicity peak associated with non-diffractive events. The diffractive signal component is visible in both distributions, but for the central jets, the signal is a lower percentage of the total sample than for the forward jet sample. Figure 5.4 shows the same distributions at 630 GeV center of mass energy. They also show the same qualitative behavior, although the mean multiplicities are lower in general because fewer particles are produced at a lower center of mass energy.

Fitting

Signals above underlying multiplicity distributions in the hard diffractive analyses are extracted by application of a two dimensional fit to the calorimeter and level \emptyset multiplicities. Sample multiplicity distributions are shown in Figure 5.1. The upper two plots show a calorimeter versus L \emptyset multiplicity plot from the 1800 GeV single veto data set. In the bottom panels the projections onto the L \emptyset and calorimeter axes are shown. Earlier versions of the analyses fit only to the one dimension N_{CAL} distribution. A ‘leading edge’ fit was used to fit N_{CAL} in the region between the low multiplicity peak and the most probable value of the multiplicity distribution. The fit was then extrapolated to zero multiplicity and used as a background estimate for extraction of the diffractive signal. This proved unsatisfactory in some cases, because the extrapolation of the fit under the peak at zero multiplicity could show large variations based on the functional form selected. This motivated fitting the 2-D distributions. The 2-D distributions clearly contain more information, because they include information from two detectors. And the background distribution is nearly flat, making signal extraction significantly less dependent on the choice of functional form used to fit the background.

In the 2-D fits both signal and background are fit simultaneously. The background and signal are parameterized as

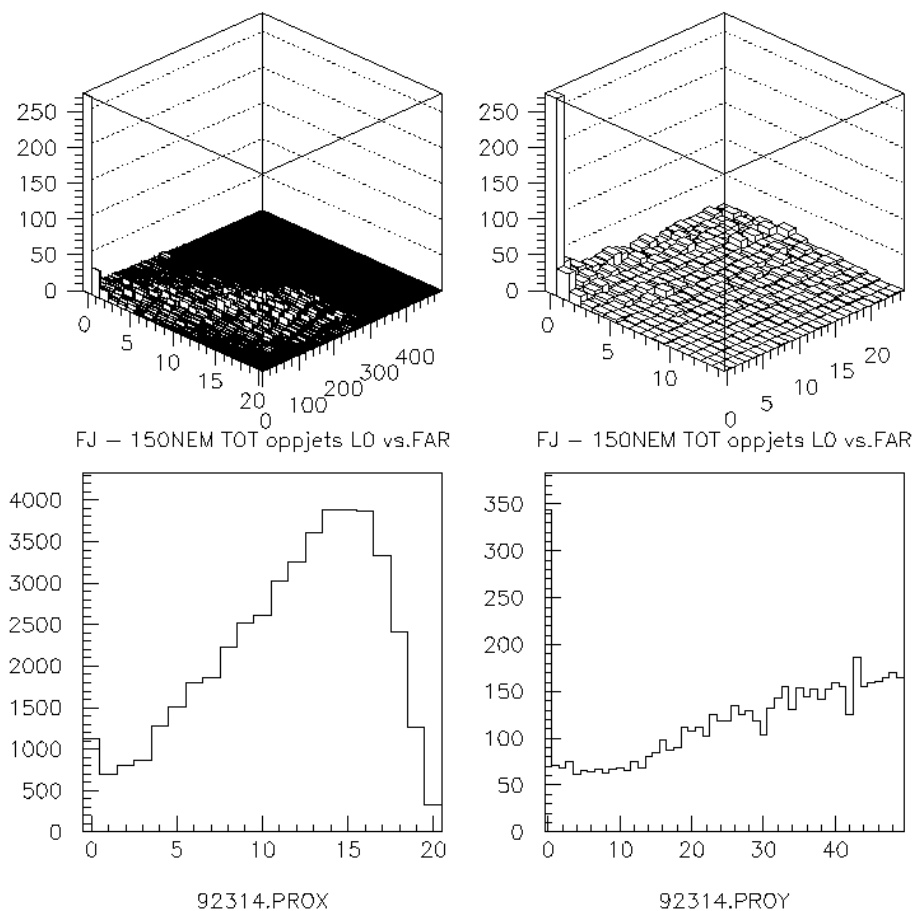


Figure 5.1 The multiplicity distributions for 1800 GeV forward jets, the entire multiplicity, the lower multiplicity bins, and the projections onto the L0 and calorimeter axes.

$$B = B_0 + B_1 \cdot \int_{x_i}^{x_f} x dx + B_2 \cdot \int_{y_i}^{y_f} y dy + B_3 \int_{x_i}^{x_f} \int_{y_i}^{y_f} xy dx dy$$

and

$$S = \frac{S_0}{S_1 \cdot S_2} \cdot \int_{x_i}^{x_f} \int_{y_i}^{y_f} \exp(-x/S_1 - y/S_2) dx dy$$

The B_i 's are background fit parameters and the S_i 's are signal fit parameters. The integrations are meant to illustrate that the function is integrated over each bin for comparison to the data. More complex background functions including high powers on 'x' and 'y' were explored. However, due to the relative flatness of the background distribution, they were not found to be necessary.

The fit proceeds in two steps. First a region around the signal peak is masked out (typically 2 bins in N_{L0} by 3 bins in N_{CAL}) and a background-only fit is applied to the background region. Then all

parameters in the fit are freed and a (signal + background) fit is performed. The parameters are found using a χ^2 minimization where χ^2 is calculated by setting the error in each bin to the square root of the number of fit events in the bin. This removes biases caused by using the data to estimate the error in each bin in cases of low background multiplicities.

It is necessary to determine the upper limits on the fit. In some sense we still apply a ‘leading edge’ fit, because we do not expect any useful background information to come from the very high multiplicity regions, far removed from the signal peak. Also fitting over large multiplicity ranges greatly complicates the shape of the background function and can cause large biases in the background extraction if the shape is being strongly constrained by data far from the signal. Since $L\bar{O}$ multiplicities are generally small we choose an $N_{L\bar{O}}$ range to include most of the region up to the peak in the 1-D $N_{L\bar{O}}$ distribution to maximize the information obtained from $L\bar{O}$. The N_{CAL} range is chosen by an iterative approach. Initially the calorimeter range is set to the peak of the 1-D N_{CAL} distribution and it is successively lowered until the χ^2 's of the fits are observed to reduce and reach a stable value.

The result of a fit to the data in Fig. 5.1 is shown in Fig. 5.2. The top plots show the data without and with the fit (ranges are set to show the fit region). The middle two plots show the background and signal fits. The bottom plots show the fit residuals in a 2-D plot and the fractional residuals in histogram form.

The signal is S_0 , the number of signal events in the sample. The fractional signal is then S_0 divided by the total number of events. The error on the signal is determined from a MINOS error analysis. In the event that MINOS errors are not available, the MINUIT parabolic error is used as an estimate of the signal error. The signal error (σ_{S_0}) reflects the uncertainty in the background fit as well as uncertainty in the signal normalization due to signal statistics.

When we are fortunate enough to have very high numbers of events in the data, though we may obtain a reasonable fit to the eye, it is sometimes difficult to obtain a fit where the χ^2 per degree of freedom is sufficiently probable to accept the fit errors estimates from MINUIT. In these cases we scale the individual bin errors up by $\sqrt{(\chi^2/\text{dof})}$, redo the fit, and obtain inflated fit errors to cover apparent uncertainties in our background model.

Table 5.2 shows the gap fractions obtained. In general, the 630 GeV gap fractions are higher than the 1800 GeV gap fractions, and forward jet gap fractions are higher than central jet gap fractions.

Table 5.3 and Table 5.4 show the measured gap fractions for the near gap and long gap at 1800 and 630 GeV. The near gap fraction is less than the far gap fraction because the rapidity gap region is moved closer to the hard scattering interaction where more rapidity gaps are ruined. The long gap region

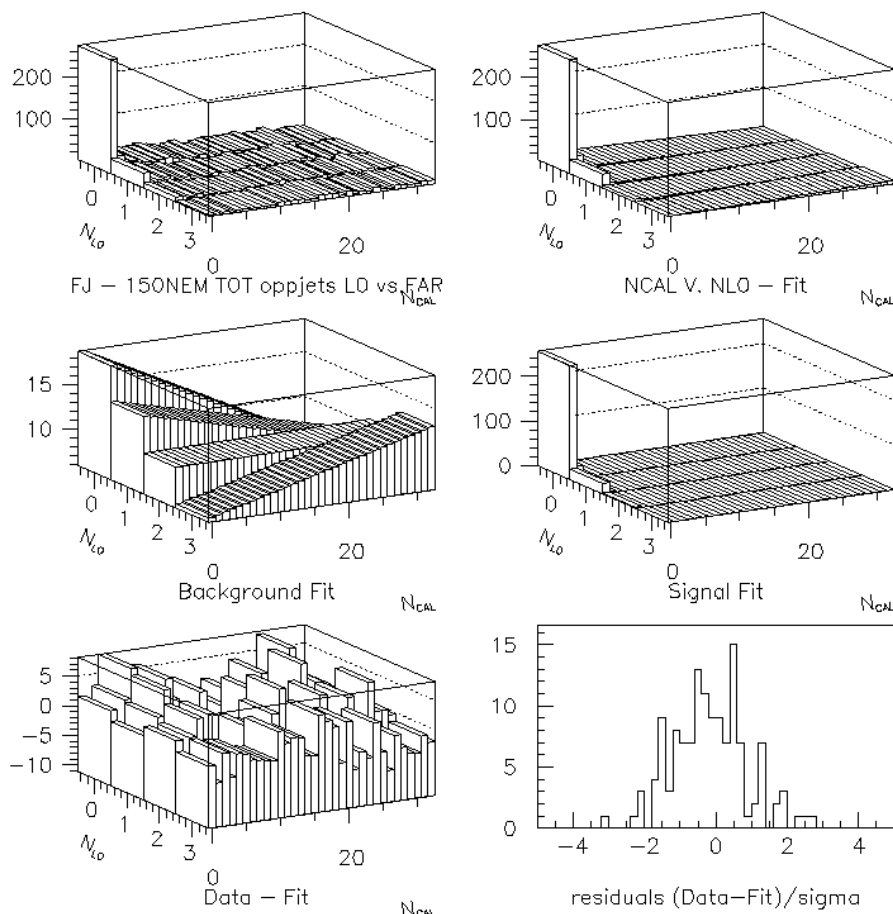


Figure 5.2 The fit results for 1800 GeV forward jets.

includes the near gap except it reaches farther out in pseudorapidity, including $4.1 < |\eta| \leq 5.2$. This is another unit of rapidity onto the far end towards where the outgoing proton or antiproton is leaving. The signal is slightly less than for the near rapidity gap definition correspondingly, because some of the time the outgoing proton will become excited and break apart. From theory calculations [35], double diffraction where the diffracted proton breaks happens around 10% of the time.

Now when we begin to move the rapidity gap farther from the two jets and keeping the farthest point the same, the fraction starts to increase. This meets qualitatively with expectations, because it is allowing for higher mass states. When the pomeron has a large momentum, a larger mass can be produced which can spread out and potentially ruin more rapidity gaps. By moving the rapidity gap out farther, less gaps are spoiled so our signal increases.

Table 5.2 Measured gap fractions for the far gap region for central and forward jets at both center-of-mass energies.

EVENT SAMPLE	FITTED FAR GAP FRACTION
1800 FORWARD JETS	$0.69\% + 0.05\% - 0.05\%$
1800 CENTRAL JETS	$0.23\% + 0.08\% - 0.05\%$
630 FORWARD JETS	$1.22\% + 0.10\% - 0.09\%$
630 CENTRAL JETS	$0.94\% + 0.07\% - 0.05\%$

Table 5.3 Measured gap fractions for the near gap region for central and forward jets at both center-of-mass energies.

EVENT SAMPLE	FITTED NEAR GAP FRACTION
1800 FORWARD JETS	$0.54\% + 0.06\% - 0.06\%$
1800 CENTRAL JETS	$0.07\% + 0.04\% - 0.03\%$
630 FORWARD JETS	$0.67\% + 0.09\% - 0.08\%$
630 CENTRAL JETS	$0.32\% + 0.10\% - 0.05\%$

Table 5.4 Measured gap fractions for the long gap region for central and forward jets at both center-of-mass energies.

EVENT SAMPLE	FITTED LONG GAP FRACTION
1800 FORWARD JETS	$0.45\% + 0.04\% - 0.04\%$
1800 CENTRAL JETS	$0.11\% + 0.05\% - 0.03\%$
630 FORWARD JETS	$0.60\% + 0.07\% - 0.07\%$
630 CENTRAL JETS	$0.25\% + 0.04\% - 0.04\%$

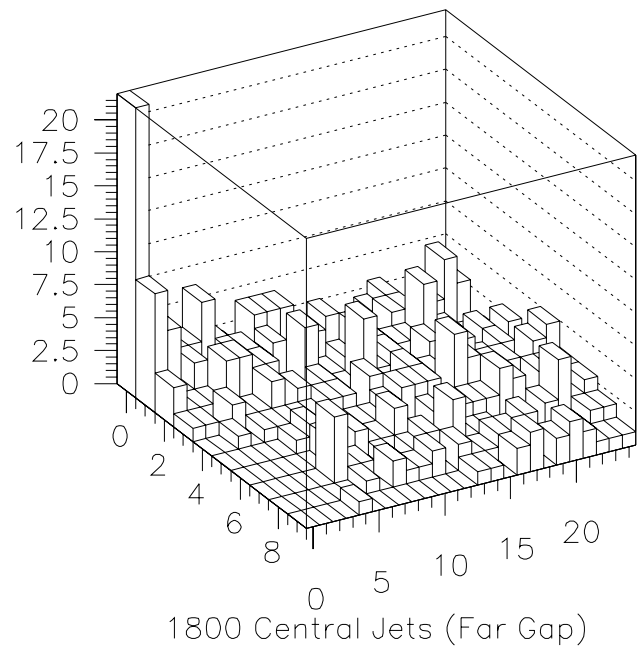
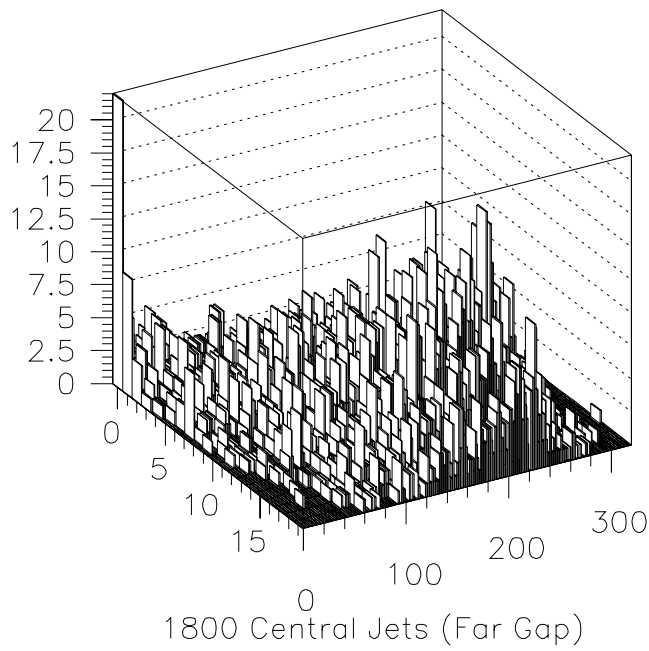
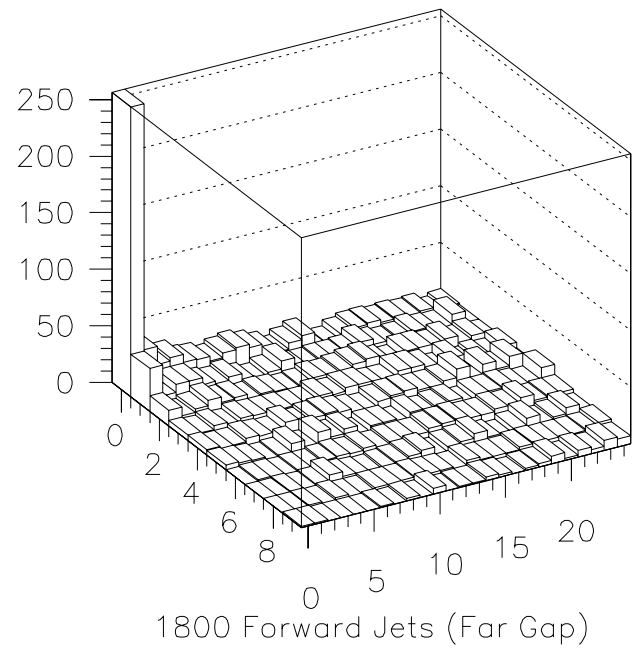
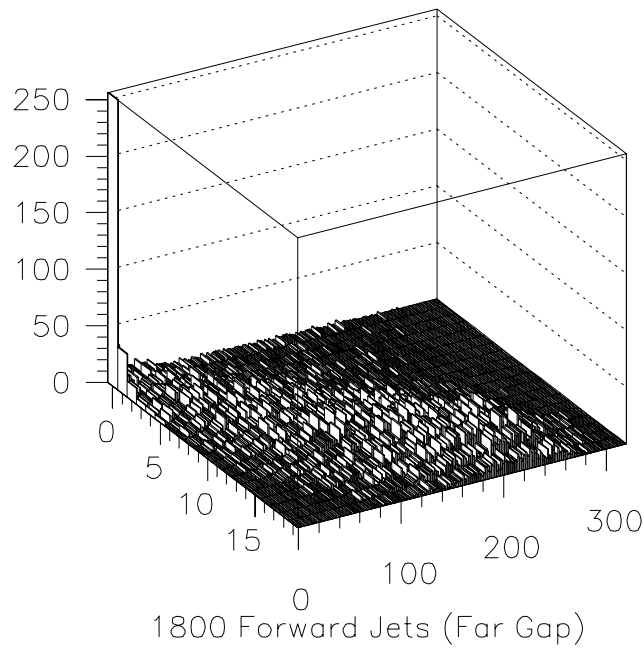


Figure 5.3 The 2D far gap multiplicity at 1800 GeV for forward and central jets. Shown is for all multiplicities (left) as well as a close-up of the lower multiplicity bins (right).

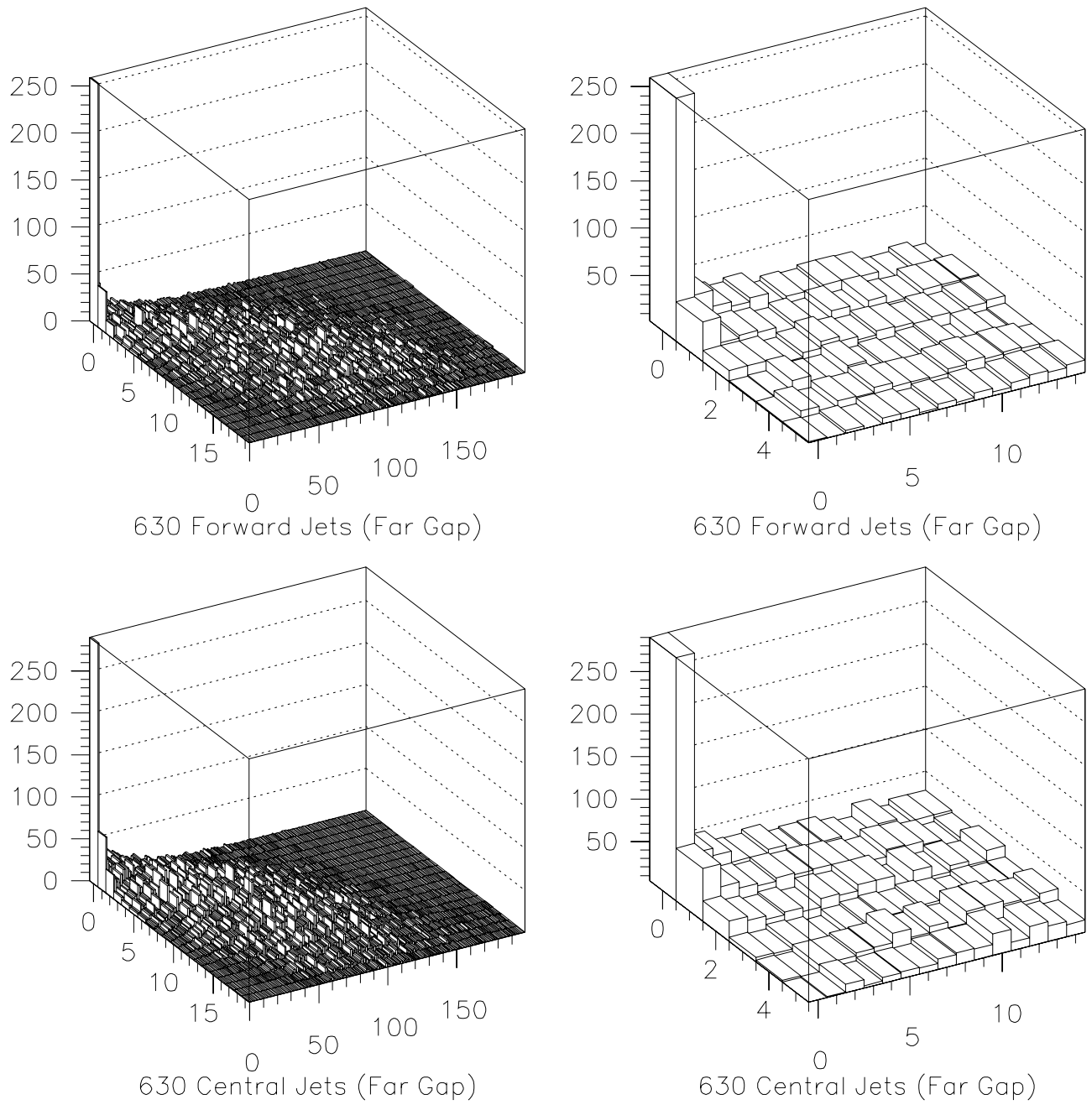


Figure 5.4 The 2D far gap multiplicity at 630 GeV for forward and central jets. Shown is for all multiplicities (left) as well as a close-up of the lower multiplicity bins (right).

Cross-checks and corrections

The errors given in the tables are the combined statistical and the systematic errors on the fit. There are potentially other systematic errors associated with dependence of the gap fraction on the initial cuts, the noise in the detector, as well as the thresholds chosen.

Table 5.5 shows the gap fraction for the forward jets at 1800 GeV as a function of initial data cuts. The fraction is quite stable with all variations. All ‘good’ jets specifies that every jet in the event meets the jet quality cuts, instead of only the first two, and no ‘good’ jets removes the quality cuts on the jets. E_T high and E_T low vary the energy scale of the jets, and lum1 and lum2 divide the luminosity of the already low luminosity sample into a high and low sample. This searches for any systematics that vary with luminosity, such as residual multiple interactions. Cutting on the number of vertices equal to one is another cut to eliminate residual multiple interactions. At 1800 GeV we have a very low luminosity sample with an average luminosity of 0.2×10^{30} , but at 630 GeV we have a slightly higher luminosity sample (0.7×10^{30}) that could allow in a few multiple interactions (see Figure 5.5).

Table 5.5 Fitted gap fractions for the far gap region for 1800 forward jets, varying the data cuts applied to the sample. The fraction is stable.

DATA CUT	1800 FWD JET FITTED GAP FRACTION
STANDARD	0.69% + 0.05% – 0.05%
ALL ‘GOOD’ JETS	0.69% + 0.05% – 0.05%
NO ‘GOOD’ JETS CUT	0.69% + 0.04% – 0.05%
E_T HIGH	0.69% + 0.04% – 0.06%
E_T LOW	0.66% + 0.04% – 0.05%
LUM 1	0.67% + 0.06% – 0.06%
LUM 2	0.70% + 0.07% – 0.07%
N VERTEX	0.64% + 0.04% – 0.05%

Table 5.6, Table 5.7, and Table 5.8 show the variation in gap fractions for the 1800 GeV central jet sample and the 630 GeV forward and central jet samples, respectively. They all show similar results with a stable gap fraction with variations in data cuts.

Unfortunately, cutting out events that have more than one vertex has a side effect other than eliminating residual multiple interactions. The vertex finding algorithm was tuned to find the primary vertex, not to find always the correct number of vertices. So cutting on events with one vertex also cuts out real events with only one interaction that have been mis-reconstructed as having two (or more) vertices. There is an over-efficiency in finding the vertex with the vertex-finding algorithm, or a vertex

Table 5.6 Fitted gap fractions for the far gap region for 1800 central jets, varying the data cuts applied to the sample. The fraction is stable.

DATA CUT	1800 CENT JET FITTED GAP FRACTION
STANDARD	0.23% + 0.08% - 0.05%
ALL 'GOOD' JETS	0.24% + 0.06% - 0.06%
NO 'GOOD' JETS CUT	0.22% + 0.11% - 0.11%
E_T HIGH	0.22% + 0.04% - 0.04%
E_T LOW	0.25% + 0.06% - 0.05%
LUM 1	0.19% + 0.06% - 0.06%
LUM 2	0.24% + 0.08% - 0.08%
N VERTEX	0.21% + 0.06% - 0.05%

Table 5.7 Fitted gap fractions for the far gap region for 630 forward jets, varying the data cuts applied to the sample. The fraction is stable.

DATA CUT	630 FWD JET FITTED GAP FRACTION
STANDARD	1.22% + 0.10% - 0.09%
ALL 'GOOD' JETS	1.22% + 0.11% - 0.09%
NO 'GOOD' JETS CUT	1.22% + 0.09% - 0.09%
E_T HIGH	1.21% + 0.09% - 0.09%
E_T LOW	1.14% + 0.11% - 0.10%
LUM 1	1.17% + 0.16% - 0.13%
LUM 2	1.24% + 0.13% - 0.09%
N VERTEX	1.11% + 0.15% - 0.08%

Table 5.8 Fitted gap fractions for the far gap region for 630 central jets, varying the data cuts applied to the sample. The fraction is stable.

DATA CUT	630 CENT JET FITTED GAP FRACTION
STANDARD	0.94% + 0.07% - 0.05%
ALL 'GOOD' JETS	0.90% + 0.10% - 0.07%
NO 'GOOD' JETS CUT	0.93% + 0.08% - 0.07%
E_T HIGH	0.92% + 0.09% - 0.06%
E_T LOW	0.95% + 0.08% - 0.08%
LUM 1	0.94% + 0.09% - 0.08%
LUM 2	0.96% + 0.11% - 0.10%
N VERTEX	0.90% + 0.06% - 0.05%

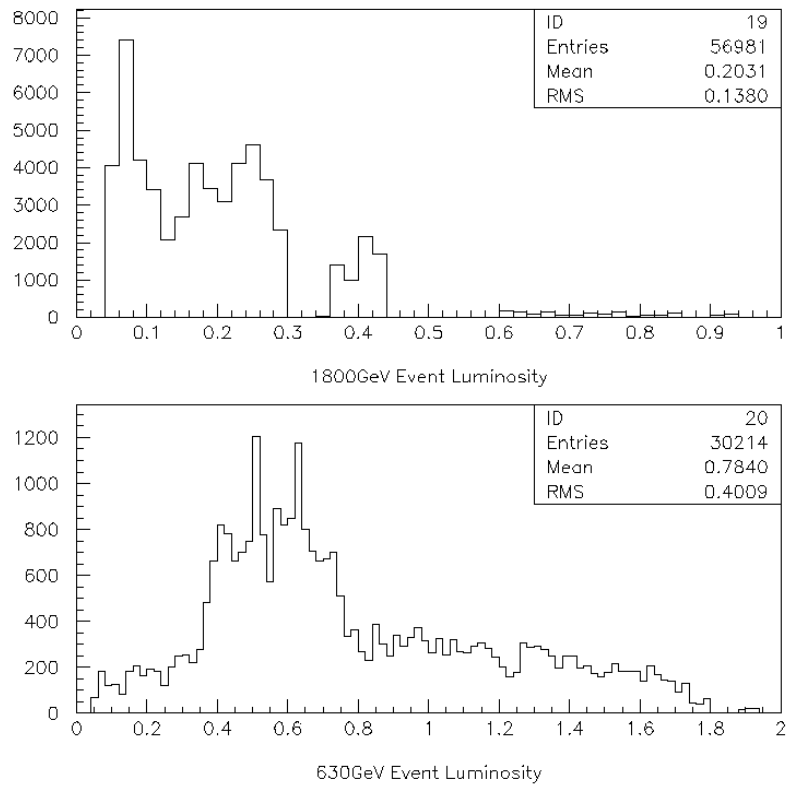


Figure 5.5 Luminosity distributions for 1800 and 630 GeV.

faking rate. The gap fraction is the number of non-diffractive events over the total number of events, so if events with a rapidity gap had the same average over-efficiency as all events, it would not effect the fraction. But events with a rapidity gap tend to be quieter and cleaner events, making it easier most of the time to identify correctly only one vertex compared to non-diffractive events. The true gap fraction, including this vertex effect is:

$$\text{Gapfraction} = \frac{\text{Gapevents}/\epsilon_G}{\text{Totalevents}/\epsilon_T}. \quad (5.1)$$

We use the 630 GeV central jet sample to look closer at the vertex cuts. We plot the total number of events with only one vertex divided by the total number of events with one or more vertices versus luminosity in Figure 5.6. At “zero” luminosity, all events should have only one vertex, so the y-intercept should equal one. That it doesn’t go through one is a measure of the vertex finding over-efficiency. From the plot for the 630 GeV central jet data sample the y-intercept, or ϵ_T is 0.920 ± 0.002 . Similarly, we can compare the number of gap events with one vertex to the number of gap events with one or more vertices, and find $\epsilon_G = 0.953 \pm 0.004$. The corrected 630 GeV central jet gap fraction is $0.91\% + 0.07\% - 0.05\%$.

In the 1800 GeV sample we did not need to make the $N_{vertex} = 1$ cut to eliminate residual multiple interactions (because of the low luminosity), but we applied it to be consistent with the 630 GeV sample. Since this entire sample is at very low luminosity, the correction is just the number events with only one vertex divided by the number with one or more vertices. This correction at 1800 GeV is 0.908 ± 0.001 . The fraction of gap events with one vertex is 0.972 ± 0.003 making the measured forward gap fraction $0.64\% \pm 0.05\%$. Table 5.9 shows the vertex efficiency for all of the samples and the total correction required.

We’ve also looked at several other possible sources of error, including residual noise and variations in background fit. Using the noise smearing found for the far gap, we can unsmear the data easily and re-fit (see Figure 3.9). Figure 5.7 shows the multiplicities without noise for the far gap. The gap fractions found are $0.68 + 0.05\% - 0.04$ for 1800 GeV forward jets, $0.24 \pm 0.05 \pm 0.05\%$ for 1800 GeV central jets, $1.25 \pm 0.07 \pm 0.06\%$ for 630 GeV forward jets and $0.93 \pm 0.06\%$ for 630 GeV central jets. These are all in agreement with the fitted gap fraction. We also varied the four parameter background fit ($a + bx + cy + dxy$) to a six parameter background fit to allow for more flexibility ($a + bx + cy + dxy + ex^2 + fy^2$). The gap fractions found with the six parameter fit with the same fit ranges are $0.69 \pm 0.05\%$ for 1800 GeV forward jets, $0.23 + 0.07\% - 0.06\%$ for 1800 GeV central jets, $1.23 + 0.09 - 0.08\%$ for 630 GeV forward jets and $0.95 + 0.09 - 0.06\%$ for 630 GeV central jets. Again, these are all in good agreement with the fitted four-parameter gap fraction.

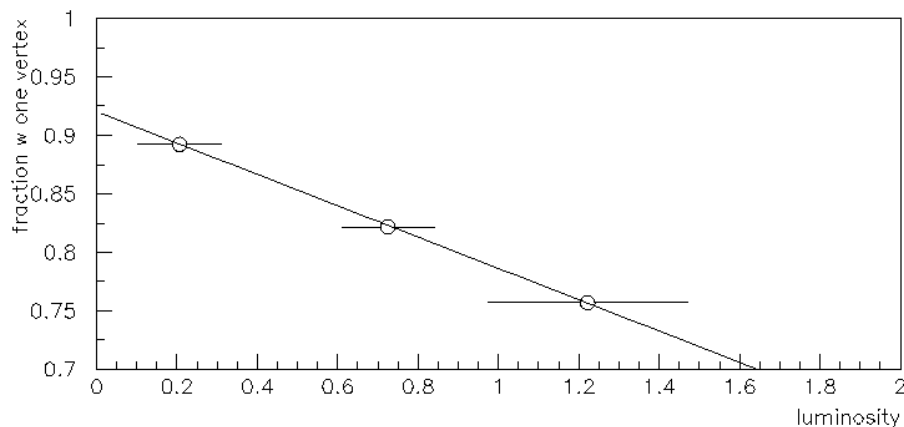


Figure 5.6 The fraction of events with one vertex versus luminosity in 630 GeV forward jets.

Table 5.9 The efficiency of the vertex algorithm to find one vertex in a single interaction event for all events and for gap events.

EVENT SAMPLE	ϵ_T	ϵ_G
1800 FWD JETS	0.908 ± 0.001	0.972 ± 0.003
1800 CEN JETS	0.846 ± 0.003	0.971 ± 0.008
630 FWD JETS	0.945 ± 0.004	0.935 ± 0.004
630 CEN JETS	0.920 ± 0.002	0.953 ± 0.003

The gap fraction also should not be dependent on the particular choice of calorimeter threshold. To study any dependence, we choose two other sets of thresholds to re-measure the gap fraction, called THRESH1 and THRESH2. In THRESH1, the electromagnetic calorimeter threshold is 200 MeV, the forward hadronic is 600 MeV, and the last layer of the forward hadronic is 70 MeV. For THRESH2, the electromagnetic calorimeter threshold is 300 MeV, the forward hadronic is 700 MeV, and the last layer of the forward hadronic calorimeter is 100 MeV. Figure 5.8 shows how the average calorimeter multiplicity decreases for the 1800 GeV forward jets in each of the samples. If we use the same fit range as for the standard threshold fit, the χ^2 per degree of freedom can move away from where it is stable—the fit range is too large. Table 5.10 shows the fitted gap fraction for the new thresholds where the χ^2 per degree of freedom is stable. Table 5.11 shows the same fitted gap fractions for 630 GeV forward and central jets. The fraction is stable and is not dependent on choice of threshold.

The last cross-check is to compare how the measured gap fraction changes from the two-dimensional

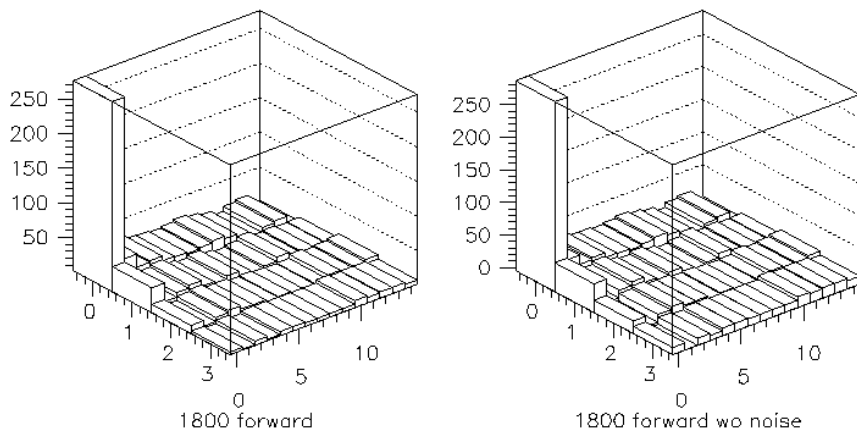


Figure 5.7 The far gap multiplicity distributions for 1800 GeV forward jets with and without noise. The $0 - 0$ multiplicity bin is slightly higher without noise, but the signal extracted from the fit is consistent.

Table 5.10 The fitted gap fractions for 1800 forward and central jets with different minimum thresholds for finding the calorimeter multiplicity.

DATA CUT	1800 FWD FITTED GAP FRACTION	1800 CENT FITTED GAP FRACTION
STANDARD	$0.69\% + 0.05\% - 0.05\%$	$0.23\% + 0.08\% - 0.05\%$
THRESH1	$0.73\% + 0.04\% - 0.06\%$	$0.25\% + 0.07\% - 0.06\%$
THRESH2	$0.65\% + 0.05\% - 0.05\%$	$0.27\% + 0.07\% - 0.05\%$

fit from the one-dimensional fits. We fit the one-dimensional n_{CAL} multiplicity to several functional forms, including a leading edge negative binomial (which in general fits multiplicity distributions very well) and a simple line. The signal changes on some samples quite dramatically between these two functional forms where a large systematic error needs to be added to the measurement. In addition, there is also an error attributed to when the fit starts and stops along the leading edge; there is an ambiguity in where the signal starts and where the background stops in the lower multiplicity bins. The two-dimensional fit solves these problems because there is more information available. Figure 5.9 shows the range of “good” fits to the far gap N_{CAL} distribution using the negative binomial fitted to the non-diffractive distribution as well as a line. Integrating over the first six bins, the negative binomial extracts 484 events as diffractive for a gap fraction of 1.04% and the line counts only 312 events for a gap fraction of 0.67%. The fitted line contains approximately the same number of signal events as the two-dimensional multiplicity distribution. In the one-dimensional method we integrate

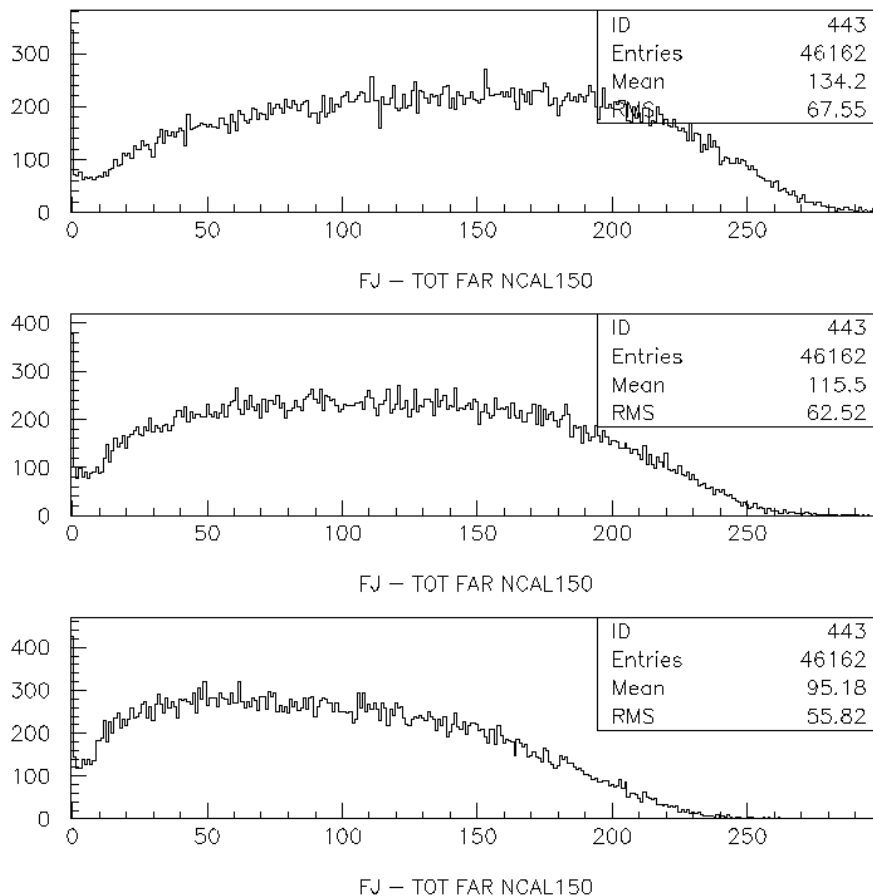


Figure 5.8 As the calorimeter threshold increases, the distributions shifts to lower multiplicity.

over the first 6 bins of N_{CAL} . Some of the “signal” events in the one-dimensional multiplicity are not considered “signal” in the two-dimensional multiplicity distribution because the number L0 detector hits is too high. The gap fractions measured between the two-dimensional method and the one-dimensional method are consistent with the line at low multiplicity, and the two-dimensional method is lower than the average of the two types of fits.

After examining various sources of error and performing cross-checks on the gap fraction, the only extra correction and source of systematic error is the vertex correction. The final measured gap fractions are shown in Table 5.12.

We can then look at ratios of these number. In the 630/1800 ratios, much of the gap efficiency dependence cancels, so it becomes more model independent. Table 5.13 shows the ratios in the data.

Table 5.11 The fitted gap fractions for 630 forward and central jets with different minimum thresholds for finding the calorimeter multiplicity.

DATA CUT	630 FWD FITTED GAP FRACTION	630 CENT FITTED GAP FRACTION
STANDARD	$1.22\% + 0.10\% - 0.09\%$	$0.94\% + 0.07\% - 0.05\%$
THRESH1	$1.26\% + 0.16\% - 0.10\%$	$0.95\% + 0.16\% - 0.09\%$
THRESH2	$1.25\% + 0.10\% - 0.10\%$	$0.92\% + 0.10\% - 0.05\%$

Table 5.12 The measured far gap fractions after the vertex correction.

DATA SAMPLE	MEASURED GAP FRACTION
1800 FORWARD JET	$0.64\% + 0.05\% - 0.05\%$
1800 CENTRAL JET	$0.20\% + 0.08\% - 0.05\%$
630 FORWARD JET	$1.23\% + 0.10\% - 0.09\%$
630 CENTRAL JET	$0.91\% + 0.07\% - 0.05\%$

Table 5.13 The measured ratios of the far gap fractions.

DATA SAMPLE	MEASURED RATIO
630/1800 FWD JET	$1.9 + 0.2 - 0.2$
630/1800 CEN JET	$4.6 + 1.2 - 1.8$
1800 FWD/CEN JET	$3.2 + 0.8 - 0.5$
630 FWD/CEN JET	$1.4 + 0.1 - 0.1$

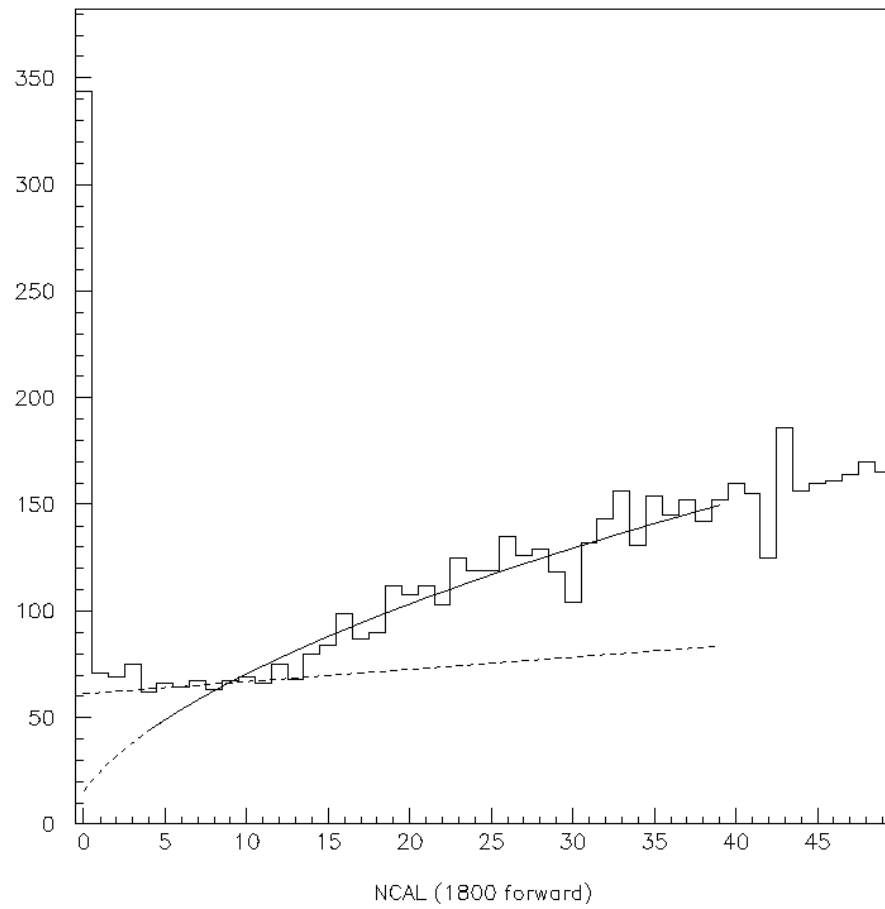


Figure 5.9 Fits to N_{CAL} using a negative binomial and a line.

ξ distribution

Now that we have measured the gap fractions at 1800 and 630 GeV for forward and central jets, we can confront the pomeron ξ that we are probing in each sample. (ξ is the fraction of the proton momentum carried by the pomeron.) We examine only the $(0, 0)$ bin in the multiplicity distribution to have a minimum of non-diffractive background. The purity of the $(0, 0)$ bin is $93.2\% \pm 0.4\%$, $84.2\% \pm 1.0\%$, $89.8\% \pm 0.4\%$, and $86.2\% \pm 0.2\%$ for 1800 forward jets, 1800 central jets, 630 forward jets, and 630 central jets, respectively. In each far-gap multiplicity distribution measured, we have only a couple hundred events with a rapidity gap. However, there is another trigger available that selects single diffractive events to provide a large sample to study. The single veto trigger (SV) requires no hits in either the north or south L0 counters as well as 2 15 GeV jets, the same jet requirements as the inclusive trigger. With this trigger we can examine forward jets, central jets, as well as inclusive jets for those events with a far rapidity gap (no hits in L0 or calorimeter).

Figure 5.10 shows the ξ distribution measured with the SV trigger for 1800 GeV forward and central jets. The mean ξ with the SV trigger is consistent with the mean ξ measured with each sample independently. As expected, the pomeron ξ for the central jets are higher than the pomeron ξ for the forward jets. The jets are boosted if the pomeron carries less momentum. Figure 5.11 shows the same ξ distributions for 630 GeV. Also, as expected, the ξ at 630 GeV is higher than the ξ at 1800 GeV. To get the same jet E_T as the 1800 sample, the 630 sample needs a larger momentum pomeron. The range of the ξ distribution, especially at 630 GeV is unexpected, though. Typically pomeron exchange is expected to be dominant for $\xi < 0.1$.

The same figures also show the ξ distribution for the inclusive jet η and the ξ probed in the entire sample. The ξ distribution extends to surprisingly high ξ . The highest ξ comes from the jets that are backscattered and are closest to the rapidity gap. There is also a small tail (not shown) that extends to very high ξ . This is from the non-diffractive contamination.

Event characteristics

We can also look at some of the other event characteristics of the data besides the ξ distribution. Figure 5.12 compares at 1800 GeV the number of jets, the jet width, the $\Delta\phi$ between jets and the jet E_T distribution for gap events and inclusive dijet events with no η restriction on the jets. Figure 5.13 shows a similar comparison at 630 GeV. In each case the gap distribution (dashed) is normalized to the inclusive dijet distribution. At both center-of-mass energies, the gap events have fewer jets than

the inclusive distribution. They are thinner and more back-to-back. This implies that the gap events are quieter overall with less radiation. The diffractive dijet E_T distributions also match the inclusive dijet E_T distribution, even at large E_T . If we compare to an inclusive dijet distribution (not shown) where the underlying event is subtracted from only the inclusive distribution, it also shows similar characteristics.

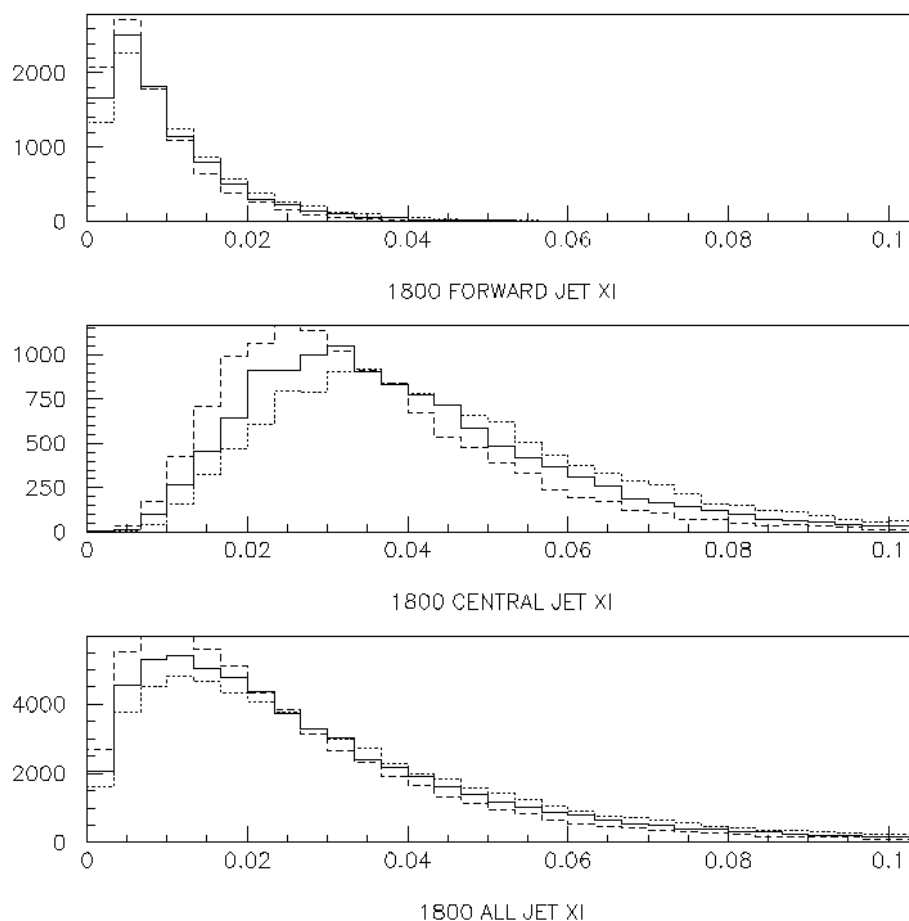


Figure 5.10 The 1800 GeV ξ distributions for forward, central and all jets. The factor of 2.2 is included to account for only using the EM.

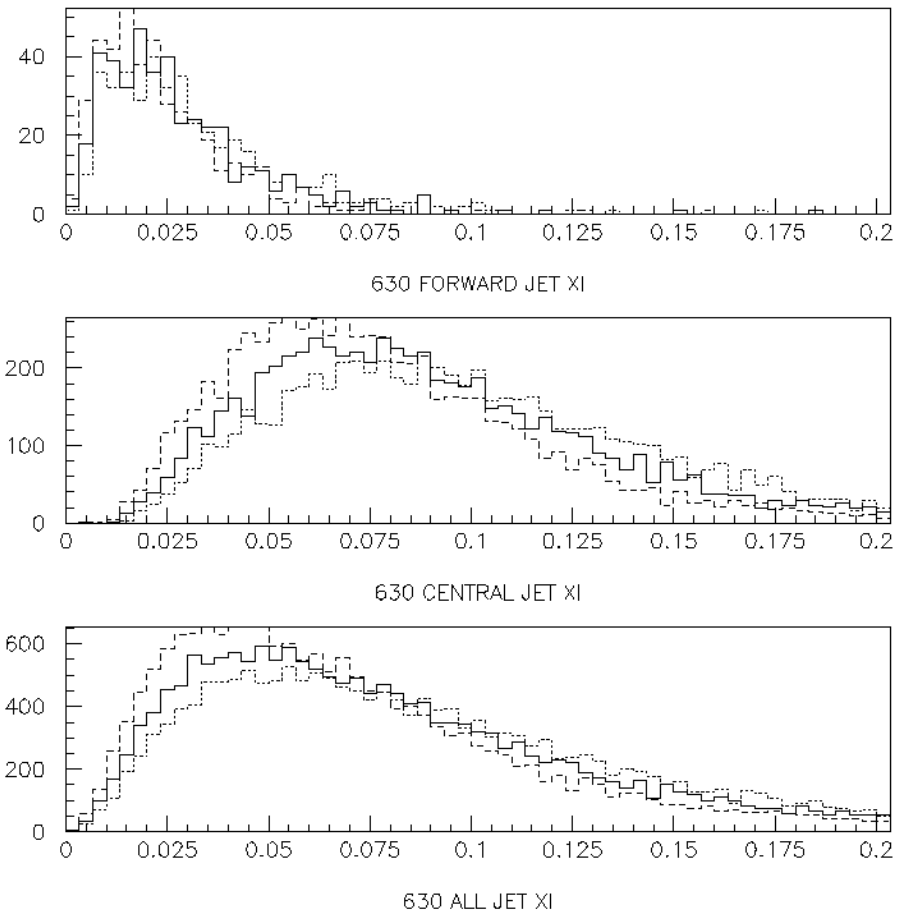


Figure 5.11 The 630 GeV ξ distributions for forward, central, and all jets.

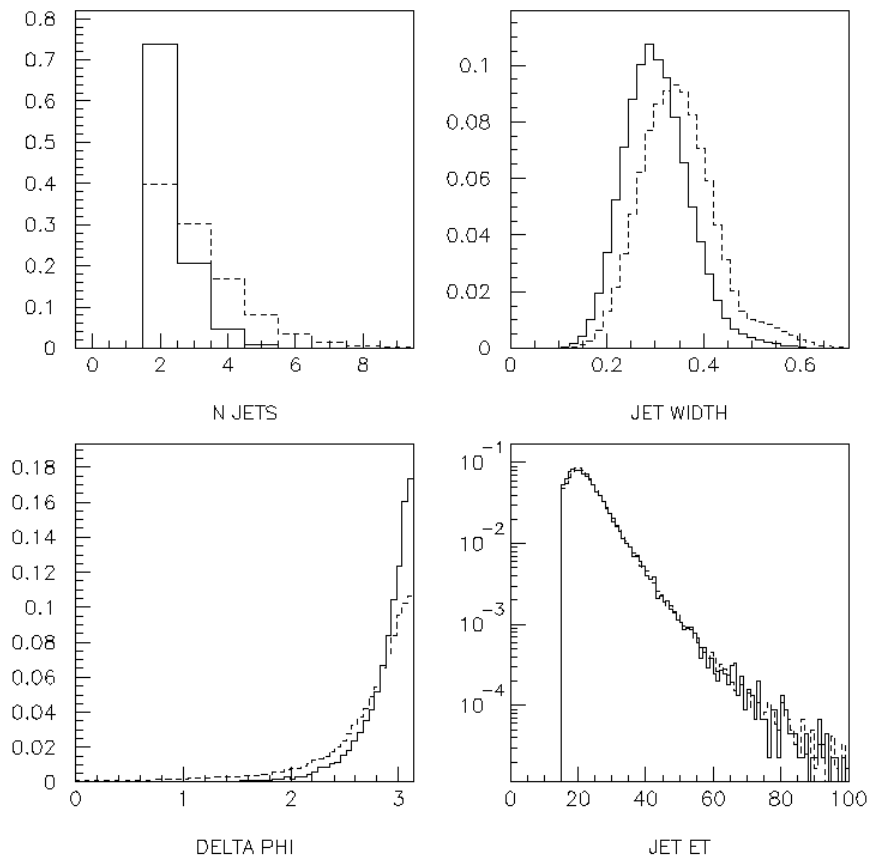


Figure 5.12 Comparing gap events (solid) to non-diffractive events (dashed) at 1800.

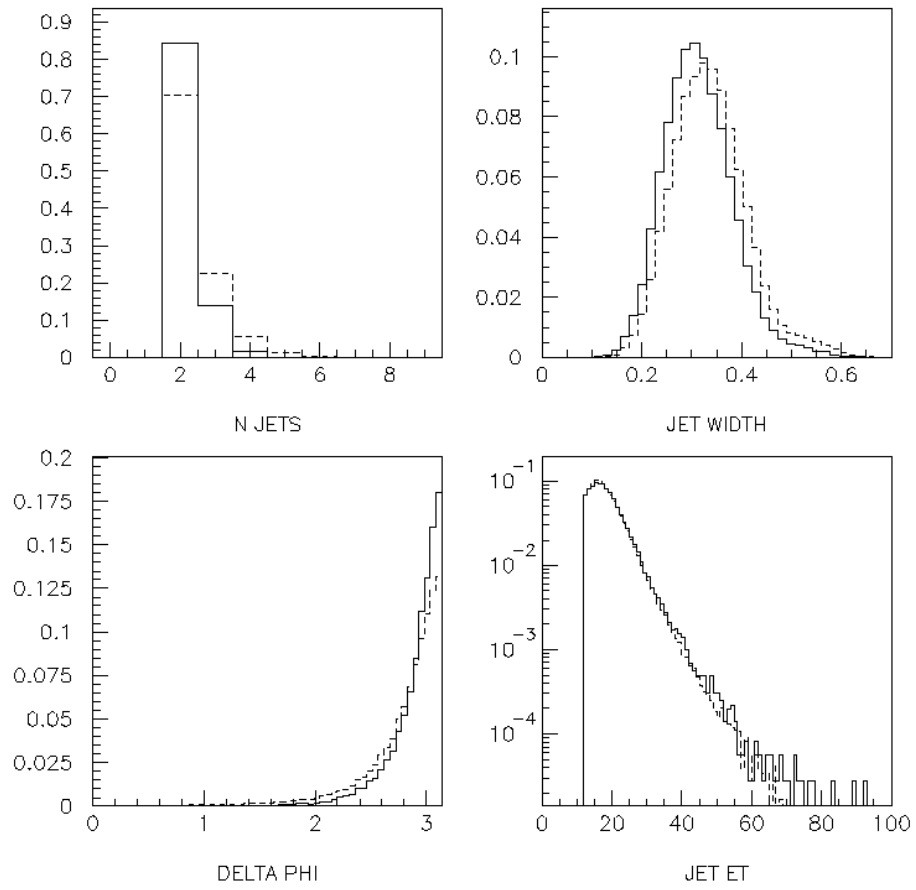


Figure 5.13 Comparing gap events (solid) to non-diffractive events (dashed) at 630.

6 INTERPRETATION

With the Monte Carlo predictions and the data measurements, we can compare how the Ingelman-Schlein model fits the data. First we look at the rates folding in the gap efficiency to the Monte Carlo predictions. Then we examine the ξ distributions and other characteristics.

Rate comparison

Multiplying the gap efficiency for the hard gluon by the rate expected gives the Monte Carlo predictions in Table 6.1. Although the hard gluon and flat gluon event characteristics with a large ξ follow the data, the overall rates predicted by the hard and flat gluon structures are high, even after being multiplied by the gap efficiency. If the pomeron is only a hard or flat gluon, this might be attributable to a normalization difference in the pomeron flux or a measure of the break-down of factorization. However, the problem is not just a normalization difference. The forward to central jet ratios are in the inverse direction from observed in the data. Table 6.2 has the ratios of the gap fractions for comparison to data. This means that just hard or flat gluons cannot be the structure of the pomeron.

Unlike the hard gluon and flat gluon, the quark and soft gluon pomeron structures predict a higher forward jet gap fraction than a central gap fraction. The quark structure is also consistent with the data ratios and approximate rates, although there is a large error. The event characteristics for the quark structure function are similar to data, although the jet E_T distribution begins to fall below PYTHIA at 630 GeV and larger E_T . In contrast, the event characteristics of the soft gluon alone differ greatly from the data. The soft gluon jet E_T falls below PYTHIA at both center-of-mass energies, and the soft gluon gap efficiency for the central region at both 1800 and 630 GeV is consistent with zero. This results in a predicted rate for the soft gluon central jets zero as well.

Overall for the Ingelman-Schlein model to hold would imply one of two possibilities: that the pomeron has either a large quark component or a combination of soft gluon and something harder to be consistent with the data. If the pomeron is predominately quarks, that would mean that factorization is a good approximation in $p\bar{p}$ collisions because the rates are similar when compared to data. If the pomeron is

a mixture of say hard (or flat) gluons and soft gluons, the ratios could come out correctly depending on the mixture amount. Since soft gluons essentially produces no rapidity gaps with central jets, this would, when added to the hard (or flat) gluons make the forward/central jet ratio greater than one. The diffractive rates would still be too high, implying (if this model is correct) either a break-down in factorization or flux renormalization.

Table 6.1 The rate predictions for Monte Carlo after folding in the gap efficiency.

MC EVT SAMPLE	HARD GLUON	FLAT GLUON	QUARK	SOFT GLUON
1800 FWD JET	$2.1\% \pm 0.3\%$	$2.4\% \pm 0.3\%$	$0.9\% \pm 0.1\%$	$1.6\% \pm 0.3\%$
1800 CEN JET	$2.8\% \pm 0.5\%$	$3.5\% \pm 0.6\%$	$0.5\% \pm 0.2\%$	$0.1\% \pm 0.1\%$
630 FWD JET	$4.6\% \pm 0.8\%$	$3.0\% \pm 0.7\%$	$2.2\% \pm 0.5\%$	$0.9\% \pm 0.7\%$
630 CEN JET	$5.1\% \pm 0.7\%$	$6.1\% \pm 0.8\%$	$1.4\% \pm 0.7\%$	$0.1\% \pm 0.1\%$

Table 6.2 The measured ratios of the far gap fractions for POMPYT structure functions.

MC EVENT SAMPLE	HARD GLUON	FLAT GLUON	QUARK	SOFT GLUON
630/1800 FWD JET	2.2 ± 0.5	1.3 ± 0.3	2.4 ± 0.6	0.6 ± 0.5
630/1800 CEN JET	1.8 ± 0.4	1.7 ± 0.4	2.8 ± 1.4	1.0 ± 1.4
1800 FWD/CEN JET	0.8 ± 0.2	0.7 ± 0.2	1.8 ± 0.7	$16. \pm 16.$
630 FWD/CEN JET	0.9 ± 0.2	0.5 ± 0.1	1.6 ± 0.9	$9.0 \pm 11.$

ξ

The ξ distributions seen in data are substantially higher at 630 GeV than the $\xi < 0.05$ or $\xi < 0.10$ rule-of-thumb ordinarily associated with diffraction. $\xi > 0.01$ is the Reggeon dominated regime. Even so, the POMPYT Monte Carlo does allow for such large ξ , but what its meaning in Regge context is unclear.

In Figure 6.1 we compare the ξ distribution for nominal 1800 GeV data (solid line) and a POMPYT hard gluon structure (dotted line). They are similar in shape and width. The effect of the background in the data is to extend the tail of the ξ distribution. Figure 6.2 shows the POMPYT hard gluon 1800 GeV forward jets (with a far gap), the analogous ξ distribution for PYTHIA 1800 GeV forward jets (imposing a far gap), and combining them with the same purity as in the (0,0) data bin. The

background has little effect on the ξ distribution because the purity is so high, but it creates a small tail of events at high ξ .

We simulate a type of soft color interaction by looking at non-diffractive data and calculate ξ the same way as for the diffractive data, except counting only the towers with an $|\eta| < 3.0$ (supposing color cancellation took place to produce a far rapidity gap). In Figure 6.3 and Figure 6.4 we measure the ξ distribution at 1800 and 630 GeV for forward jets (opposite the imposed rapidity gap), central jets, and all jets (dashed line). The diffractive data ξ distribution (solid line) is smaller and quieter than the non-diffractive data ξ , even with an imposed rapidity gap.

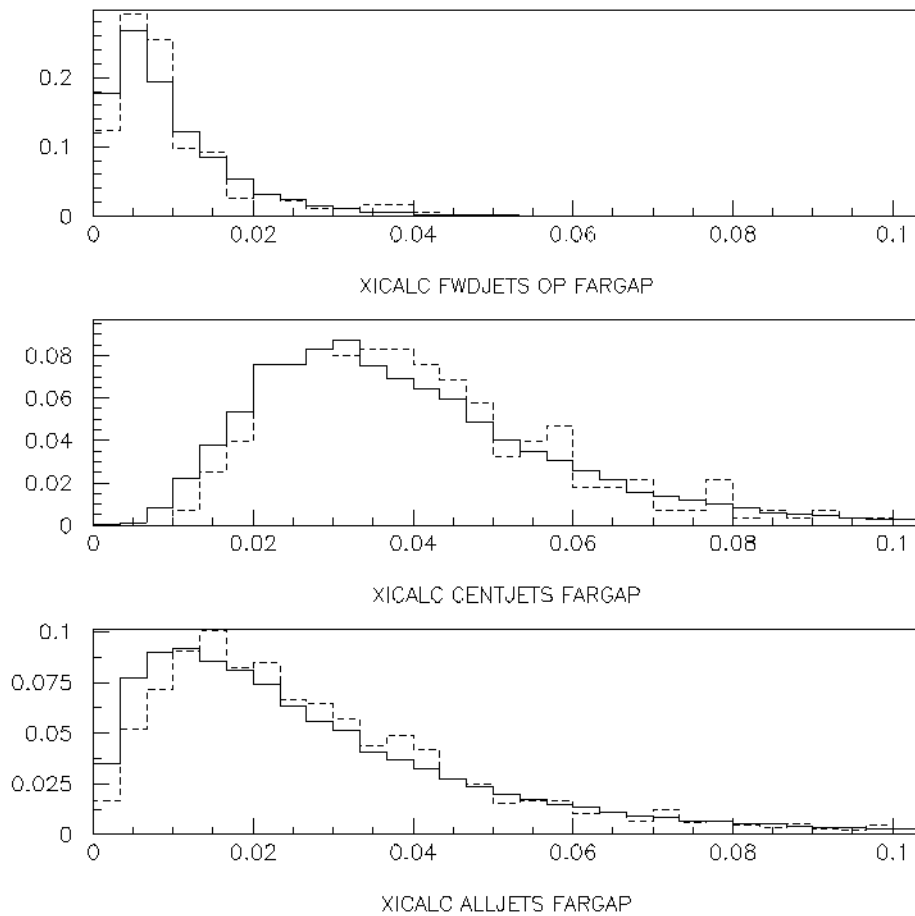


Figure 6.1 The ξ distribution for 1800 GeV data (solid) and for POMPYT hard gluons (dotted).

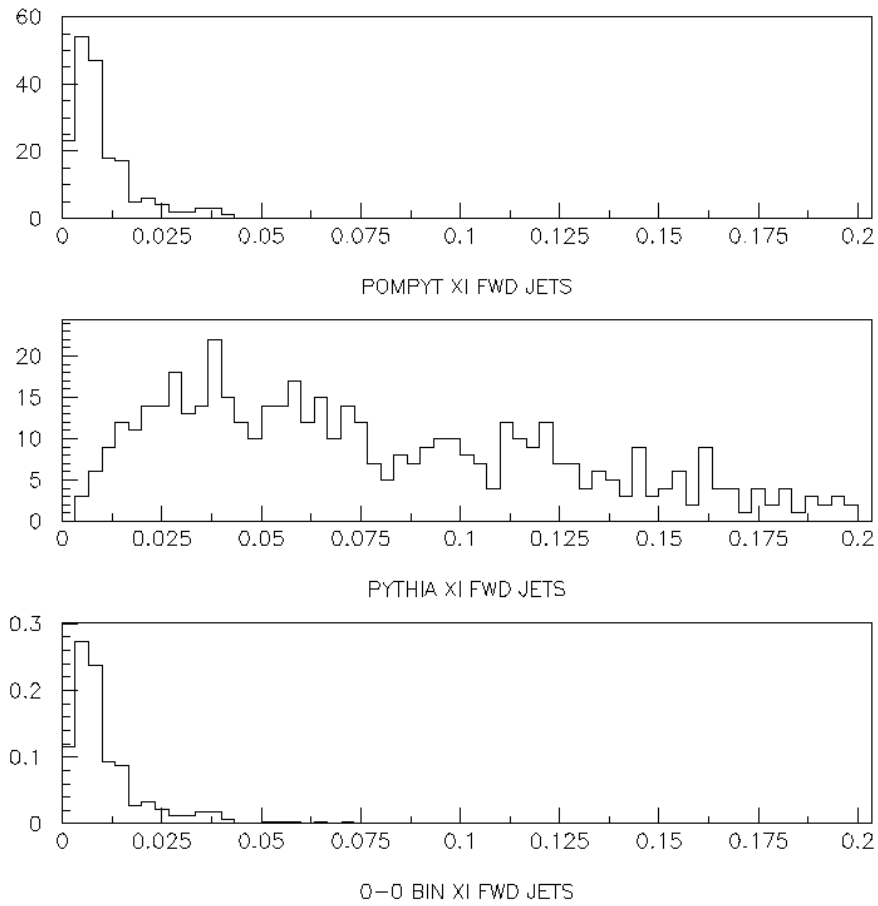


Figure 6.2 The ξ distribution for POMPYT hard gluon forward jets at 1800 with a far rapidity gap. Shown are also the analogous distribution for PYTHIA imposing a far gap, and the combined distribution with the same purity as in the $(0, 0)$ data.

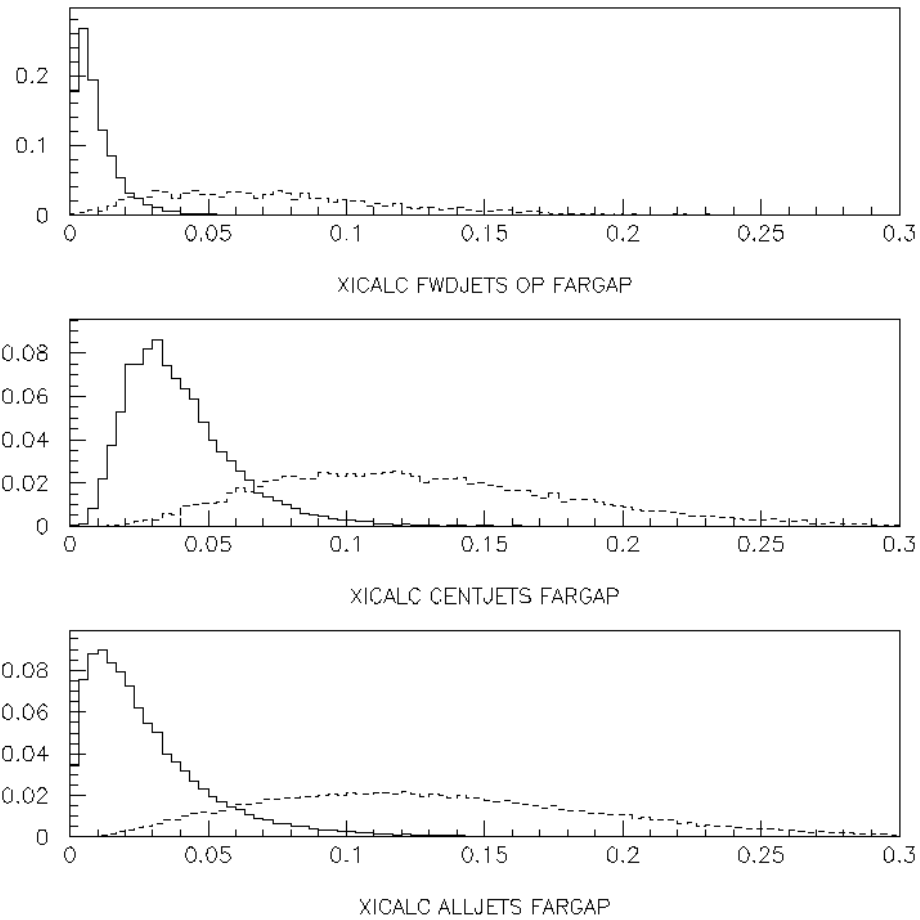


Figure 6.3 The diffractive ξ distribution (solid) for forward, central, and all jets at 1800 GeV. Also calculated is the unnormalized ξ distribution for non-diffractive data (dotted), assuming color cancellation to produce a far gap.

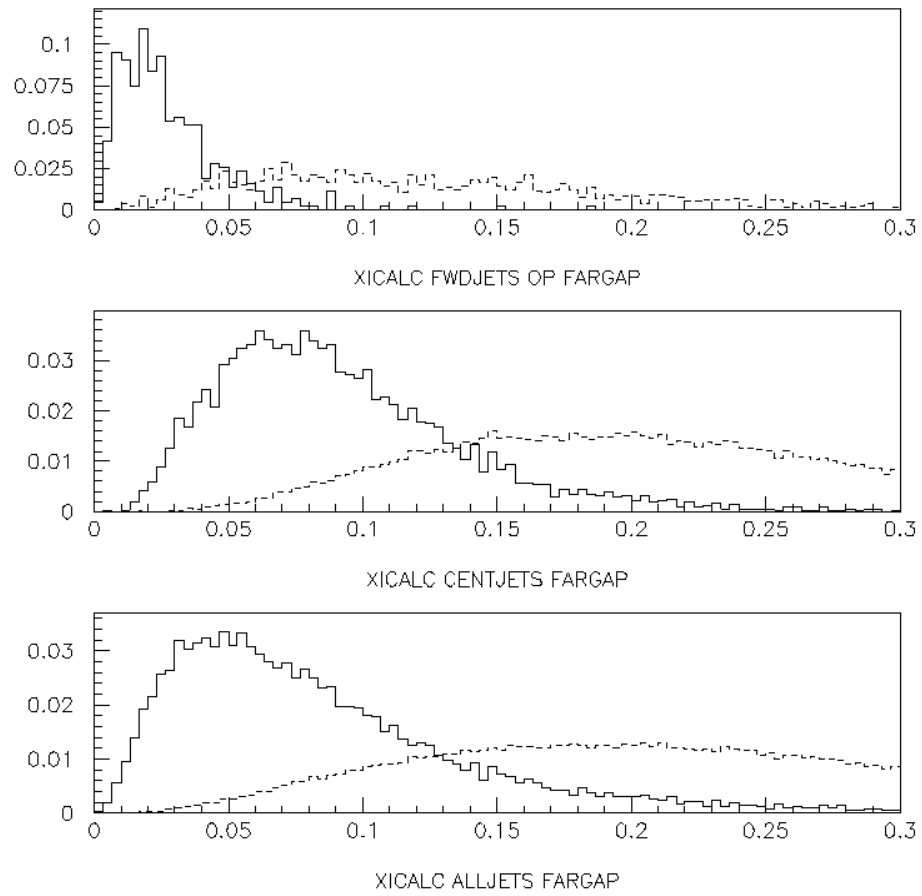


Figure 6.4 The diffractive ξ distribution (solid) for forward, central, and all jets at 630 GeV. Also calculated is the unnormalized ξ distribution for non-diffractive data (dotted), assuming color cancellation to produce a far gap.

7 CONCLUSION

We have shown a class of events from inclusive and forward gap triggers used throughout the last two running periods. A selection of events with two jets and one forward rapidity gap shows the expected characteristics of hard single diffraction. The large sample of single diffractive data allows us to study this phenomena as a function of jet rapidity, transverse energy, gap definition, pomeron momentum, and center of mass energy. In the Ingelman-Schlein model, these data can be explained with either a dominant quark component or a mixture of hard (or flat) and soft gluons components in the pomeron. Although the rates for a pomeron with a mixture of flat (or hard) and soft gluon content are too large, this may be due to the non-factorizable component (also called the survival probability). The observation of large ξ in the data, as well as large ξ required in the Monte Carlo to simulate the data, presents an inconsistency with the Ingelman-Schlein model. The pomeron structure and the Soft-Color Interaction model needs to be investigated more further.

BIBLIOGRAPHY

- [1] Collins, P.D.B. *An Introduction to Regge Theory and High-Energy Physics*, 1977, Cambridge University Press, Cambridge, Massachusetts.
- [2] Ingelman, G. & Schlein, P. *Phys. Lett.* **B152** (1985) 256.
- [3] Halzen, F. & Martin, A. *Quarks and Leptons: an Introductory Course in Modern Particle Physics*, 1984, Wiley, New York.
- [4] Gross, F. *Relativistic Quantum Mechanics and Field Theory*, 1993, John Wiley and Sons, New York, 171,581.
- [5] Erhan, S. & Schlein, P. "Evidence for ξ and t-dependent damping of the Pomeron flux in the proton," hep-ph/9804257, 1998.
- [6] Avila, C. "What is the value of σ_{tot} at the Tevatron?," *Presented at 4th Workshop on Small-x and Diffractive Physics, Fermilab, 1998*.
- [7] Bruni, P. & Ingelman, G. "Diffractive hard scattering at ep and $p\bar{p}$ colliders," *Presented at Europhysics Conference on High Energy Physics, Marseille, France, 22-28 Jul 1993*.
- [8] Donnachie A. & Landshoff, P.V. *Nucl. Phys.* **B303** (1988) 634.
- [9] A. Edin, G. Ingelman and J. Rathsman, "Unified description of rapidity gaps and energy flows in DIS final states," *Z. Phys.* **C75**, 57 (1996).
- [10] A. Edin, G. Ingelman and J. Rathsman, "Soft color interactions and the diffractive structure function," *J. Phys.* **G22**, 943 (1996).
- [11] A. Edin, G. Ingelman and J. Rathsman, "Soft color interactions as the origin of rapidity gaps in DIS," *Phys. Lett.* **B366**, 371 (1996).
- [12] A. Edin, G. Ingelman and J. Rathsman, "Rapidity gaps in DIS through soft color interactions," hep-ph/9508224.
- [13] Collins, J. "Proof of Factorization for Diffractive Hard Scattering," hep-ph/9709499, 1997.
- [14] Edin, A. "Soft Colour Interactions at the Tevatron", *Presented at 4th Workshop on Small-x and Diffractive Physics, Fermilab, 1998*.
- [15] Bjorken, J. Colloquium presented at Fermilab, March 3 1999.
- [16] Lippmaa, E. *et al.* [FELIX Collaboration], "FELIX: A Full acceptance detector at the LHC: Letter of intent," CERN-LHCC-97-45.
- [17] Sjostrand, T. Private Communication
- [18] Abachi, S. *et al.* 1993, *Nucl. Instr. and Methods*, **A338**, 185.
- [19] Bantly, J. *et al.* 1993, D0 NOTE 1996.

- [20] Nang, F & Partridge, R. 1990, D0 NOTE 998.
- [21] Baden, A.R. & Hadley, N.J. 1990, D0 NOTE 957.web page
http://www-d0.fnal.gov/hirosky/d0_private/sddp_updates/sddp_updates.html
- [22] deKerret, H. *et al.*, PhysLett. 68B 385 (1977).
- [23] Joyce, D. *et al.*, Phys. Rev. D 48 1943 (1993).
- [24] Abachi, S. *et al.*, D0 Collaboration, PRL 76 734 (1996).
- [25] Abachi, S. *et al.*, D0 Collaboration, PRL 72 2332 (1994).
- [26] Abbott, B. *et al.*, D0 Collaboration, Physics Letters B 440 189 (1998).
- [27] Collins & Berera, Private Communication
- [28] Drees, Private Communication
- [29] “Hard Single Diffractive Jet Production at DØ” Abachi, S. *et al.*, Contributed to 28th International Conference on High-energy Physics (ICHEP 96), Warsaw, Poland, 25-31 Jul 1996, FERMILAB-PUB-96-247-E.
- [30] P. Bruni, A. Edin, & G. Ingelman, “POMPYT version 26 –A Monte Carlo to Simulate Diffractive Hard Scattering Processes,” ISSN 0418-9833.
- [31] T. Sjostrand, Computer Physics Commun. **82** (1994) 74.
- [32] Collins, J. “Light-cone Variables, Rapidity and All That,” hep-ph/9705393, 1997.
- [33] Hirosky, B. http://www-d0.fnal.gov/hirosky/d0_private/sddp_updates/sddp_updates.html
- [34] Abe, F. *et al.*, CDF Collaboration, “Measurement of Diffractive Dijet Production at the Tevatron,” PRL 79 2636 (1997).
- [35] J. Montanha, private conversation and internal physics note